

Functional nanocomposites, block copolymers, and nanocrystals: From synthesis, self-assembly to application

By

Lei Zhao

A dissertation submitted to the graduate faculty
in partial fulfillment of the requirements for the degree of

DOCTOR OF PHILOSOPHY

Major: Materials Science and Engineering

Program of Study Committee:

Zhiqun Lin, Major Professor

Surya K. Mallapragada

Kaitlin Bratile

Ning Fang

Malika Jeffries-EL

Iowa State University

Ames, Iowa

2011

Copyright © Lei Zhao, 2011. All rights reserved.

Dedications

I would like to dedicate this work to my wife Ping Liu, and my parents.

Table of Contents

List of Figures	v
Abstract	xi
1. General Introduction	1
1.1 Organic-Inorganic Nanocomposites Used in Solar Cell.....	1
1.1.1 CP/NC Composites	3
1.1.2 CP-NP Nanocomposites	9
1.2 Self-Assembly of Non-Linear Polymers at the Air/Water Interface: Effect of Molecular Architecture.....	14
1.2.1 Polymer Brushes.....	18
1.2.2 Star-Like Polymers	20
1.2.3 Dendritic Polymers.....	21
1.2.4 Linear-Dendritic Polymers	22
2. Anisotropic Nanocomposites via Directly Coupling Conjugated Polymers with Quantum Rods	34
2.1 Introduction	34
2.2 Result and Discussion	35
2.3 Conclusion	49
2.4 Experimental Section	50
3. Anisotropic Organic-Inorganic Nanocomposites by Placing Conjugated Polymers in Intimate Contact with Quantum Rods	57
3.1 Introduction	57
3.2 Result and Discussion	59
3.3 Conclusion	71
3.4 Experimental Section	72
4. Self-Assembly of Ultrahigh Molecular Weight Comb Block Copolymer at the Air/Water Interface	80
4.1 Introduction	80
4.2 Experimental Section	81
4.3 Result and Discussion	83
4.4 Conclusion	96

5. Self-Assembly of Polystyrene-Polylactide Bottlebrush Block Copolymer at the Air/Water Interface	100
5.1 Introduction	100
5.2 Experimental Section	104
5.3 Result and Discussion	105
5.4 Conclusion	119
6. Patterning of Conjugated Polymer with Enhanced Photoluminescence via Self-Assembly at the Air/Water Interface	124
6.1 Introduction	124
6.2 Experimental Section	127
6.3 Result and Discussion	132
6.4 Conclusion	146
7. Patterning of Hydrophobic Conjugated Copolymer with Enhanced photoluminescence via Dewetting at the Air/Water Interface	154
7.1 Introduction	154
7.2 Experimental Section	155
7.3 Result and Discussion	159
7.4 Conclusion	170
8. Self-Assembly of P3HT-PDMAEMA Responsive Block Copolymer at Air/Water Interface	176
8.1 Introduction	176
8.2 Experimental Section	176
8.3 Result and Discussion	177
8.4 Conclusion	187
Acknowledgement	191
Publications	192

List of Figures

Figure 1-1. Synthetic pathway for the preparation of aniline tetramer/CdSe nanohybrids.	10
Figure 1-2. Synthetic pathway for the preparation of a family of carbodithioic acid functionalized regioregular oligo- and polythiophene.	11
Figure 1-3. Grafting vinyl-terminated P3HT onto [(4-bromophenyl)methyl] dioctylphosphine oxide-functionalized CdSe QDs.	13
Figure 1-4. Molecular structure of linear-dendritic polymer.	19
Scheme 2-1. Grafting P3HT onto bromobenzylphosphonic acid functionalized CdSe NRs by catalyst-free click reaction	36
Figure 2-1. TEM images of (a) BBPA-functionalized CdSe NRs, and (b) close-up of an individual NR	38
Figure 2-2. Dynamic light scattering (DLS) measurements on (a) BBPA functionalized CdSe NRs; and (b) P3HT-CdSe NR nanocomposites prepared by click reaction.	38
Figure 2-3. ^{31}P NMR spectra of (a) pure ODPA, (b) pure BBPA, and (c) CdSe-BBPA and CdSe-ODPA complex (see Supporting Information: BBPA ligand recovery for NMR analysis).	40
Figure 2-4. TEM images of CdSe NRs synthesized with (a) BBPA solely, (b) ODPA/BBPA mixture at 1:1 molar ratio, and (c) ODPA/BBPA mixture at 3:1 molar ratio.	40
Figure 2-5. TEM images of P3HT/CdSe NR composites prepared by (a) physically mixing ethynyl-terminated P3HT and azide-benzylphosphonic acid functionalized CdSe NRs, and (b) P3HT-CdSe NR nanocomposites synthesized by click reaction	42
Figure 2-6. Thermogravimetry analysis (TGA) of (a) BBPA functionalized CdSe NRs, (b) P3HT-CdSe NR nanocomposites prepared by click reaction.	43
Figure 2-7. (a) HRTEM image of P3HT-CdSe NR nanocomposites synthesized by click reaction, and (b) TEM image of nanocomposites in a P3HT homopolymer matrix. The P3HT matrix is clearly evident on the background of TEM images, appearing dark and/or grey.	44
Figure 2-8. (a) Absorption spectra of azide-benzylphosphonic acid functionalized CdSe NRs	

(black curve), ethynyl-terminated P3HT (blue curve), and P3HT-CdSe nanocomposites prepared by click reaction (red curve). (b) Emission spectra of ethynyl-terminated P3HT (blue curve) and nanocomposites (red curve) in dry state.

45

Figure 2-9. ^1H NMR spectra of P3HT in chloroform that was grafted on CdSe (black) and P3HT after detached from the CdSe surface (red) in the nanocomposites prepared by click reaction.

46

Figure 2-10. (a) ^1H NMR spectrum of ethynyl-terminated P3HT, and (b) ^1H NMR spectrum of P3HT detached from the CdSe NR surface in the nanocomposites prepared by click reaction.

46

Figure 2-11. Normalized time-resolved photoluminescence decays of P3HT, physical mixture of P3HT/BBPA-CdSe NR, P3HT-CdSe nanocomposites prepared by click coupling, respectively, monitored at $\lambda_{\text{exc}} = 407$ nm and $\lambda_{\text{em}} \geq 500$ nm. The curve fitting yielded the average lifetimes of 370 ps for P3HT, 320 ps for P3HT/CdSe NR composite, and 105 ps for P3HT-CdSe nanocomposites via click reaction, respectively.

48

Scheme 3-1. Direct grafting vinyl-terminated P3HT onto bromobenzylphosphonic acid-functionalized CdSe QRs (i.e., BBPA-CdSe QRs) by Heck coupling, yielding P3HT-CdSe QR nanocomposites.

59

Figure 3-1. TEM images of (a) BBPA-functionalized CdSe QRs (i.e., BBPA-CdSe QRs) prepared using the ODP:BBPA mixture at the 5:1 molar ratio, and (b) close-up of individual BBPA-CdSe QRs in which the crystalline lattice is clearly evident.

60

Figure 3-2. Dynamic light scattering (DLS) measurements on (a) BBPA-CdSe QRs, and (b) P3HT-CdSe QR nanocomposites prepared by Heck coupling.

62

Figure 3-3. TEM images of CdSe QRs synthesized with (a) BBPA solely, (b) TDPA:BBPA mixture at 3:1 molar ratio, (c) TDPA:BBPA mixture at 5:1 molar ratio, and (d) ODP:BBPA mixture at 3:1 molar ratio.

63

Figure 3-4. TEM images of (a) physical mixture of vinyl-terminated P3HT and BBPA-CdSe QRs, (b) P3HT-CdSe QR nanocomposites synthesized by Heck coupling, and (c) P3HT-CdSe QR nanocomposites in the P3HT homopolymer matrix.

65

Figure 3-5. Thermogravimetry analysis (TGA) of (a) vinyl-terminated P3HT, (b) P3HT-CdSe QR nanocomposites prepared by Heck coupling.

66

Figure 3-6. HRTEM image of P3HT-CdSe QR nanocomposites synthesized by Heck coupling.

Figure 3-7. (a) ¹HNMR traces of P3HT bonded on the CdSe surface (black curve) and in the free state (red curve) in the chloroform. The signal from d-chloroform at 7.26 ppm was shown as reference. (b) ¹HNMR traces of P3HT stripped from P3HT-CdSe nanocomposites. Insert shows the close-up from 5 ppm to 6 ppm.

Figure 3-8. (a) Absorption spectra of the P3HT-CdSe nanocomposites prepared by Heck coupling (red curve), BBPA-CdSe QRs (black curve), and vinyl-terminated P3HT (blue curve); (b) Emission spectra of vinyl-terminated P3HT (blue curve) and the P3HTCdSe nanocomposites (red curve) in dry state.

Table 4-1 Height and surface coverage of CBCP ribbons obtained from AFM images.

Figure 4-1. (a) Chemical structure and (b) schematic representation of the newly synthesized CBCP, which can be viewed as a triblock polymer. Each block is labeled as A (within a thick dotted circle), B (within a thin dotted circle), and C, respectively.

Figure 4-2. Isotherms of the Langmuir monolayer of CBCP obtained from the chloroform solution (black solid line) and the toluene solution (red dash line), respectively. A_b and A_p are the area of brush-like structures and the area of pancake-like structures, respectively.

Figure 4-3. AFM height images of the CBCP Langmuir monolayers obtained from the chloroform solution at various transfer pressure: (a) $\pi = 0$ mN/m, (b) $\pi = 10$ mN/m, (c) $\pi = 22$ mN/m, and (d) $\pi = 45$ mN/m. Scan size = $10\ \mu\text{m} \times 10\ \mu\text{m}$ and z scale = 30 nm for all images. Scan size = $3\ \mu\text{m} \times 3\ \mu\text{m}$ for the insert in (c).

Figure 4-4. AFM height images of the CBCP Langmuir monolayers obtained after solvent evaporation from chloroform solution for 30 min (a) and 2h (b). The surface coverage of a is 24% and b is 30%.

Figure 4-5. AFM height images of the CBCP Langmuir monolayers obtained after solvent evaporation for 2 h. (a) from chloroform solution, and (b) from toluene solution. The deposition pressure, $\pi = 0$ mN/m. Scan size = $10\ \mu\text{m} \times 10\ \mu\text{m}$ and z scale = 30 nm for both images.

Figure 4-6. Schematic illustration of the packing of microstructures at different surface pressures. B block in red = hydrophilic block, and C block in blue= PS block (i.e., arms).

Figure 4-7. Representative compression-expansion cycles of the CBCP ended in the different regions: (a) extended liquid state region, (b) plateau region, and (c) condensed state region.

Figure 4-8. AFM height images of the CBCP film originally deposited from the chloroform solution at $\pi = 20$ mN/m (a) before, and (b) after CS₂ vapor annealing for 7 h; after methanol vapor annealing for (c) 2 h, and (d) 7 h. Scan size = $10\ \mu\text{m} \times 10\ \mu\text{m}$ and z scale = 30 nm

96

Figure 5-1. Chemical structures of (a) bottlebrush copolymer (BBCP), and (b) PS-b-PLA linear block copolymer (LBCP). (c) Molecular morphology of BBCP

103

Figure 5-2. Schematic representations of (a) bottlebrush copolymer with PLA (yellow) and PS (blue), and (b) a linear block copolymer of PS-b-PLA, in which PLA and PS blocks are in yellow and blue, respectively.

104

Table 5-1 Height and surface coverage of BBCP domains obtained from AFM images.

106

Figure 5-3. Pressure ~ area isotherms of the Langmuir monolayer of (a) BBCP and (b) LBCP. Three regions are labelled as (i) gas state, (ii) liquid state, and (iii) condensed state.

106

Figure 5-4. AFM height images of the BBCP Langmuir monolayers obtained from the chloroform solution at various transfer pressures: (a) $\pi = 1$ mN/m, (b) $\pi = 5$ mN/m, (c) $\pi = 13$ mN/m, and (d) $\pi = 30$ mN/m. Scan size = $3\ \mu\text{m} \times 3\ \mu\text{m}$ and scan size = $0.5\ \mu\text{m} \times 0.5\ \mu\text{m}$ for the insert in (d). The Height of the domain is shown in the up-right corner, and the its surface coverage is shown in the low-right corner

107

Figure 5-5. (a) AFM height image of the BBCP Langmuir monolayer obtained after scratching off the top portion of monolayer. Scan size = $1\ \mu\text{m} \times 1\ \mu\text{m}$. (b) The corresponding phase image of (a). (c) Close-up of the phase image in (b); the domain is enclosed with red dash line, and arms with white. Scan size = $0.3\ \mu\text{m} \times 0.3\ \mu\text{m}$

108

Figure 5-6. AFM height image (top) and phase image (low) of (a) original Langmuir monolayer, (b) monolayer annealed at 95°C for 12h, (c) monolayer annealed at 170°C for 5h. Scan size = $1\ \mu\text{m} \times 1\ \mu\text{m}$, z scale = 50 nm, and phase scale = 50°. The bearing height of domains are labeled on each height images.

110

Figure 5-7. Schematic illustration of two models PS-b-PLA block copolymer at the air/water interface.

112

Figure 5-8. (a) AFM height image of Langmuir monolayer after immersion in the buffer solution without the addition of enzyme for 1h. (b) AFM height image of Langmuir monolayer undergoing enzymatic degradation for 1h. (c) Corresponding phase image of (b).

112

Figure 5-9. Schematic stepwise representation of the packing of microstructures of BBCP. (a) at the low pressure (i.e., between regions i and ii, where PLA arms (yellow) highly spread over the water surface, and PS (blue) form domains on the top of PLA; (b) at the intermediate

pressure (i.e., region ii), where the rearrangement of PLA arms occur; and (c) at the high pressure (i.e., region iii), where the PLA arms are highly compressed, and PS domains become connected.

115

Figure 5-10. AFM height images (a, c, e and g) and corresponding phase images (b, d, f and h) of Langmuir monolayers of PS-b-PLA LBCP obtained from the chloroform solution at various surface pressures: (a) and (b) $\pi = 1$ mN/m, (c) and (d) $\pi = 5$ mN/m, (e) and (f) $\pi = 13$ mN/m, and (g) and (h) $\pi = 30$ mN/m. Scan size = $1 \mu\text{m} \times 1 \mu\text{m}$

117

Figure 5-11. Schematic illustration of the packing of microstructures of PS-b-PLA LBCP at different surface pressures. (a) at the low pressure, where PLA arms (yellow) highly spread over the water surface, and PS (blue) form domains on the top of PLA). (b) at the intermediate pressure (i.e., region ii), where the folding of PLA chains lead more PLA to occupy the space between PS domains; and (c) at the high pressure (i.e., region iii), where the folding of PLA chains is complete, thereby leading to the formation of a topologically continuous film

118

Figure 6-1. (a) Chemical structure and (b) schematic representation of multi-arm PtBA-P3HT block copolymer.

133

Figure 6-2. Pressure -area isotherms of multi-arm PtBA-P3HT block copolymer: (I) liquid region, (II) plateau region, (III) sub-condensed region, (IV) condensed region, (V) post condensed region. Insertion shows the illustration of molecular architecture at gas state (right) and condensed state (left).

134

Figure 6-3. AFM height images of the MSBC Langmuir monolayers obtained from the chloroform solution at various transfer pressure: (a) gas region; (b) liquid region; (c) plateau region; (d) sub-condensed region; (e) condensed region; (f) post condensed region. Scan size = $5 \mu\text{m} \times 5 \mu\text{m}$ and z scale = 100 nm for all images

135

Figure 6-4. Schematic illustration of the packing of microstructures at different surface pressures. (a) gas region where multi-arm molecules are fully spread; (b) liquid and plateau region, (c) condensed state region, as well as possible P3HT packing (d) in this region. Red dot line represents the axis of nano-fiber.

136

Figure 6-5. TEM images of LB monolayer deposited from (a),(b) liquid region; (c),(d) plateau region; (e),(f) condensed region.

137

Figure 6-6. (a) AFM height image, (b) TEM image, and (c) fluorescent image of MSBC pattern deposited at condensed region. Scan size = $20 \mu\text{m} \times 20 \mu\text{m}$ and z scale = 100 nm for AFM images.

138

Figure 6-7. (a) Close up TEM image of MSBC network deposited at condensed region, as well as its AFM phase images at different magnification (b) size = $3\ \mu\text{m} \times 3\ \mu\text{m}$ and phase scale = 50° and (C) size = $3\ \mu\text{m} \times 3\ \mu\text{m}$ and phase scale = 30° .

139

Figure 6-8. Photoluminescence spectra of (a) MSBC patterns, P3HT homopolymer in solution and solid state; (b) MSBC monolayer at the liquid region and condensed region.

141

Table 7-1. Height, Diameter and surface coverage of PI-PS-P3HT circular domains obtained from AFM images

163

Scheme 7-1. Synthesis of polyisoprene-b-polystyrene-b-poly(3-hexylthiophene) by coupling of living polyisoprene-b-polystyryl lithium with allyl-terminated regioregular poly(3-hexylthiophene)

155

Figure 7-1. ^1H NMR spectrum of polyisoprene-b-polystyrene-b-poly(3-hexylthiophene) (PI-PS-P3HT)

157

Figure 7-2. Pressure -area isotherms PI-PS-P3HT triblock copolymer : (I) liquid region, (II) condensed region. Insertion shows the chemical structure of PI-PS-P3HT triblock copolymer

159

Figure 7-3. AFM height images of the PI-PS-P3HT triblock copolymer LB monolayers obtained from the chloroform solution at (a), (b) gas region; (c),(d) condensed region. Scan size is $20\ \mu\text{m} \times 20\ \mu\text{m}$ for (a) and (c), $5\ \mu\text{m} \times 5\ \mu\text{m}$ for (b) and (d), respectively. The z scale is 50 nm for all images.

160

Figure 7-4. TEM images of PI-PS-P3HT triblock copolymer monolayer deposited at gas region at (a) low and (b) high magnification.

162

Figure 7-5. (a) fluorescent image of PI-PS-P3HT triblock copolymer monolayer deposited from gas region; (b) Photoluminescence spectra of PI-PS-P3HT patterns, as well as P3HT homopolymer in solution and solid state. The scale bar is $5\ \mu\text{m}$.

164

Figure 7-6. Schematic illustration of (a) microstructures of PI-PS-P3HT monolayer. The P3HT phase is shown in red, and PI/PS aggregation in black; and (b) chaining process of dot domain into “pearl-necklace” morphology.

169

Figure 8-1. Pressure -area isotherms P3HT-PDMAEMA diblock copolymer obtained from DI water (red) and NaOH solution (black): (I) liquid region, (II) condensed region.

177

Figure 8-2. AFM height images of the P3HT-PDMAEMA diblock copolymer LB monolayers

obtained from the chloroform solution at gas region(a,b height image, and e,f. corresponding phase images); condensed region (c,d height image, and g,h. corresponding phase images). Scan size is $3\ \mu\text{m} \times 3\ \mu\text{m}$ for a,c,e,g, and, $1\ \mu\text{m} \times 1\ \mu\text{m}$ for b,d,f,h, respectively. The z scale is 50 nm for all images

179

Figure 8-3. TEM image of P3HT-PDMAEMA diblock copolymer monolayer deposited at gas state (a) and condensed state (b), as well as HTEM image of individual domain.

180

Figure 8-4. Schematic illustration of self-assembly process, P3HT aggregation is shown in red, hydrophilic PDMAEMA is shown in yellow, and hydrophobic PDMAEMA is shown in black

181

Figure 8-5. Cross-section analysis of LB film at high pressure.

182

Figure 8-6. Photoluminescence spectra of P3HT-PDMAEMA patterns, as well as P3HT homopolymer in solution and solid state.

183

Figure 8-7. AFM height images of the P3HT-PDMAEMA diblock copolymer LB monolayers obtained under basic water subphase (a,c height image, and b,d. corresponding phase images); Scan size is $3\ \mu\text{m} \times 3\ \mu\text{m}$ for a,b, and $1\ \mu\text{m} \times 1\ \mu\text{m}$ for c,d, respectively. The z scale is 50 nm for all images

186

Abstract

Conjugated polymer–nanocrystals nanohybrids, capitalizing on the advantages peculiar to solution-processable conjugated polymers (CPs) in conjunction with the high electron mobility and tunable optical properties of inorganic nanocrystals (NCs), have attracted considerable attention to achieve high efficiency organic photovoltaics at low cost. The most elegant approach to obtain CP-NC nanohybrids is to chemically tether CPs on the NC surface. In our study, semiconductor organic–inorganic nanocomposites were synthesized by directly grafting CP, poly(3-hexylthiophene), onto cadmium selenide nanorod surface (i.e., preparing P3HT–CdSe NR nanocomposites). The direct grafting was accomplished by two coupling reactions: Heck coupling of vinyl-terminated P3HT with bromobenzylphosphonic acid functionalized CdSe NRs (i.e., BBPA-CdSe), and a newly developed catalyst-free click reaction of ethynyl-terminated P3HT with azide functionalized CdSe NRs. Such rationally designed nanocomposites possessed a well-defined interface between P3HT and CdSe NRs, thereby promoting the effective dispersion of CdSe NRs within the nanocomposites and facilitating their electronic interaction. This is the *first study* of directly placing conjugated copolymers in intimate contact with semiconductor NRs, dispensing with the need for ligand exchange chemistry as in copious past work. These nanocomposites offer a maximum interfacial area between the constituents for efficient exciton dissociation. As such, it represents a significant advance in rational design and fabrication of organic–inorganic hybrid solar cells with improved power conversion efficiency.

As one of the most typical film preparation methods, the Langmuir-Blodgett (LB) technology has been widely utilized to produce copolymer films with mono- or multi-

molecule layers for potential applications in microlithography, devices, and biomimetic thin films. In our study, self-assembly of a series of newly synthesized functional block copolymers (e.g., conjugated, bio-degradable, responsive, etc.) with various novel structures (linear, brush, comb, and star-like) were systematically explored using the LB technique. The influence of the chemical composition and molecular architectures on the self-assembly process was carefully investigated. Various models were proposed to elucidate the complex dynamic self-assembly process. This study not only complements the well-known models of self-assembly of amphiphilic block copolymers at the air/water interface, but also provides a general means of fabricating LB monolayer into controllable structures and integrating the intriguing functionalities in a desirable manner.

Chapter 1. General Introduction

1.1 Organic-Inorganic Nanocomposites Used in Solar Cell

The economy and environment of our times depend on access to reliable, clean, abundant, and affordable energy, including hydropower, nuclear, biomass, wind, geothermal, and solar energies. Among these energy sources, the solar energy represents an effectively unlimited supply of fuel at no cost, and has less issue compared to other sources. The earth receives about 100,000 TW of solar power on its surface, meaning solar energy of one hour can supply humanity's energy needs for a whole year.¹ The calculation performed by the National Renewable Energy Laboratory (NREL) shows that solar panels on all usable residential and commercial roof surfaces could provide the United States with as much electricity per annum as the country used in 2004.¹ Considering the broad desert areas on the earth, for example, the Sahara Desert, the Gobi Desert in central Asia, the Atacama in Peru, and the Great Basin in the United States, the solar energy produced will be far more than enough to be used. Despite its advantages, the electricity generated from solar cells is still limited in a small fraction of our overall energy consumption, primarily due to high cost of manufacturing and installation of the commercial Si solar cells (power conversion efficiency, $PCE = \sim 15\%$).² Although the cost per watt of crystalline Si solar cells has significantly dropped over the past decade,³ its current cost is still in the range of \$0.25–0.40 per watt,¹ making it less competitive without the benefit of government subsidies than conventional electricity grids. The second generation solar cells, based on polycrystalline semiconductor thin films, can bring down the price dramatically. However they still suffer from low efficiency and being practically viable.⁴ With recent advances in nanotechnology, especially in the area

of synthesis^{5,6 7-9} and assembly¹⁰⁻¹⁵ of nanocrystals (NCs), the third generation solar cells based on organic/inorganic nanohybrids has received considerable attention.^{16,17} The solar cells of this kind are believed to be able to provide electricity at extremely low cost if reasonable *PCE* (>10%) and lifetime (> 10 yr) can be attained on a large scale in the near future.¹⁶

The organic/inorganic nanohybrid solar cells are those consisting of interpenetrating phases of semiconducting conjugated polymers (CPs) and NCs as the active components. The p-type CPs and n-type inorganic NCs are selected the electron donor and electron acceptor, respectively. Upon the absorption of photons, the electron of CP is excited from the high occupied molecular orbital (HOMO) to low unoccupied molecular orbital (LUMO) by harvesting a photo with energy greater than the band gap, thereby generating an exciton (i.e., electron-hole pair). Subsequently, the electrons injection (i.e., charge transfer) from CP into NC is energetically favored when the electronic structure of CP and NC are well coupled, which means $E_{\text{NP}}^{\text{A}} - E_{\text{CP}}^{\text{A}} > U_{\text{CP}} - V_{\text{charge transfer}}$,² where E_{NP}^{A} and E_{CP}^{A} are electron affinities of NCs and CPs, respectively, U_{CP} is the Coulombic binding energy of the singlet exciton on the polymer, and $V_{\text{charge transfer}}$ is the Coulombic energy associated with attraction between electron and hole in the final charge-separated state. In general, $V_{\text{charge transfer}}$ is much smaller than U_{CP} and can be ignored due to the increased average electron-hole separation in the charge-separated state.¹⁸ In most CPs, excitons have a binding energy of only a fraction of an eV.^{19,20} The difference in electron affinities of CP and NC is typically around several eV,² which provides enough driving force for the exciton dissociation at the CP/NC interface. In general, the recombination of electrons and holes occurs in the form of the radiative and nonradiative decays of

excitons during the diffusion and dissociation process. Thus, the exciton diffusion length, defined as the average length over which the exciton can diffuse within the polymer before recombination, should be large enough for efficient charge generation, and charge separation process must also be fast enough compared to the radiative and nonradiative decays of the singlet exciton at the CP/NC interface, which typically occur on a time scale of 100-100 picoseconds.² After dissociation, the charges (i.e., electrons and holes) migrate to their respective electrodes under an internal electric field due to the difference in their Fermi levels, thereby generating the photocurrent for external loadings.

The performance of the resulting solar cells is dictated by several factors, including the light absorption efficiency, exciton diffusion efficiency, exciton dissociation efficiency, carrier transport efficiency, and charge collection efficiency at electrodes. More detailed information in this aspect can be found in some review articles.² In this review article, we present the most recent progress on nanohybrid materials used in solar cells. We first introduce the basic optoelectronic properties of NCs and CPs, followed by the recent advances in the CP/NC nanohybrid solar cells, including both prepared by physically mixing CP and NC and chemical integration CP with NC.

1.1.1 CP/NC Composites

Composites of CP/NC are of interest from the standpoint of increased performance relative to either of the non-hybrid counterparts with many applications envisioned in the areas of solar cells²¹⁻²⁴ and LEDs.²⁵⁻²⁸ The pioneer work involving composites of organic CPs and inorganic NCs was reported by Greeham et al in 1996;²⁹ they found that the photoluminescence (PL) quenching of MEH-PPV after mixing it with 5-nm spherical CdS and CdSe NCs. After removal of insulating ligand TOPO on the NC

surface, the quenching was much stronger, which provided evidence for charge transfer. Because once the exciton was dissociated, it can no longer decay radiatively to the ground state. They attributed the observed PL quenching to Forster transfer of the exciton to the NC, followed by decay with a radiative efficiency significantly less than that of MEH-PPV.¹⁸ This property (i.e., PL quenching) facilitates the dissociation of exciton at the NP/CP interface and constitutes the base for composites of CP/NC for use in solar cells. Solar cells fabricated by depositing these composites yielded external quantum efficiency (EQE) of 12% under the low intensity light, and power conversion efficiency (*PCE*) of 0.1% subjected to simulated AM 1.5 G irradiation of 100 mW/cm². Based on the TEM images of these composite films, three problems are clearly evident, which limit further improvement of device performance. First, the NCs tended to aggregate, which reduced the interfaces of NC/CP. As a result, only few excitons would be able to diffuse to the interface and dissociate, leading to incomplete quenching and thus electron transfer. Second, the loosely connected NC network scattered the electron current, and thus less electrons can be collected by electrodes. Finally, the surface of NC was coated with TOPO; these insulating alkyl side chains hindered the efficient electron transfer. Over the past decade, different methods have been proposed to overcome these problems as discussed in detail in the following.

a. Control of Phase Separation

As mentioned above, the aggregation of NCs in composites prepared by physically mixing CP and NC leads to incomplete PL quenching and thus the low electron transfer efficiency. Therefore, a better dispersed NC morphology is favorable for composites for use in solar cells. However, it remains challenging to disperse inorganic

NCs at high density within CPs due to the low solubility of NCs in polymers. The dispersion of NC is governed by the solubility parameter (δ), which is proportional to the square root of cohesive energy density, describing the attractive strength between molecules.² The solubility of a component in solvent increases as the difference between the solubility parameters of the component and solvent decreases. To render good dispersion of NCs, a solvent that dissolve both NCs and CPs is usually required. The solvent is eventually removed in a controllable manner to prevent microphase separation of CPs and NCs. In the pioneering work, Alivisatos et al developed a solvent mixture consisting of one good solvent for NC and another good solvent for CP.²² Specifically, CdSe nanorods were co-dissolved with P3HT in a mixture of pyridine and chloroform, which are good solvents for CdSe and P3HT, respectively. Subsequent spin-coating process enabled the formation of a uniform film composed of dispersed CdSe nanorods in P3HT. Later on, Alivisatos et al introduced the tailor-made solvent to achieve less phase separation.³⁰ By adding the capping ligand to the host solvent, the NCs became more soluble at the expense of the solubility of CP. By varying the concentration of the solvent mixture, phase separation between CP and NC can be tuned from micrometer scale to nanometer scale.³⁰ Specifically, pyridine passivated CdSe nanorods were first dispersed in the mixed solvent of pyridine/chloroform. Pyridine, which hinders the charge transfer from P3HT to CdSe, was then removed by thermal treatment. As a result, the device performance was greatly improved.

An alternative approach to prevent the microphase separation is to modify the ligands that coat on the NC surface to increase their solubility in the CP/NC composites. The phase segregation of NCs is profoundly influenced by their capping ligands.^{31,32}

Carter et al studied the ligand effect on the phase segregation of NCs with commonly used ligands, including butylamine, stearic acid, pyridine, oleic acid, tributylamine.³² Butylamine was found to yield the smallest morphological features of NCs within P3HT, followed by oleic acid, tributylamine, and stearic acid. A better strategy to promote the complete dispersion of NCs in the CP matrix is to directly graft CPs on the NC surface; this will be discussed in Section 4.

b. Improvement of Carrier Transport

In addition to phase separation between CP and NC, the performance of the resulting solar cells is also influenced by the efficiency of electron transport. The electrons have to hop between NCs and are often trapped at the end of the NC network. To improve electron collection, it is desirable to form a well-defined pathway, where few traps exist, to appropriate electrode from the CP/NC interface. Compared to nanodots or sintered NCs, the use of anisotropic nanorods or tetrapods shows a better performance in solar energy conversion due to the fact that the electron has higher mobility along the anisotropic single crystalline nanostructures, where much less defects or trap sites exist compared to the nanodot network. Recent efforts in synthesizing anisotropic nanostructures with well defined geometrical shapes^{33,34} and assembling them in two and three dimensions³⁵ have further expanded the possibility of developing new strategies for enhanced energy conversion. In the pioneering work, Huynh et al discovered that electron transport in the film was improved by utilizing slightly elongated NCs that can effectively pack within the film.³⁶ Later on, they used CdSe nanorods to mix with P3HT to fabricate the P3HT/CdSe nanorods hybrid solar cells.²² Quite intriguingly, the use of these nanorods showed an improved performance and the *PCE* of 1.7% was reported. A

similar observation was made by Janssen et al in the ZnO/poly [2-methoxy-5-(3',7'-dimethyloctyloxy)-1,4-phenylenevinylene] (MDMO-PPV) solar cell,³⁷ where the use of ZnO nanorod led to an improved performance compared to the nanodot counterpart.

As discussed above, one dimensional nanorods carry advantages over nanodots; however, they tend to lie in the plane of the film, which is not the optimal arrangement for electron transport. One way to circumvent this problem is to use branched nanostructures, for example tetrapods or hyperbranched NCs. These nanostructures can individually traverse the thickness of the film and have extensions perpendicular to the substrate, thereby providing continuous pathway for transporting electrons. Greenham et al fabricated composites of CP and branched CdTe NC, which exhibited improved solar cell performance, compared to that of previously reported CP/nanorod composites.³⁸ Under AM 1.5 illumination, the *PCE* of 1.8% was obtained from a device containing 86 wt% NCs. This result suggested that the increase in *PCE* is consistent with improved electron transport perpendicular to the plane of the film. Later on, Alivisatos et al produced ordered CP/NC composites by sequential deposition of CdTe tetrapods and P3HT,³⁹ where the CdTe tetrapods were spontaneously aligned toward the electrodes. The loading and dispersion of tetrapods were easily controlled and characterized. Moreover, the organic and inorganic phases were deposited from their preferred solvents rather than a suboptimal cosolution, therefore the exposure of the NC phase to the top electrode can be controlled. Another way to solve the problem is to pre-form the inorganic phase to maximize the electron mobility, followed by deposition or infiltration of the CP phase. The pre-formed inorganic phase is typically the fused NC network or vertically oriented anisotropic NC arrays. Kang et al demonstrated that the vertically aligned CdTe nanorods

fabricated by electrodeposition can be used to improve the performance of the poly(3-octylthiophene)/CdTe nanohybrid solar cell by providing a high optical absorption, an efficient charge separation, and a fast electron transport at the poly(3-octylthiophene)/CdTe interface.⁴⁰ The *PCE* of 1.06% was achieved by this method. Later on, vertically aligned CdS nanorod arrays were fabricated on Ti substrates and mixed with MEH-PPV.⁴¹ The *PCE* of MEH-PPV based solar cell was improved from 0.0012% to 0.60% when combined with these CdS nanoarrays. ZnO columnar arrays were also used in the nanohybrid solar cells prepared by Peiro et al;⁴² these columnar structures provided a direct and ordered path for photogenerated electrons to the collecting electrode.⁴² Different CPs (MEH-PPV based polymer and P3HT) were compared in these structures and *PCEs* of 0.15 and 0.20% were achieved, respectively. Regarding the fused NC network, Heeger et al infiltrated P3HT into random nanocrystalline TiO₂ networks.⁴³ Various methods, including heat treatment, surface derivatization, and the use of low molecular weight fraction, were utilized to improve the degree of polymer infiltration. This type of solar cells is similar to the dye sensitized solar cell (DSSC), however no liquid electrolyte is needed in the former. It is worth noting that the efficiency reported to date is modest because of poor polymer infiltration. More efforts are still needed to be made in this area.

1.1.2. CP–NP Nanocomposites

Despite various progresses, as CPs and NCs are always in physical contact in the CP/NC composites, it remains difficult to control the detailed morphology and dispersion of NCs within CPs because of the large difference in the solubility of these two components. The interface between CPs and NCs, accomplished by stripping the ligands

from the NC surface during film processing,²³ is not well controlled, thus reducing electronic interactions between them. In this context, chemically tethering NC with CP (i.e., preparing CP–NC nanocomposites with well-controlled interfaces) provides a means of achieving a uniform dispersion of NCs, which carries advantages over cases in which NC aggregation dominates. As a result, efficient light induced electronic interactions between CPs and NCs are promoted. Two main synthetic strategies have been successfully performed to yield CP–NC nanocomposites. In the first strategy, ligand exchange is an essential step to either replace original insulate, small molecules on the NC surface with bifunctional ligands, which contain a second functional group for coupling with conjugated oligomers or polymers or directly exchange for the functionalized conjugated oligomers or polymers in a “grafting onto” process. The second strategy utilizes direct grafting of CPs from/onto functionalized NCs in the absence of ligand exchange chemistry.⁴⁴

a. Ligand Exchange

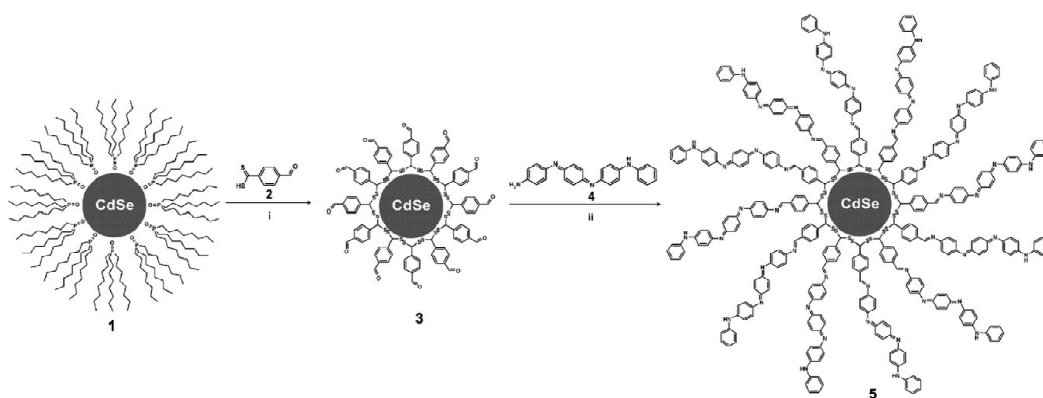


Figure 1-1. Synthetic pathway for the preparation of aniline tetramer/CdSe nanohybrids.

CP–NC nanocomposites can be prepared by exchanging the commonly used, insulate, small molecule-capped NCs with a bifunctional ligand, followed by direct coupling with CPs of interest on the NC surface. The bifunctional ligands consist of the *X-Y-Z* structure, with *X*, *Y*, and *Z* are the functional group for interacting with NCs, the spacer, and the functional group that couples with CPs.⁴⁵ Compared to thiol groups, which are broadly used for ligand exchange due largely to commercial availability. Organic ligands containing the chelating carbodithioate group are excellent binding ligand. They possess higher chemical affinity to NCs by forming strong chelate-type binding with metal atoms, thereby allowing for the nearly quantitative exchange with original ligand (e.g., TOPO) in very mild conditions and thus improving the resistance of NCs against photooxidation as compared to corresponding thiol ligands. Querner et al quantitatively exchanged initial TOPO ligands on the CdSe surface with 4-formyldithiobenzoic acid. The aniline tetramer was subsequently grafted onto the CdSe surface by a condensation reaction between the terminals as shown in Figure 1-1.^{45,46} Recently, Zhang et al used the similar method to graft *rr* P3HT on the CdSe quantum rod (QR) surface, yielding P3HT–CdSe QR nanocomposites.⁴⁷ Specifically, arylbromide-functionalized CdSe QRs were first synthesized by ligand exchange of pyridine-capped CdSe QRs with *p*-bromobenzyl-di-*n*-octylphosphine oxide (DOPO-Br). The vinyl-terminated P3HT was then chemically tethered to the CdSe QR surface by Heck coupling with arylbromide moieties. Compared to the composites of P3HT/pyridine-capped CdSe QRs, the P3HT–CdSe QR nanocomposites exhibited an excellent dispersion of QRs in the P3HT matrix. The solid-state PL measurement on the thin film of nanocomposites

showed quenching of the emission of P3HT, indicating charge transfer from P3HT to CdSe QRs.

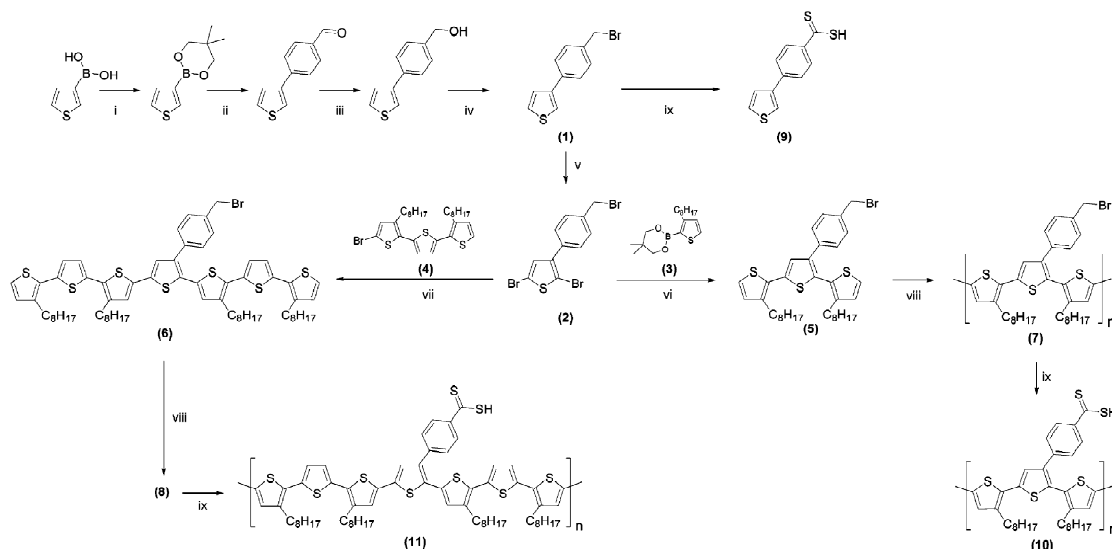


Figure 1-2. Synthetic pathway for the preparation of a family of carbodithioic acid functionalized regioregular oligo- and polythiophene.

Alternatively, the CP–NC nanocomposites can be made by a one-step ligand-exchange reaction with functionalized CPs. In this approach, strong chelating groups (e.g., carbodithioic acid) functionalized CPs or conjugated oligomers (COs) were synthesized first, and was then directly grafted on the NC surface by ligand exchanging with originally capped ligands. For example, Querner et al synthesized a family of carbodithioic acid functionalized *rr* oligo- and polythiophene as follows.⁴⁸ The functionalized thiophene monomer was coupled with oligothiophenes, followed by the oxidative polymerization of the resulting symmetric oligomers. Finally, the carbodithioate moiety was introduced through a post-functionalization reaction as illustrated in Figure 1-2. An efficient quenching of PL was observed in the polythiophene–CdSe nanocomposite, revealing a photoinduced charge transfer at the

interface of polythiophene and CdSe.⁴⁸ Fang et al grafted CdSe NCs with an amine-containing rod-coil triblock copolymer, poly(2 (dimethylamino)ethylmethacrylate)–poly(fluorene)–poly(2-(dimethyl amino) ethylmethacrylate), by directly ligand exchanging with original insulate TOPO ligands.⁴⁹ Recently, Frechet et al synthesized the amine-terminated P3HT, and used it to partially replace TOPO on the CdSe nanorod surface, leading to a high degree of homogeneity.⁵⁰ The partial grafting of P3HT resulted in a better electron transfer, yielding a higher *PCE* in P3HT–CdSe nanorod solar cells. In addition to linear oligothiophene and polythiophene, conjugated oilgothiophene dendrons were also rationally designed and utilized as electroactive surfactants for capping CdSe QDs.^{51,52 89}

b. Direct Grafting

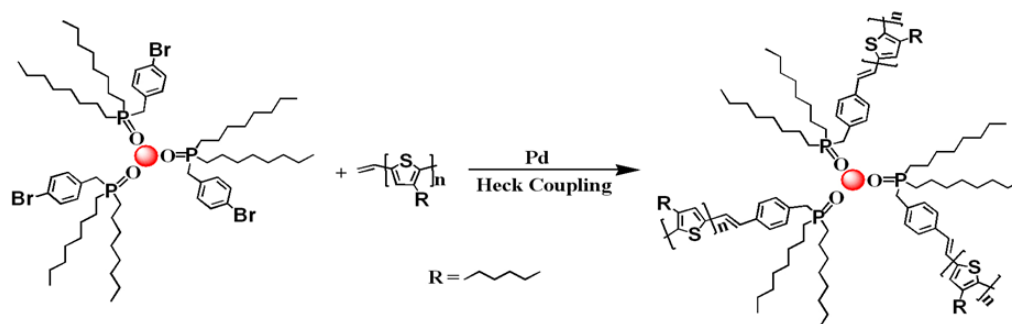


Figure 1-3. Grafting vinyl-terminated P3HT onto [(4-bromophenyl)methyl] dioctylphosphine oxide-functionalized CdSe QDs.

Ligand exchange permits derivatization with a broad range of functional groups on the NC surface. However, it suffers from incomplete surface coverage, although a study on nearly quantitatively exchange has been reported recently.⁴⁵ As a consequence, the fluorescence emission is quenched due to aggregations of QDs,⁵³ or oscillates due to

adsorption and desorption of surface ligand.⁵⁴ Recently, the bifunctional ligand *p*-bromobenzyl-di-octylphosphine oxide (DOPO-Br) was synthesized.⁵⁵ It contains a phosphine oxide moiety serving as the anchoring group to the NC surface, and an arylbromide functionality allowing subsequent surface-initiated reaction. DOPO-Br was used as the capping ligand and replaced TOPO to yield monodispersed DOPO-Br functionalized CdSe QDs. With these QDs, Xu et al grafted relatively longer chain P3HT on the CdSe QD surface via palladium catalyzed Heck coupling, forming P3HT–CdSe QD nanocomposites (Figure 1-3).⁵⁶ The effective charge transfer from P3HT to CdSe in P3HT–CdSe nanocomposites was confirmed by PL as well as PL decay measurements. Subsequently, Goodman et al reported the first study of the behavior of P3HT–CdSe nanocomposites at the air/water interface.⁵⁷ Solar cell fabricated from five Langmuir-Blodgett (LB) deposition cycles of the P3HT–CdSe nanocomposites, approximately 30 nm thick, exhibited a relatively high short circuit current, I_{SC} , while maintaining an ultrathin film profile, yielding a *PCE* of 0.08%.⁵⁷ The ultrathin thickness of active layer, ~30 nm, may result in low light absorption and thus low *PCE*. On the basis of these results, improved photovoltaic performance may be achieved by introducing QDs into CP–QD nanocomposites via forming a better percolation for charge transport, as well as by preparing CP–QR nanocomposites and aligning them in arrays of nanopores that bridge between two electrodes, where the long axis of aligned QRs provide direct pathway for charge transport.

1.2 Self-Assembly of Non-Linear Polymers at the Air/Water Interface: Effect of Molecular Architecture

Due to the surface effect, polymer thin films and micro- or nanostructured

patterns usually adopt different configurations or self-assembled states from those in bulk, resulting in unique surface structures and chemical compositions, and thus, intriguing properties, including friction, shearing, lubrication, abrasion, wetting, adhesion, adsorption, and indentation.⁵⁸⁻⁶² In addition, hierarchical structures composed of polymers that exhibit controlled ordering at different length scales are highly desirable for many applications in optical, electronic, optoelectronic, and magnetic materials and devices.⁶³ Self-assembly has been widely recognized as a most promising route to organizing pre-programmed building blocks into hierarchically ordered structures.⁶⁴⁻⁶⁶ In this context, fundamental understanding of the supramolecular structure and dynamic self-assembly process at the surface is of great importance in designing and engineering new generation polymer films and patterns with novel functional properties. Recent research has witnessed rapid advances in polymer synthesis techniques that yield a myriad of polymers with unique molecular architecture and properties, and their self-assembly in bulk form are fairly well understood.⁶⁷⁻⁶⁹ In stark contrast, their self-assembly in ultrathin films and the resulting supramolecular organization at surfaces and interfaces are far less researched.⁶⁹

One of the most commonly used methods to scrutinize the supramolecular structure and dynamic self-assembly of polymers in ultrathin films or at an interface is the Langmuir–Blodgett (LB) technique, which renders the self-assembly of polymer at an air/water interface under well controlled conditions.⁷⁰⁻⁷² The Langmuir–Blodgett (LB) method, named after Irving Langmuir and Katharine Blodgett, is perhaps the earliest approach to realize what is now called ‘supramolecular assembly’,⁷³ providing the opportunities to exercise molecular level control over the structure of organic thin films.⁷³

Various characterization techniques, including high-resolution x-ray diffraction,⁷⁴⁻⁷⁷ scanning probe microscopy,^{72,78-81} electron microscopy,^{82,83} and Brewster angle optical microscopy⁸⁴⁻⁸⁷ can be integrated with the LB trough and have proven to be effective at addressing many fundamental questions regarding the LB film. Several comprehensive books⁸⁸⁻⁹⁰ and reviews^{72,91,92} describing the state-of-the-art LB method are available, offering many aspects of the background science, from LB film deposition and characterization to applications.

To date, a great diversity of molecules and polymers, primarily linear, have been investigated with the LB technique, and the resulting films have been widely used in the areas of microlithography,⁹³⁻⁹⁶ thin film devices,^{70,72,97-102} and biomimetic films.¹⁰³⁻¹⁰⁶ Among them, linear amphiphilic block copolymer (BCP) is the most well studied system. Ever since the seminal work by Eisenberg and Lennox,¹⁰⁷ the self-assembly of different linear BCPs, e.g., polystyrene-*b*-poly(ethylene oxide) (PS-*b*-PEO)^{93,108,109} and polystyrene-*b*-poly(methyl methacrylate) (PS-*b*-PMMA),¹¹⁰⁻¹¹³ have been intensively investigated, and different models, including “pancake” and “brush” models, have been proposed to successfully illustrate the self-assembly process.^{93,114-117} Upon deposition of these polymers on the water surface, the unfavorable interfacial interaction between the hydrophobic block and water induces the aggregation of hydrophobic blocks, forming different morphologies to reduce the overall free energy of the system. On the other hand, the hydrophilic block tends to adsorb on the water surface or dissolve in the water subphase depending on the surface pressure, forming so-called surface micelles.^{93,108} During this process, the hydrophobic block acts as a buoy, anchoring the polymer chain at the air/water interface and preventing the hydrophilic blocks from dispersing into the

water subphase. Under the applied surface pressure, the hydrophilic blocks are desorbed from the water surface and pushed into the water subphase, yielding the so-called “brush” structure (i.e., transitioning from the “pancake” to the “brush”¹¹⁸). During this transition, the surface area decreases dramatically while the surface pressure is maintained constant, resulting in a plateau region in the isotherm. The length of the plateau region is determined by several parameters, including the ratio of hydrophilic block to hydrophobic block and the chemical composition of BCP. Consequently, three characteristic regions (i.e., liquid, plateau, and condensed regions) are yielded for amphiphilic linear BCPs.

For amphiphilic linear BCPs, the resulting monolayer (supramolecular organization) depends heavily on the characteristics of the blocks (e.g., amphiphilicity, solubility, molecular weight, block ratio, etc.) and processing conditions (e.g., solvent used, concentration of spreading solution, temperature, compression speed, etc.).^{93,107,114,116} Among these variables, the shape of surface micelles of linear BCPs is found to depend mainly on the relative size of the two blocks. Circular micelles are usually formed at high hydrophilic block composition and rod-shaped micelles are preferentially formed when composition of the hydrophilic block is reduced, while a uniform structure of surface micelles is no longer observed if the hydrophilic block content is too low. Therefore, the structure and chemical composition of LB films can be readily tuned by designing the polymer chains and modifying the relative block ratio. These LB films, however, are still limited for use in the areas of surface modification and patterning where self-assembled structures with higher complexity and larger variety are needed.

In order to obtain surface morphologies other than dots and rods (or ribbons), a rational

molecular design that allows for manipulating steric constraint, stacking interaction due to crystallization and π - π stacking, and hydrogen bonding is postulated to be critical to precisely control the self-assembly process. The variation in the shape of molecules, architecture of polymer backbone and specific intermolecular interaction has been proven to be very effective in tailoring the air/water interfacial behavior of polymeric materials.⁶⁹ Thus, polymers with more complex structures have been exploited to modify their self-assembly process and ultimately well controlled morphology. This activity has in turn stimulated the proper design of a large number of polymers with new structures and chemical compositions. To date, self-assembly of many non-linear polymers, including polymer brushes, star copolymers,¹¹⁹⁻¹²³ and dendritic polymers,¹²⁴⁻¹²⁶ at the air/water interface have been studied, in which a broad range of morphologies, such as dots,^{108,123,126,127} spaghetti,^{93,116,127,128} ribbons,^{107,125,126} islands,^{123,125,126} continents,^{127,128} wormlike,¹²⁹ twister,¹³⁰ and bicontinuous network,¹²² were observed.

For non-linear BCPs, the presence of joints, branches, and a low degree of entanglement significantly alters the physical properties compared to their linear counterparts, resulting in a totally different but more controllable self-assembly process.¹³¹ In addition to structural influences (both chemical composition and chemical structure), the functional end groups in non-linear BCPs play a much more important role in determining their self-assembly behaviors. Simple modification of the end group can dramatically affect the physical properties of polymers. As noted above, changing the hydrophobic/hydrophilic ratio is the most viable means of controlling the morphology. In contrast to linear BCPs, in which alteration of the ratio can only be realized by changing the percentage of hydrophobic and hydrophilic blocks, the branched structures in the non-

linear BCPs offer more variables to modify the ratio, including the architectures (e.g., the number of arms in the star-like polymers, grafting density in polymer brushes) and functional end groups because of increased ends at the periphery of the chain, which in turn enable the self-assembly of more much complex yet well controlled structures.

1.2.1 Polymer Brushes

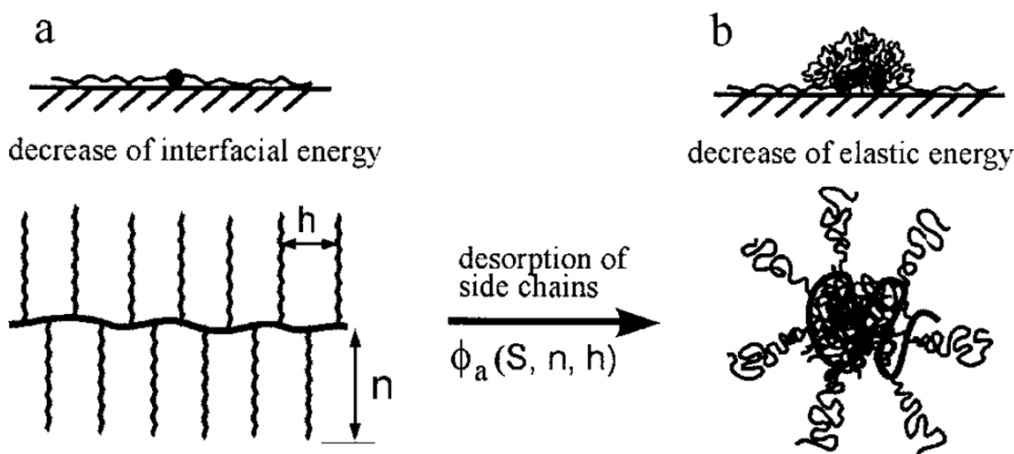


Figure 1-4. Schematic illustration of phase transition of polymer brushes from (a) a rod-like to (b) a globule state caused by partial desorption of side chains. The fraction of adsorbed side chains ϕ_a is a function of spreading coefficient S , the length of side chains n , and the grafting density h . Reprinted with permission from ref. 81, (2001 American Chemical Society).

One the most studied non-linear polymers at the air/water interface is graft polymer,¹³² also known as molecular brush or comb-like polymer. It is typically synthesized by attaching polymer chains along a flexible backbone with different grafting densities.¹³³⁻¹³⁶ Significant advance in synthesis techniques make it feasible to prepare various novel brush-like polymers, including comb-like (identical type of side chains),¹³⁷ centipede (two different types of side chains),¹³⁸ and barbwire (multiple types of side chains)^{138,139}

named based on the presence of side chains, possessing different kinds of architectures (e.g., tadpole,¹⁴⁰ tablet-like,¹⁴¹ and bottle-shaped brushes⁶⁷ defined based on the shape of polymer as whole). Depending on the distribution of side chains along the backbone, polymer brushes are also classified as regular,¹⁴² random,¹³⁴ and gradient brushes.¹⁴³

Beacuse of the steric repulsion of densely grafted side chains, polymer brushes usually adopt a wormlike conformation in solution.¹⁴³⁻¹⁴⁶ When adsorbed on the surface (water or solid substrate), the interaction between the side chain and the surface changes the orientation of the side chain relative to the backbone and breaks the symmetry and the dimensionality of the system,^{147,148} thus allowing for more conformations that depend on the fraction of adsorbed side chains, ϕ_a (Figure 1-4).¹⁴⁹ Two distinct conformations are usually observed, resulting from a competition between the energetically favorable interaction of side chains with the substrate and entropically unfavorable extension of adsorbed side chains. A brush with a high ϕ_a adopts a rod-like conformation (Figure 1-4a). Conversely, a brush with a relatively small ϕ_a prefers a globular conformation favored by the aggregation of desorbed side chains (Figure 1-4b).¹⁴³

1.2.2 *Star-Like Polymers*

Star-like polymers are also an important class of non-linear polymers, in which several linear polymer chains (i.e., arms) are attached to one compact core. These chains can be chemically similar or different, thus producing heteroarm or miktoarm star-like polymers.¹⁵⁰ Star-like polymers with compact, low-generation dendrimers as a core are usually called dendritic stars.^{151,152} The self-assembly of star-like polymers at the air/water interface was studied rather recently due mainly to the difficulty in their synthesis with high structural uniformity.¹³²

Star-like BCP can behave like either a linear BCP or a unimolecular micelle (i.e., composed of single copolymer molecule), or somewhere in between, depending heavily on the number of arms and physical properties of the arms. With an increased number of arms, the molecules become more compact, resulting in less entanglement and more defined supramolecular organization. When absorbing on the surface, the unfavorable interaction with the surface leads to the formation of globular structures,¹⁵³ while the favorable interaction usually allows the arm to spread, adopting an extended conformation.¹⁵⁴⁻¹⁵⁶

1.2.3 Dendritic Polymers

Due to the promising properties stemming from functionalized polymer chains and nanoparticle-like compact molecular architecture, dendritic polymers have received considerable attention over the past decades.¹⁵⁷⁻¹⁶⁴ Two major classes of dendritic polymers are hyperbranched polymers and dendrimers.¹⁶⁵ Dendrimers have regular, tree-like architectures, divergent from a single, point-like core with very regular branches radically extending from a single center.¹³² Because of well-defined globular architecture, the dendrimers at the air/water interface have been extensively investigated.¹²⁶ The “edge on” and “face on” models have been widely used to explain the self-assembly of a variety of dendrimers at the air/water interface.¹²⁶ We refer the reader to several comprehensive reviews on dendrimers and their assemblies.¹⁶⁶⁻¹⁶⁹ Here we only focus on the hyperbranched polymers with tree-like architecture, which are quite similar to dendrimers but have a lower degree of branching and less regular architecture.¹³² The morphology and overall shape of hyperbranched polymers as well as their interfacial behavior can also be altered by modifying the internal chemical architecture, the nature and

distribution of terminal group, and the strength of the polymer/surface interaction.^{126,170} Compared to dendrimers, despite the similarity in architecture, hyperbranched polymers show a much different self-assembly process, which is due to the much higher molecular weight and less defined architectures.

1.2.4 *Linear-Dendritic Polymers*

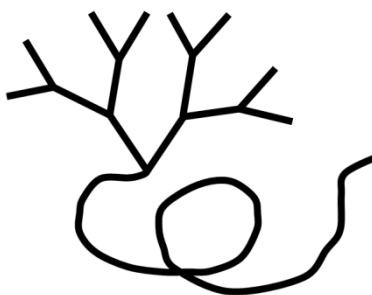


Figure 1-4. Molecular structure of linear-dendritic polymer.

As noted previously, dendritic polymers are monodisperse, tree-like macromolecules with a regular and highly branched architecture consisting of a dendritic core and peripheral sites. This peculiar structural feature opens many opportunities for using them in drug delivery (serving as host for foreign molecules),¹⁷¹ interfacial liquid membranes for stabilizing aqueous-organic emulsion, catalysis and reaction sites,¹⁷² etc. However, such compact a structure often leads to little or no entanglements, thus limiting certain applications where highly robust and cohesive films are needed. One way to overcome this problem is to capitalize on a dendrimeric polymer containing a linear block or segment (Figure 1-4). The linear block increases entanglements, thus enhancing the mechanical integrity, whereas the self-assembly nature of BCPs can be exploited to assist the assembly of organized films.¹⁷³ Most importantly, the unique properties of dendritic

polymer can be well retained in linear-dendritic polymers. Because of such a novel hybrid structure, intriguing interfacial behavior may be expected when self-assembled at the air/water interface. Compared with the non-linear polymers discussed above, linear-dendritic polymers cover a wider range of materials, but have received far less attention to date.

References:

- (1) Schiermeier, Q.; Tollefson, J.; Scully, T.; Witze, A.; Morton, O. *Nature* 2008, 454, 816.
- (2) Saunders, B. R.; Turner, M. L. *Adv. Colloid Interface Sci.* 2008, 138, 1.
- (3) Shah, A.; Torres, P.; Tscharnner, R.; Wyrsh, N.; Keppner, H. *Science* 1999, 285, 692.
- (4) Kamat, P. V. *J. Phys. Chem. C* 2008, 112, 18737.
- (5) Manna, L.; Scher, E. C.; Alivisatos, A. P. *J. Cluster Sci.* 2002, 13, 521.
- (6) Peng, X. G. *Adv. Mater.* 2003, 15, 459.
- (7) Dong, H. X.; Yang, Z.; Yang, W. Y.; Yin, W. Y.; Song, Y. Z.; Yang, H. Q. *Prog. Chem.* 2006, 18, 1608.
- (8) Wang, F. D.; Buhro, W. E. *J Am Chem Soc* 2007, 129, 14381.
- (9) Yu, H.; Li, J. B.; Loomis, R. A.; Gibbons, P. C.; Wang, L. W.; Buhro, W. E. *J Am Chem Soc* 2003, 125, 16168.
- (10) Li, L. S.; Alivisatos, A. P. *Advanced Materials* 2003, 15, 408.
- (11) Ghezelbash, A.; Koo, B.; Korgel, B. A. *Nano Letters* 2006, 6, 1832.
- (12) Hu, Z. H.; Fischbein, M. D.; Querner, C.; Drndic, M. *Nano Letters* 2006, 6, 2585.
- (13) Ryan, K. M.; Mastroianni, A.; Stancil, K. A.; Liu, H. T.; Alivisatos, A. P. *Nano Letters* 2006, 6, 1479.
- (14) Kang, C. C.; Lai, C. W.; Peng, H. C.; Shyue, J. J.; Chou, P. T. *Acs Nano* 2008, 2, 750.
- (15) Querner, C.; Fischbein, M. D.; Heiney, P. A.; Drndic, M. *Advanced Materials* 2008, 20, 2308.
- (16) Coakley, K. M.; McGehee, M. D. *Chem. Mater.* 2004, 16, 4533.
- (17) Jayadevan, K. P.; Tseng, T. Y. *J. Nanosci. Nanotechnol.* 2005, 5, 1768.

- (18) Ginger, D. S.; Greenham, N. C. *Phys. Rev. B: Condens. Matter* 1999, 59, 10622.
- (19) Campbell, I. H.; Hagler, T. W.; Smith, D. L.; Ferraris, J. P. *Phys. Rev. Lett.* 1996, 76, 1900.
- (20) Alvarado, S. F.; Seidler, P. F.; Lidzey, D. G.; Bradley, D. D. C. *Phys. Rev. Lett.* 1998, 81, 1082.
- (21) Greenham, N. C.; Peng, X.; Alivisatos, A. P. *Phys. Rev. B.* 1996, 54, 17628.
- (22) Huynh, W. U.; Dittmer, J. J.; Alivisatos, A. P. *Science* 2002, 295, 2425.
- (23) Milliron, D. J.; Alivisatos, A. P.; Pitois, C.; Edder, C.; Frechet, J. M. J. *Adv. Mater.* 2003, 15, 58.
- (24) Milliron, D. J.; Gur, I.; Alivisatos, A. P. *MRS Bulletin* 2005, 30, 41.
- (25) Odoi, M. Y.; Hammer, N. I.; Sill, K.; Emrick, T.; Barnes, M. D. *J. Am. Chem. Soc.* 2006, 128, 3506.
- (26) Colvin, V. L.; Schlamp, M. C.; Alivisatos, A. P. *Nature* 1994, 370, 354.
- (27) Coe, S.; Woo, W. K.; Bawendi, M.; Bulovis, V. *Nature* 2002, 420, 800.
- (28) Lee, J.; Sundar, V. C.; Heine, J. R.; Bawendi, M. G.; Jensen, K. F. *Adv. Mater.* 2000, 12, 1102.
- (29) Greenham, N. C.; Peng, X. G.; Alivisatos, A. P. *Phys. Rev. B: Condens. Matter* 1996, 54, 17628.
- (30) Huynh, W. U.; Dittmer, J. J.; Libby, W. C.; Whiting, G. L.; Alivisatos, A. P. *Adv. Funct. Mater.* 2003, 13, 73.
- (31) Aldakov, D.; Chandezon, F.; De Bettignies, R.; Firon, M.; Reiss, P.; Pron, A. *Eur. Phys. J. Appl. Phys.* 2006, 36, 261.
- (32) Olson, J. D.; Gray, G. P.; Carter, S. A. *Sol. Energy Mater. Sol. Cells* 2009, 93, 519.
- (33) Peng, Z. A.; Peng, X. G. *JACS* 2002, 124, 3343.

- (34) Manna, L.; Scher, E. C.; Alivisatos, A. P. *J. Am. Chem. Soc.* 2000, *122*, 12700.
- (35) Schierhorn, M.; Boettcher, S. W.; Ivanovskaya, A.; Norvell, E.; Sherman, J. B.; Stucky, G. D.; Moskovits, M. *J. Phys. Chem. C* 2008, *112*, 8516.
- (36) Huynh, W. U.; Peng, X. G.; Alivisatos, A. P. *Adv. Mater.* 1999, *11*, 923.
- (37) Beek, W. J. E.; Wienk, M. M.; Kemerink, M.; Yang, X. N.; Janssen, R. A. J. *J. Phys. Chem. B* 2005, *109*, 9505.
- (38) Sun, B. Q.; Marx, E.; Greenham, N. C. *Nano Letters* 2003, *3*, 961.
- (39) Gur, I.; Fromer, N. A.; Alivisatos, A. P. *Journal of Physical Chemistry B* 2006, *110*, 25543.
- (40) Kang, Y. M.; Park, N. G.; Kim, D. *Appl Phys Lett* 2005, 86.
- (41) Kang, Y.; Kim, D. *Sol. Energy Mater. Sol. Cells* 2006, *90*, 166.
- (42) Peiro, A. M.; Ravirajan, P.; Govender, K.; Boyle, D. S.; O'Brien, P.; Bradley, D. D. C.; Nelson, J.; Durrant, J. R. *J. Mater. Chem.* 2006, *16*, 2088.
- (43) Bartholomew, G. P.; Heeger, A. J. *Adv. Funct. Mater.* 2005, *15*, 677.
- (44) Lin, Z. Q. *Chem-Eur J* 2008, *14*, 6294.
- (45) Querner, C.; Reiss, P.; Bleuse, J.; Pron, A. *JACS* 2004, *126*, 11574.
- (46) Querner, C.; Reiss, P.; Sadki, S.; Zagorska, M.; Pron, A. *PCCP* 2005, *7*, 3204.
- (47) Zhang, Q. L.; Russell, T. P.; Emrick, T. *Chem Mater* 2007, *19*, 3712.
- (48) Querner, C.; Benedetto, A.; Demadrille, R.; Rannou, P.; Reiss, P. *Chem. Mater.* 2006, *18*, 4817.
- (49) Fang, C.; Qi, X. Y.; Fan, Q. L.; Wang, L. H.; Huang, W. *Nanotechnology* 2007, *18*.
- (50) Liu, J. S.; Tanaka, T.; Sivula, K.; Alivisatos, A. P.; Frechet, J. M. J. *JACS* 2004, *126*, 6550.

- (51) Locklin, J.; Patton, D.; Deng, S. X.; Baba, A.; Millan, M.; Advincula, R. C. *Chem. Mater.* 2004, *16*, 5187.
- (52) Advincula, R. C. *Dalton Trans.* 2006, 2778.
- (53) Kalyuzhny, G.; Murray, R. W. *J. Phys. Chem. B* 2005, *109*, 7012.
- (54) Komoto, A.; Maenosono, S.; Yamaguchi, Y. *Langmuir* 2004, *20*, 8916.
- (55) Skaff, H.; Sill, K.; Emrick, T. *JACS* 2004, *126*, 11322.
- (56) Xu, J.; Wang, J.; Mitchell, M.; Mukherjee, P.; Jeffries-EL, M.; Petrich, J. W.; Lin, Z. Q. *JACS* 2007, *129*, 12828.
- (57) Goodman, M. D.; Xu, J.; Wang, J.; Lin, Z. Q. *Chem. Mat.* 2009, *21*, 934.
- (58) Luzinov, I.; Minko, S.; Tsukruk, V. V. *Prog. Polym. Sci.* 2004, *29*, 635.
- (59) Albert, J. N. L.; Epps, T. H. *Mater. Today* 2010, *13*, 24.
- (60) Park, H. W.; Jung, J.; Chang, T. *Macromol. Res.* 2009, *17*, 365.
- (61) Hamley, I. W. *Prog. Polym. Sci.* 2009, *34*, 1161.
- (62) Kim, J. K.; Lee, J. I.; Lee, D. H. *Macromol. Res.* 2008, *16*, 267.
- (63) Kim, J. S.; McHugh, S. K.; Swager, T. M. *Macromolecules* 1999, *32*, 1500.
- (64) Schweikart, A.; Horn, A.; Boker, A.; Fery, A. *Complex Macromolecular Systems I* 2010, 227, 75.
- (65) Keizer, H. M.; Sijbesma, R. P. *Chem. Soc. Rev.* 2005, *34*, 226.
- (66) Forster, S. *Colloid Chemistry I* 2003, 226, 1.
- (67) Hamley, I. W. *Angew. Chem. Int. Ed.* 2003, *42*, 1692.
- (68) Klok, H. A.; Lecommandoux, S. *Adv. Mater.* 2001, *13*, 1217.
- (69) Tsukruk, V. V. *Prog. Polym. Sci.* 1997, *22*, 247.
- (70) Davis, F.; Higson, S. P. J. *Biosens. Bioelectron.* 2005, *21*, 1.

- (71) Acharaya, S.; Shundo, A.; Hill, J. P.; Ariga, K. *J. Nanosci. Nanotechnol.* 2009, 9, 3.
- (72) Zasadzinski, J. A.; Viswanathan, R.; Madsen, L.; Garmaes, J.; Schwartz, D. K. *Science* 1994, 263, 1726.
- (73) Talham, D. R.; Yamamoto, T.; Meisel, M. W. *J. Phys.: Cond. Matt.* 2008, 20.
- (74) Qiu, Y. F.; Chen, P. L.; Liu, M. H. *J Am Chem Soc* 2010, 132, 9644.
- (75) Shibata, T.; Ebina, Y.; Ohnishi, T.; Takada, K.; Kogure, T.; Sasaki, T. *Cryst. Growth Des.* 2010, 10, 3787.
- (76) Penza, M.; Tagliente, M. A.; Aversa, P.; Re, M.; Cassano, G. *Nanotechnology* 2007, 18.
- (77) Chen, Y. L.; Liu, H. G.; Zhu, P. H.; Zhang, Y.; Wang, X. Y.; Li, X. Y.; Jiang, J. Z. *Langmuir* 2005, 21, 11289.
- (78) Jandt, K. D. *Mater. Sci. Eng., R* 1998, 21, 221.
- (79) Fujihira, M. *Annu. Rev. Mater. Sci.* 1999, 29, 353.
- (80) Bottomley, L. A.; Coury, J. E.; First, P. N. *Anal. Chem.* 1996, 68, R185.
- (81) Vansteenkiste, S. O.; Davies, M. C.; Roberts, C. J.; Tendler, S. J. B. *Prog. Polym. Sci.* 1998, 57, 95.
- (82) Collins, S. J.; Dhathathreyan, A.; Ramasami, T.; Mohwald, H. *Thin Solid Films* 2000, 358, 229.
- (83) Kimura, S.; Kusano, H.; Kitagawa, M.; Kobayashi, H. *Appl. Surf. Sci.* 1999, 142, 579.
- (84) Santos, T. C. F.; Peres, L. O.; Wang, S. H.; Oliveira, O. N.; Caseli, L. *Langmuir* 2010, 26, 5869.
- (85) Gutierrez-Campos, A.; Castillo, R. *Rev. Mex. Fis.* 2010, 56, 339.
- (86) Wang, J.; Qiu, L. U.; Jakli, A.; Weissflog, W.; Mann, E. K. *Liq. Cryst.* 2010, 37, 1229.

- (87) Giner, I.; Gascon, I.; Vergara, J.; Lopez, M. C.; Ros, M. B.; Royo, F. *M. Langmuir* 2009, 25, 12332.
- (88) Roberts, G. G. *Langmuir-Blodgett films* 1990.
- (89) Petty, M. C. *Langmuir-Blodgett films : an introduction* 1996.
- (90) Ulman, A. *An introduction to ultrathin organic films : from Langmuir-Blodgett to self-assembly* 1991.
- (91) Ulman, A. *Chem. Rev.* 1996, 96, 1533.
- (92) Peng, J. B.; Barnes, G. T.; Gentle, I. R. *Adv. Colloid Interface Sci.* 2001, 91, 163.
- (93) Cheyne, R. B.; Moffitt, M. G. *Langmuir* 2006, 22, 8387.
- (94) Li, T. S.; Xu, W. J.; Zhou, J.; Wang, J.; Xu, Z. H.; Wu, Y. J.; Miyashita, T. *Proceedings of the 2009 2nd International Congress on Image and Signal Processing, Vols 1-9* 2009, 2813.
- (95) Boker, A.; Lin, Y.; Chiapperini, K.; Horowitz, R.; Thompson, M.; Carreon, V.; Xu, T.; Abetz, C.; Skaff, H.; Dinsmore, A. D.; Emrick, T.; Russell, T. P. *Nature Mater.* 2004, 3, 302.
- (96) Li, X. D.; Aoki, A.; Miyashita, T. *Macromolecules* 1997, 30, 2194.
- (97) Fasolka, M. J.; Harris, D. J.; Mayes, A. M.; Yoon, M.; Mochrie, S. G. *J. Phys. Rev. Lett.* 1997, 79, 3018.
- (98) Pepe, I. M.; Nicolini, C. *J. Photochem. Photobiol., B* 1996, 33, 191.
- (99) Metzger, R. M. *J. Solid State Chem.* 2002, 168, 696.
- (100) Kaneto, K.; Kudo, K.; Ohmori, Y.; Onoda, M.; Iwamoto, M. *IEICE Trans. Electron.* 1998, E81C, 1009.
- (101) Ducharme, S.; Reece, T. J.; Othon, C. M.; Rannow, R. K. *IEEE Trans. Device Mater. Reliab.* 2005, 5, 720.
- (102) Valli, L. *Adv. Colloid Interface Sci.* 2005, 116, 13.

- (103) Aksay, I. A.; Trau, M.; Manne, S.; Honma, I.; Yao, N.; Zhou, L.; Fenter, P.; Eisenberger, P. M.; Gruner, S. M. *Science* 1996, 273, 892.
- (104) Simon, A.; Girard-Egrot, A.; Sauter, F.; Pudda, C.; D'Hahan, N. P.; Blum, L.; Chatelain, F.; Fuchs, A. *J. Colloid Interface Sci.* 2007, 308, 337.
- (105) Rybak, B. M.; Ornatska, M.; Bergman, K. N.; Genson, K. L.; Tsukruk, V. V. *Langmuir* 2006, 22, 1027.
- (106) Gradwell, S. E.; Renneckar, S.; Esker, A. R.; Heinze, T.; Gatenholm, P.; Vaca-Garcia, C.; Glasser, W. *C.R. Biol.* 2004, 327, 945.
- (107) Zhu, J.; Eisenberg, A.; Lennox, R. B. *Macromolecules* 1992, 25, 6547.
- (108) Baker, S. M.; Leach, K. A.; Devereaux, C. E.; Gragson, D. E. *Macromolecules* 2000, 33, 5432.
- (109) Deschenes, L.; Bousmina, M.; Ritcey, A. M. *Langmuir* 2008, 24, 3699.
- (110) Chung, B.; Choi, H.; Park, H. W.; Ree, M.; Jung, J. C.; Zin, W. C.; Chang, T. *Macromolecules* 2008, 41, 1760.
- (111) Seo, Y.; Cho, C. Y.; Hwangbo, M.; Choi, H. J.; Hong, S. M. *Langmuir* 2008, 24, 2381.
- (112) Lopes, S. I. C.; Goncalves da Silva, A.; Brogueira, P.; Picarra, S.; Martinho, J. M. G. *Langmuir* 2007, 23, 9310.
- (113) Carvalho, A. J. F.; Ferreira, M.; Balogh, D. T.; Oliveira, O. N.; Faria, R. M. *J. Phys. Chem. B* 2004, 108, 7033.
- (114) daSilva, A. M. G.; Filipe, E. J. M.; dOliveira, J. M. R.; Martinho, J. M. G. *Langmuir* 1996, 12, 6547.
- (115) Cox, J. K.; Yu, K.; Eisenberg, A.; Lennox, R. B. *Phys. Chem. Chem. Phys.* 1999, 1, 4417.
- (116) Cheyne, R. B.; Moffitt, M. G. *Langmuir* 2005, 21, 5453.
- (117) Park, J. Y.; Koenen, N.; Forster, M.; Ponnappati, R.; Scherf, U.; Advincula, R. *Macromolecules* 2008, 41, 6169.

- (118) Szleifer, I. *Europhys. Lett.* 1998, 44, 721.
- (119) Francis, R.; Skolnik, A. M.; Carino, S. R.; Logan, J. L.; Underhill, R. S.; Angot, S.; Taton, D.; Gnanou, Y.; Duran, R. S. *Macromolecules* 2002, 35, 6483.
- (120) Ornatska, M.; Bergman, K. N.; Rybak, B.; Peleshanko, E.; Tsukruk, V. V. *Angew. Chem. Int. Ed.* 2004, 43, 5246.
- (121) Ornatska, M.; Peleshanko, S.; Genson, K. L.; Rybak, B.; Bergman, K. N.; Tsukruk, V. V. *J Am Chem Soc* 2004, 126, 9675.
- (122) Genson, K. L.; Hoffman, J.; Teng, J.; Zubarev, E. R.; Vaknin, D.; Tsukruk, V. V. *Langmuir* 2004, 20, 9044.
- (123) Gunawidjaja, R.; Peleshanko, S.; Tsukruk, V. V. *Macromolecules* 2005, 38, 8765.
- (124) Peleshanko, S.; Sidorenko, A.; Larson, K.; Villavicencio, O.; Ornatska, M.; McGrath, D. V.; Tsukruk, V. V. *Thin Solid Films* 2002, 406, 233.
- (125) Njikang, G. N.; Cao, L.; Gauthier, M. *Langmuir* 2008, 24, 12919.
- (126) Njikang, G. N.; Cao, L.; Gauthier, M. *Macromol. Chem. Phys.* 2008, 209, 907.
- (127) Cox, J. K.; Yu, K.; Constantine, B.; Eisenberg, A.; Lennox, R. B. *Langmuir* 1999, 15, 7714.
- (128) Devereaux, C. A.; Baker, S. M. *Macromolecules* 2002, 35, 1921.
- (129) Holzmüller, J.; Genson, K. L.; Park, Y.; Yoo, Y. S.; Park, M. H.; Lee, M.; Tsukruk, V. *Langmuir* 2005, 21, 6392.
- (130) Cheng, C. X.; Jiao, T. F.; Tang, R. P.; Chen, E. Q.; Liu, M. H.; Xi, F. *Macromolecules* 2006, 39, 6327.
- (131) Ornatska, M.; Bergman, K. N.; Goodman, M.; Peleshanko, S.; Shevchenko, V. V.; Tsukruk, V. V. *Polymer* 2006, 47, 8137.
- (132) Peleshanko, S.; Tsukruk, V. V. *Prog. Polym. Sci.* 2008, 33, 523.

- (133) Tsukahara, Y.; Tsutsumi, K.; Yamashita, Y.; Shimada, S. *Macromolecules* 1990, 23, 5201.
- (134) Borner, H. G.; Duran, D.; Matyjaszewski, K.; da Silva, M.; Sheiko, S. *S. Macromolecules* 2002, 35, 3387.
- (135) Schappacher, M.; Deffieux, A. *Macromolecules* 2000, 33, 7371.
- (136) Liu, Y. F.; Abetz, V.; Muller, A. H. E. *Macromolecules* 2003, 36, 7894.
- (137) Borner, H. G.; Beers, K.; Matyjaszewski, K.; Sheiko, S. S.; Moller, M. *Macromolecules* 2001, 34, 4375.
- (138) Mays, J. W.; Uhrig, D.; Gido, S.; Zhu, Y. Q.; Weidisch, R.; Iatrou, H.; Hadjichristidis, N.; Hong, K.; Beyer, F.; Lach, R.; Buschnakowski, M. *Macromol. Symp.* 2004, 215, 111.
- (139) Hirao, A.; Kawano, H.; Ryu, S. W. *Polym. Adv. Technol.* 2002, 13, 275.
- (140) Fu, G. D.; Phua, S. J.; Kang, E. T.; Neoh, K. G. *Macromolecules* 2005, 38, 2612.
- (141) Huang, Y.; Liu, X. B.; Zhang, H. L.; Zhu, D. S.; Sun, Y. J.; Yan, S. K.; Wang, J.; Chen, X. F.; Wan, X. H.; Chen, E. Q.; Zhou, Q. F. *Polymer* 2006, 47, 1217.
- (142) Zhang, B.; Fischer, K.; Schmidt, M. *Macromol. Chem. Phys.* 2005, 206, 157.
- (143) Lord, S. J.; Sheiko, S. S.; LaRue, I.; Lee, H. I.; Matyjaszewski, K. *Macromolecules* 2004, 37, 4235.
- (144) Fredrickson, G. H. *Macromolecules* 1993, 26, 2825.
- (145) Saariaho, M.; Subbotin, A.; Ikkala, O.; ten Brinke, G. *Macromol. Rapid Commun.* 2000, 21, 110.
- (146) Wintermantel, M.; Gerle, M.; Fischer, K.; Schmidt, M.; Wataoka, I.; Urakawa, H.; Kajiwar, K.; Tsukahara, Y. *Macromolecules* 1996, 29, 978.

- (147) Khalatur, P. G.; Khokhlov, A. R.; Prokhorova, S. A.; Sheiko, S. S.; Moller, M.; Reineker, P.; Shirvanyanz, D. G.; Starovoitova, N. *Eur. Phys. J. E* 2000, *1*, 99.
- (148) Potemkin, I. I.; Khokhlov, A. R.; Reineker, P. *Eur. Phys. J. E* 2001, *4*, 93.
- (149) Sheiko, S. S.; Moller, M. *Chem. Rev.* 2001, *101*, 4099.
- (150) Teng, J.; Zubarev, E. R. *J Am Chem Soc* 2003, *125*, 11840.
- (151) Trollsas, M.; Claesson, H.; Atthoff, B.; Hedrick, J. L. *Angew. Chem. Int. Ed.* 1998, *37*, 3132.
- (152) Xu, J.; Luo, S. Z.; Shi, W. F.; Liu, S. Y. *Langmuir* 2006, *22*, 989.
- (153) Hua, F. J.; Ruckenstein, E. *Macromolecules* 2005, *38*, 888.
- (154) Kiriya, A.; Gorodyska, G.; Minko, S.; Stamm, M.; Tsitsilianis, C. *Macromolecules* 2003, *36*, 8704.
- (155) Kiriya, A.; Gorodyska, G.; Minko, S.; Tsitsilianis, C.; Jaeger, W.; Stamm, M. *J Am Chem Soc* 2003, *125*, 11202.
- (156) Gorodyska, G.; Kiriya, A.; Minko, S.; Tsitsilianis, C.; Stamm, M. *Nano Lett.* 2003, *3*, 365.
- (157) Tomalia, D. A. *Adv. Mater.* 1994, *6*, 529.
- (158) Percec, V.; Chu, P. W.; Ungar, G.; Zhou, J. P. *J Am Chem Soc* 1995, *117*, 11441.
- (159) Jansen, J. F. G. A.; Debrabandervandenberg, E. M. M.; Meijer, E. W. *Science* 1994, *266*, 1226.
- (160) Gao, C.; Yan, D. *Prog. Polym. Sci.* 2004, *29*, 183.
- (161) Matthews, O. A.; Shipway, A. N.; Stoddart, J. F. *Prog. Polym. Sci.* 1998, *23*, 1.
- (162) Jikei, M.; Kakimoto, M. *Prog. Polym. Sci.* 2001, *26*, 1233.

- (163) Hult, A.; Johansson, M.; Malmstrom, E. *Branched Polymers II* 1999, **143**, 1.
- (164) Patri, A. K.; Majoros, I. J.; Baker, J. R. *Curr. Opin. Chem. Biol.* 2002, **6**, 466.
- (165) Zhai, X.; Peleshanko, S.; Klimenko, N. S.; Genson, K. L.; Vaknin, D.; Vortman, M. Y.; Shevchenko, V. V.; Tsukruk, V. V. *Macromolecules* 2003, **36**, 3101.
- (166) Al-Jamal, K. T.; Ramaswamy, C.; Florence, A. T. *Adv. Drug Delivery Rev.* 2005, **57**, 2238.
- (167) Singh, P. *Biotechnol. Appl. Biochem.* 2007, **48**, 1.
- (168) Lee, H.; Larson, R. G. *Molecules* 2009, **14**, 423.
- (169) Samad, A.; Alam, M. I.; Saxena, K. *Curr. Pharm. Des.* 2009, **15**, 2958.
- (170) Wells, M.; Crooks, R. M. *J Am Chem Soc* 1996, **118**, 3988.
- (171) Meijer, E. W. *Science* 1994, **266**, 1226.
- (172) Bosman, A. W., Janssen, H.M., and Meijer, E.W. *Chem Rev.* 1999, **1665**.
- (173) Iyer, J.; Hammond, P. T. *Langmuir* 1999, **15**, 1299.

Chapter 2. Anisotropic Nanocomposites via Directly Coupling Conjugated

Polymers with Quantum Rods

2.1 Introduction

Conjugated polymers (CPs) have received considerable attention as promising materials for use in organic photovoltaics, light-emitting diodes (LEDs), thin film transistors, and biosensors.¹ Among various types of CPs, poly(3-hexylthiophene) (P3HT) is one of the most widely studied organic semiconductors. P3HT possesses excellent solution processability, environmental stability, high charge carrier mobility, and tailorable electrochemical properties.² Due to their quantum-confined nature, for quantum dots (QDs) such as cadmium selenide (CdSe),³ variation of nanocrystal size provides continuous and predictable changes in fluorescence emission, rendering them useful for a wide range of applications in photovoltaic cells,^{4,5} LEDs,⁶ biosensors,⁷ and bio-imaging.⁷

CP-based organic/inorganic hybrid solar cells (e.g., CP/QD composites) are favorable alternatives to inorganic solar cells as they carry many advantages peculiar to CPs, such as light weight, flexibility, processability, roll-to-roll production, low cost, and large area. However, the CP/QD composites are widely prepared by simply *physically mixing* CP and QD, which suffers from several severe problems, including microscopic phase separation and the existence of insulating interfacial layers,⁸ thereby reducing the interfacial area between CP and QD and limiting the performance of the resulting devices. Recently, various methods have been utilized to overcome these problems, such as the use of co-solvent mixture⁹ or binary solvent mixture,¹⁰ and surface modification of QDs.⁸ The most elegant approach is to *chemically tether* CPs on the QD surface (i.e., preparing CP–QD nanocomposites), enabling direct electronic coupling between CP and QD.^{8,11}

Notably, this strategy has only recently been developed and primarily implemented via ligand exchange, which permits the derivatization with a broad range of functional groups.⁸ However, ligand exchange chemistry suffers from incomplete surface coverage.⁸

2.2 Result and Discussion

In this context, recently P3HT–CdSe QD nanocomposites have been synthesized by *directly* grafting vinyl-terminated P3HT onto [(4-bromophenyl)methyl]dioctylphosphine oxide (DOPO-Br) functionalized CdSe QD surface via a mild palladium-catalyzed Heck coupling without the need for ligand exchange.¹² The ability to manipulate the shape of nanocrystals has led to quantum rods (hereafter refer to as nanorods; NRs) with diameters ranging from 2 to 10 nm and lengths ranging from 5 to 100 nm.³ Due to their intrinsic structural anisotropy, NRs possess many unique properties that make them potentially better nanocrystals than QDs for photovoltaics and biomedical applications. Photovoltaic cells made of NRs and CPs show an improved optical absorption in the red and near-infrared ranges originating from the NRs.^{4,5} Moreover, the long axis of NRs provides continuous paths for transporting electrons, an advantage over QDs where electron hopping between QDs is required.⁹ The performance of photovoltaic cells can be further improved if NRs are vertically aligned between two electrodes to minimize the carrier transport pathways.¹³ It is noteworthy that although CP–NR nanocomposites were recently produced by ligand exchange of CPs with insulating ligands that were originally bonded on the NR surface,¹⁴ *direct* grafting of CPs onto anisotropic nanocrystals has not yet been explored.

Herein, we report one simple yet robust route to CP–NR nanocomposites, dispensing with the need for ligand exchange chemistry. In this strategy, the catalyst free alkyne–azide cycloaddition, which belongs to an emerging field of click chemistry,¹⁵ was utilized in the preparation of P3HT–CdSe NR nanocomposites. As shown in scheme 2-1, CdSe NRs were passivated with bromobenzylphosphonic acid (BBPA) which not only induced elongated growth but also functionalized the CdSe NR surface, forming BBPA-CdSe NRs. Subsequently, the aryl bromide of BBPA was converted into azide functional group, forming N₃-BPA-CdSe NRs. Finally catalyst-free Huisgen 1,3-dipolar cycloaddition between ethynyl-terminated P3HT and N₃-BPA-CdSe NRs successfully yielded intimate P3HT-CdSe NR nanocomposites without introducing any deleterious metallic impurity. Compared with the heck coupling mainly used in the present P3HT grafting works, the click reaction possessed several attractive features, including an extremely versatile bond formation process, no requirement of protecting groups, good selectivity, nearly complete conversion, and generally no need for purification.¹⁶ As such, it stands out as a promising method to simplify the synthesis procedure and opens opportunities to increase the grafting density for large-scale synthesis. The charge transfer occurred at the P3HT/CdSe

NR interface and was confirmed by systematic UV-Vis absorption, photoluminescence (PL), and time-resolved PL studies.

It has been demonstrated that end-functional P3HT can be successfully grafted onto [(4-bromophenyl)methyl]dioctylphosphine oxide (DOPO-Br) functionalized CdSe QD surface through Heck coupling of aryl bromide of DOPO-Br with vinyl end group of P3HT.¹² Quite intriguingly, however, the strategy of preparing (DOPO-Br) capped CdSe QDs was not effective in the synthesis of DOPO-Br capped CdSe NRs,¹⁴ as phosphine oxide, the capping group on DOPO-Br, was not a suitable ligand to induce elongated growth of CdSe nanocrystals.³ Growth in phosphine oxide occurred too rapidly at the high monomer concentration desired for the elongated growth. Thus the resulting nanocrystals are primarily isotropic dot-like.³ By contrast, phosphoric acid, coordinating more strongly than phosphine oxide, is very effective at adjusting the growth rate of nanocrystals and raising the energy of (001) faces of CdSe wurtzite structure, which leads to the formation of elongated structures.^{3,17} Moreover, a recent NMR study showed that phosphoric acid is the only capping ligand on the elongated CdSe structure, even though an excess amount of phosphine oxide was used as the solvent.¹⁸ Taken together, in order to enable the ligands not only bear functional group, i.e., aryl bromide (converted into azide) that can react with end-functional P3HT via click reaction, but also can strongly anchor to the NR surface, new bifunctional ligands with phosphonic group and aryl bromide at each end are needed.

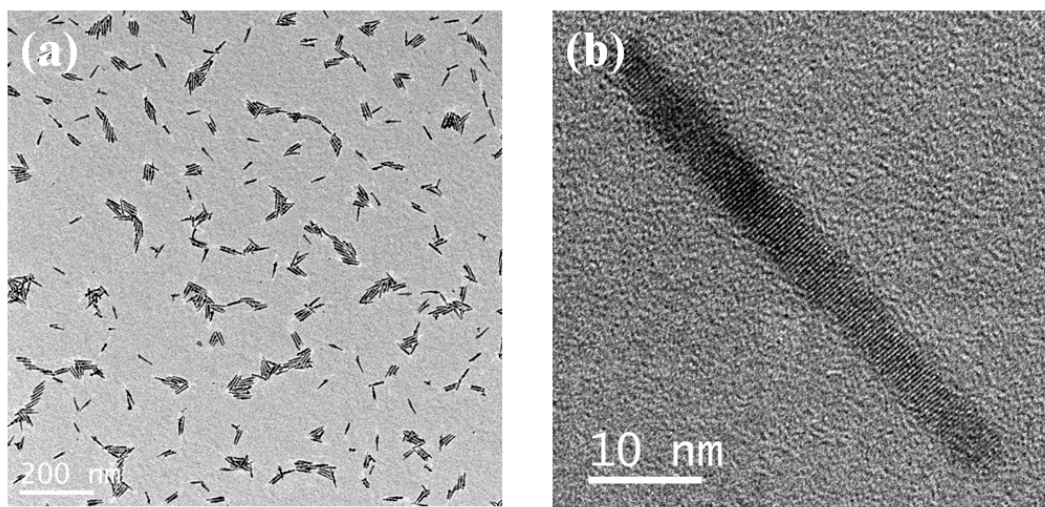


Figure 2-1. TEM images of (a) BBPA-functionalized CdSe NRs, and (b) close-up of an individual NR

2. Result and discussion

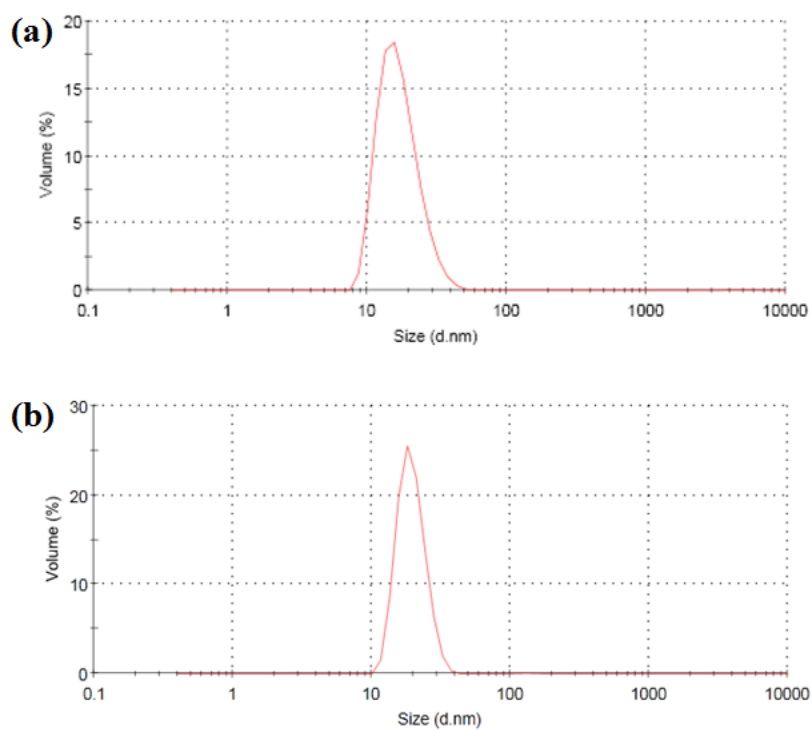


Figure 2-2. Dynamic light scattering (DLS) measurements on (a) BBPA functionalized CdSe NRs; and (b) P3HT-CdSe NR nanocomposites prepared by click reaction.

To this end, bromobenzylphosphonic acid (BBPA; bearing aryl bromide end group) functionalized CdSe NRs were synthesized based on a ligand-exchange free procedure (see *Experimental Section*). The TEM measurements revealed a high quality one-dimensional CdSe NR morphology with wurtzite structure (Figure 2-1a) and dimensions of 40 ± 5.6 nm in length and 5 ± 0.7 nm in diameter (Figure 2-1b). The local weak aggregation was due to the self-assembly of BBPA-CdSe NRs on the TEM grid after solvent evaporation.³ The NRs possessed monodispersed size distribution as evidenced by the dynamic light scattering (DLS) measurement in which a relatively narrow single peak was observed (Figure 2-2a). The anchoring of BBPA on CdSe was detected by the solution-based ³¹P-NMR after ligand recovery process (see *Supporting Information*); this is due to the confinement of ligand vibration by solid surface.¹⁹ The ³¹P-NMR of octadecylphosphonic acid (ODPA; 27.66ppm) and BBPA (21.29ppm) exhibited similar intensity despite the initial molar ratio of ODPA:BBPA = 5:1 (Figure 3). Compared with ODPA, BBPA has much shorter chain length and thus much higher reactivity due to less steric hindrance during the monomer diffusion and crystal growth process.^{17,18} This result was consistent with a previous study using hexylphosphonic acid (HPA) and tetradecane phosphoric acid (TDPA) mixture to grow CdSe NRs, where more active HPA also predominately covered the NR surface.²⁰ Additionally, in the present study no peak of TOPO (solvent) was observed (data not shown), which is due to its much weaker capping ability as compared to phosphoric acid; this is in good agreement with previously reported work.^{19,20}

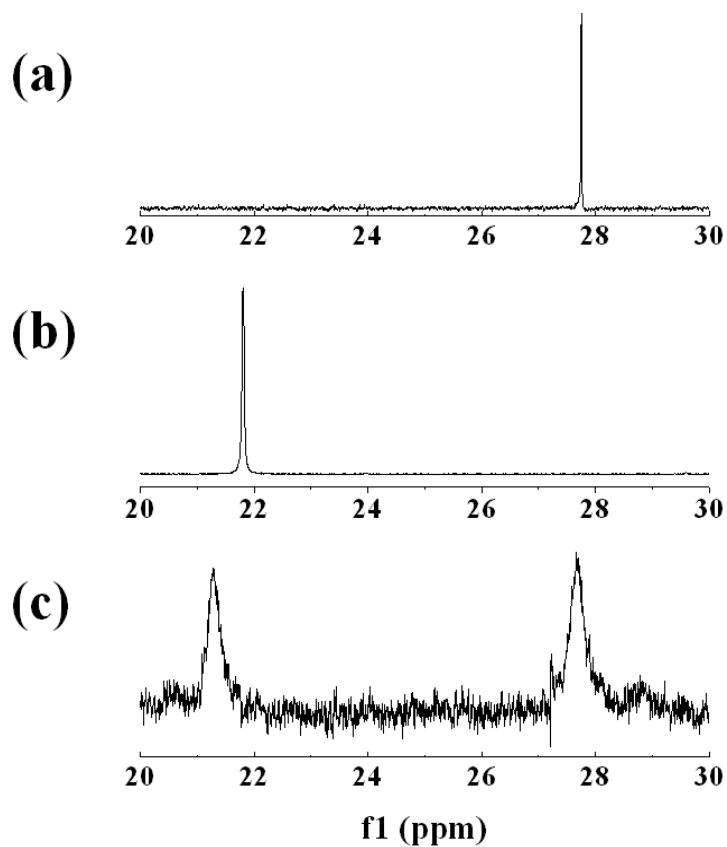


Figure 2-3. ^{31}P NMR spectra of (a) pure ODPA, (b) pure BBPA, and (c) CdSe-BBPA and CdSe-ODPA complex (see Supporting Information: BBPA ligand recovery for NMR analysis).

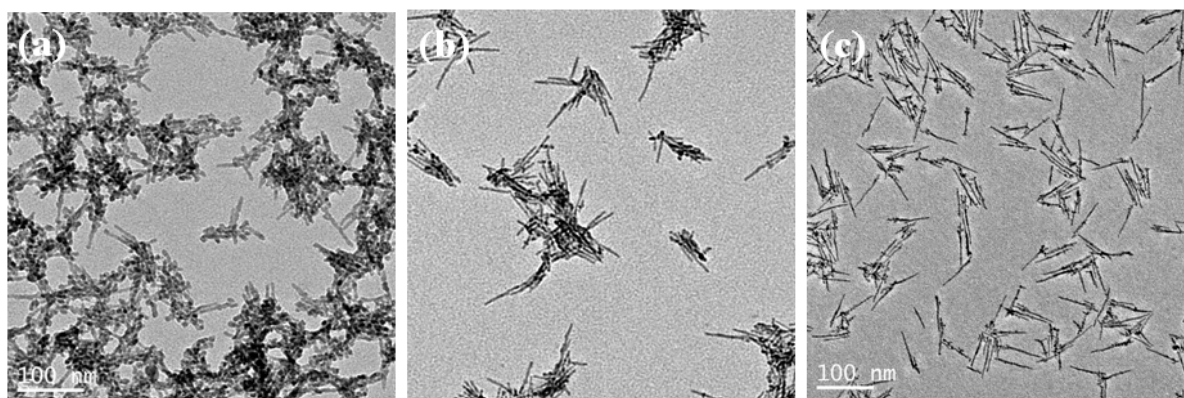


Figure 2-4. TEM images of CdSe NRs synthesized with (a) BBPA solely, (b) ODPA/BBPA mixture at 1:1 molar ratio, and (c) ODPA/BBPA mixture at 3:1 molar ratio.

The addition of ODPa as a co-ligand was found to play an important role in producing high quality, well-dispersed elongated nanocrystals. Growth with BBPA solely led to the formation of highly aggregated elongated nanostructures (Figure 2-4a) due to poor stabilization of BBPA in relatively low polar organic solvent (i.e., THF and toluene used in the study), in which P3HT, however, was fully dissolved during the grafting process. Furthermore, a lower molar ratio of ODPa in the ligand mixture (i.e., ODPa:BBPA = 1:1 and 3:1) generally led to less well-defined nanostructures possessing more branches, kinks, and non-uniform cross sections along the diameter of the NRs (Figure 2-4b and 2-4c). The presence of sufficient ODPa acted as the monomer buffer (i.e., metal-organic precursors) in conjunction with BBPA, effectively regulating the monomer concentration during the nanocrystal growth.²⁰ Otherwise, the highly active BBPA-Cd precursor would greatly accelerate the growth process, resulting in structures more susceptible to lattice defects (e.g., stacking faults, twinning defects, etc.²¹).

Click reaction has been widely recognized as an attractive route for the functionalization of a variety of nanomaterials with high yield, including Au nanoparticles,²² carbon nanotubes,²³ and QDs.²⁴ To the best of our knowledge, *no* study has been performed on direct grafting of conjugated polymers onto nanocrystals using click reaction. In the present study the synthesis of P3HT–CdSe NR nanocomposites was accomplished as follows (Scheme 2-1). First, aryl bromide of BBPA was converted into an azide group by adding NaN₃ in the BBPA-CdSe solution. As NaN₃ cannot be dissolved quite well in organic solvents (i.e., THF), a long time reaction over a period of three days was carried out to ensure complete conversion to yield azide-benzylphosphonic acid capped CdSe (i.e., N₃-BPA-CdSe). Subsequently, the azide group

of N₃-BPA-CdSe reacted with ethynyl-terminated P3HT to form 1, 2, 3-triazole, thus grafting P3HT onto the CdSe NR surface (see *Experimental Section*). Notably, the use of catalysts (e.g., copper) was avoided in this process as metallic impurities can be easily bonded to the nanocrystal surface, making it difficult to remove from the product, which is deleterious to the performance of nanocomposite solar cells.

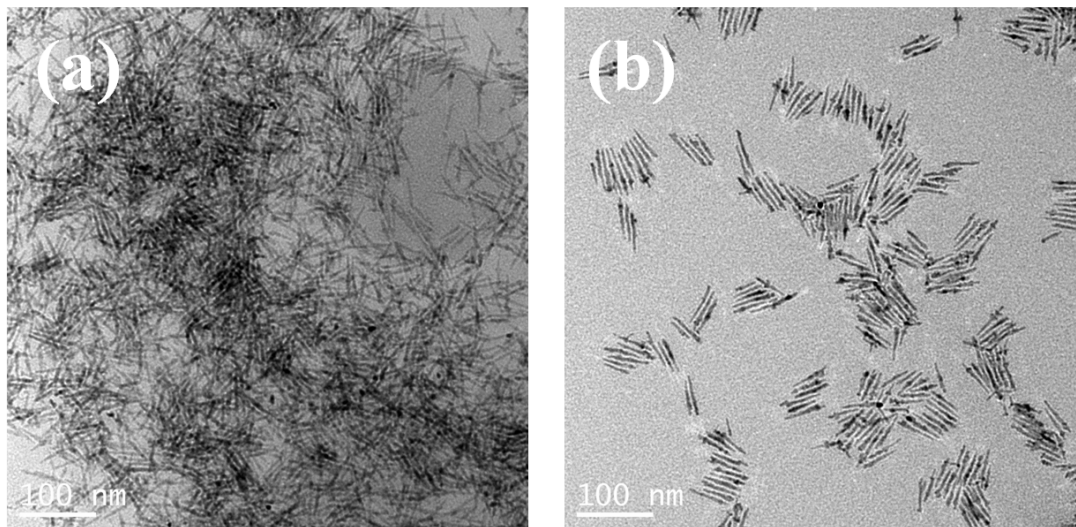


Figure 2-5. TEM images of P3HT/CdSe NR composites prepared by (a) physically mixing ethynyl-terminated P3HT and azide-benzylphosphonic acid functionalized CdSe NRs, and (b) P3HT-CdSe NR nanocomposites synthesized by click reaction

The color of the solution changed from brown (CdSe) to light purple (P3HT) after the reaction and subsequent purification, indicating P3HT was grafted onto CdSe NRs. TEM images of P3HT/CdSe NR composites prepared by physically blending ethynyl-terminated P3HT and BBPA-CdSe, and P3HT-CdSe NR nanocomposites are shown in Figure 2-5a and 2-1b, respectively. Compared to the physical mixture counterpart, which showed significant phase segregation (Figure 2-5a) and thus reduced the interfacial area needed for charge separation, CdSe NRs were well dispersed within the P3HT-CdSe NR nanocomposites as evidenced in Figure 2-5b. The self-assembly of nanocomposites was

clearly evident, which can be attributed to strong dipole-dipole interaction of CdSe NRs broadly observed in the elongated nanostructures (Figure 2-5b).³ The P3HT/CdSe weight ratio in the composites (~1: 3.358) was made to be the same as that of the nanocomposites; the ratio in the latter was determined by TGA measurements (Figure 2-6). Notably, the P3HT–CdSe NR nanocomposites can also be readily dispersed in the P3HT homopolymer matrix (Figure 2-7) in comparison to phase segregation seen in the P3HT/CdSe composites (Figure 2-5a).⁸ It is interesting to note that no clear grafted P3HT at the periphery of CdSe NRs was imaged by TEM (Figure 2-7a) due to the low electron density of P3HT compared to inorganic NRs.¹² However, the existence of P3HT grafting can be indirectly verified by the DLS measurement, which had been proven to be an effective method to confirm the coating at the surface of NRs (e.g., Au).²⁵ After P3HT grafting, the average size of NRs actually increased from 17.37 nm to 19.56 nm (Figure 2-2).

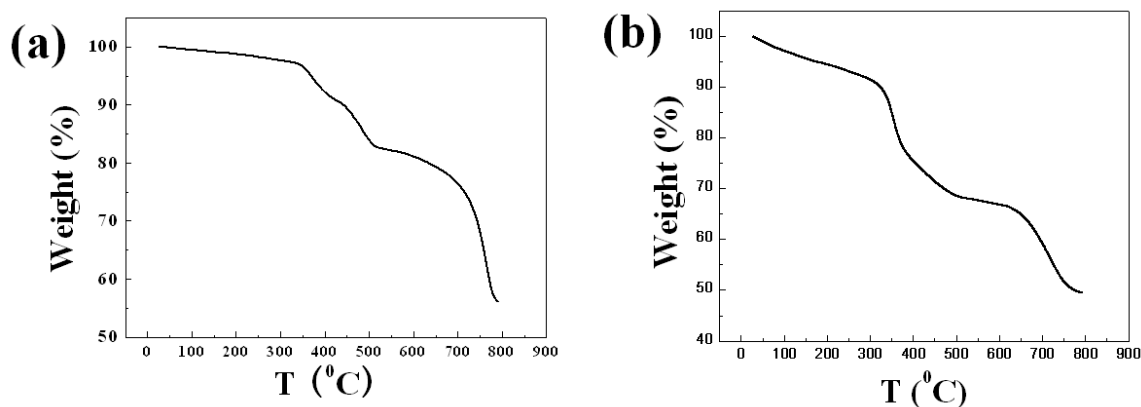


Figure 2-6. Thermogravimetry analysis (TGA) of (a) BBPA functionalized CdSe NRs, (b) P3HT-CdSe NR nanocomposites prepared by click reaction.

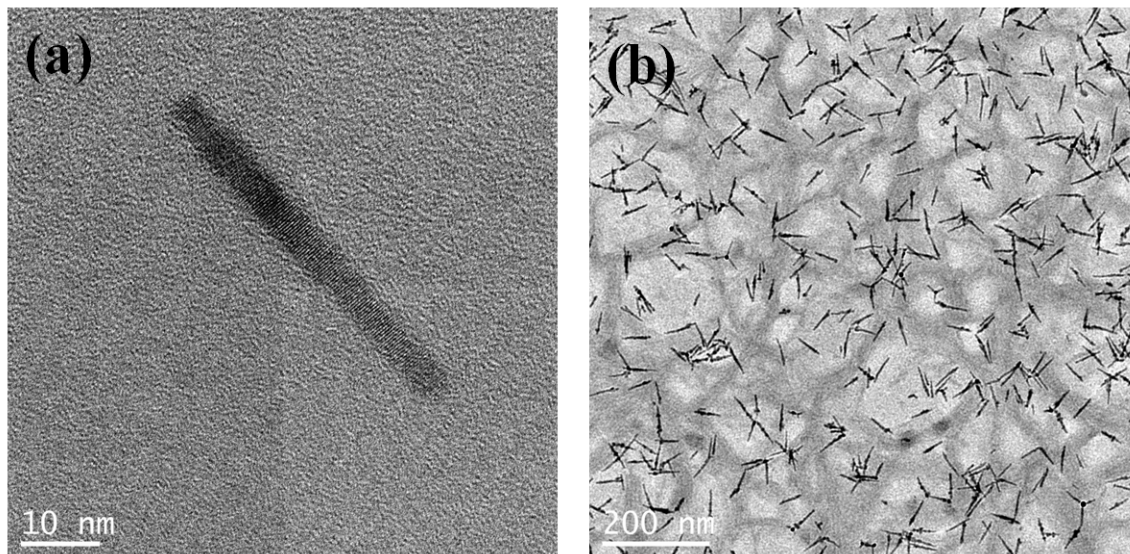


Figure 2-7. (a) HRTEM image of P3HT-CdSe NR nanocomposites synthesized by click reaction, and (b) TEM image of nanocomposites in a P3HT homopolymer matrix. The P3HT matrix is clearly evident on the background of TEM images, appearing dark and/or grey.

The success of coupling of ethynyl-terminated P3HT with N_3 -BPA-CdSe NRs was confirmed by solution ^1H -NMR. Compared with molecules and QDs, NRs are large in volume, the vibration of bonded P3HT was strongly confined under magnetic wave, resulting in low resolution NMR signal of the coupling group nearby the NR surface.¹⁹ Therefore, a dissociation procedure was employed to detach grafted P3HT chain from the NR surface, and thus P3HT coupled with BBPA ligand can be characterized in a free unbonded state (see *Supporting Information*). After click reaction, the proton signal from thiophene ring at 6.98 ppm was observed,^{8,12} and it was shifted to 6.88 ppm after dissociation of P3HT, indicating that P3HT was originally bonded to CdSe (Figure 2-9). Furthermore, The proton signal at 3.5 ppm (i.e., peak i) from the ethynyl group on P3HT (Figure 2-10) disappeared after click reaction (Figure 2-10b), signifying P3HT was successfully grafted onto CdSe. Additionally, the signal of proton from thiophene ring

connected with ethynyl group (i.e., peak h) also disappeared due to the absence of influence of ethynyl group after forming cycloaddition. The grafting density of P3HT chains was determined by thermogravimetry analysis (TGA) (Figure 2-6). The molecular weight of CdSe NRs was estimated to be 9.81×10^6 g/mol based on TEM images shown in Figure 2-1, and the P3HT/CdSe weight ratio was 1 : 3.358 from TGA. Thus the P3HT/CdSe molar ratio was approximately ~560:1, much higher than that obtained from ligand exchange approach, which was 250:1.¹⁴

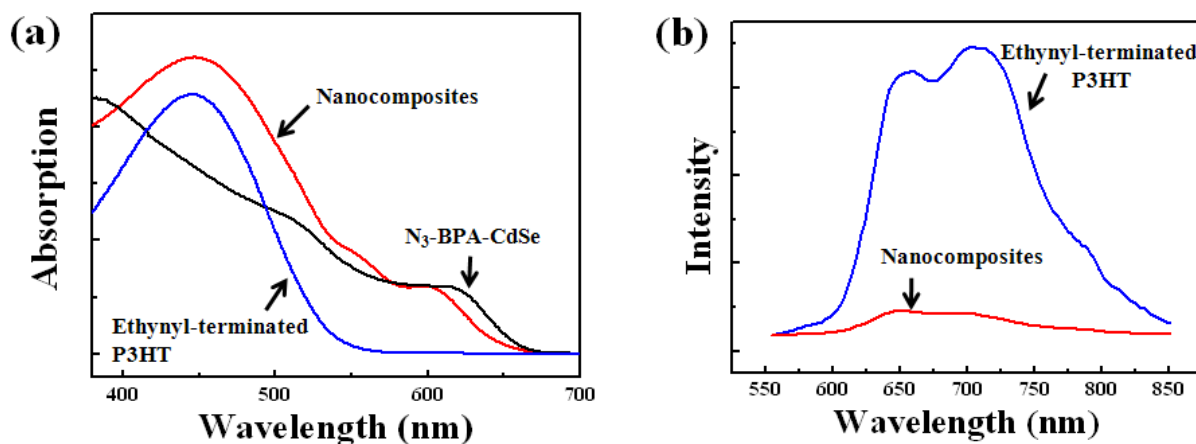


Figure 2-8. (a) Absorption spectra of azide-benzylphosphonic acid functionalized CdSe NRs (black curve), ethynyl-terminated P3HT (blue curve), and P3HT-CdSe nanocomposites prepared by click reaction (red curve). (b) Emission spectra of ethynyl-terminated P3HT (blue curve) and nanocomposites (red curve) in dry state.

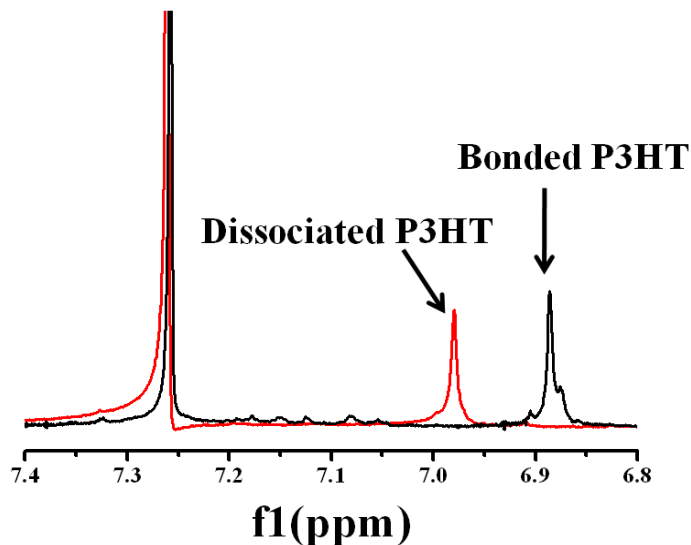


Figure 2-9. ^1H NMR spectra of P3HT in chloroform that was grafted on CdSe (black) and P3HT after detached from the CdSe NR surface (red) in the nanocomposites prepared by click reaction.

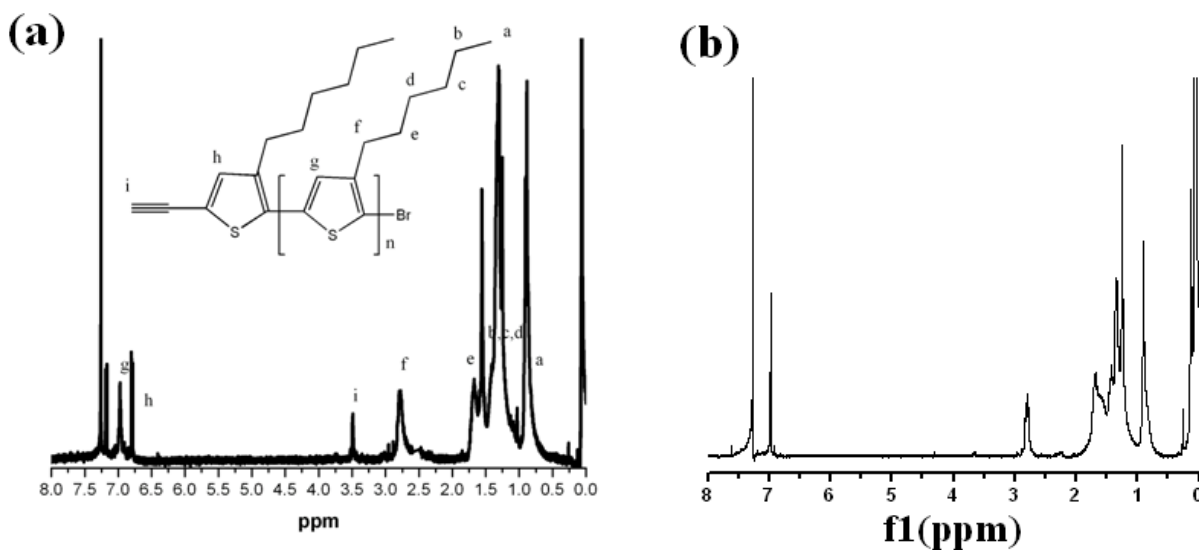


Figure 2-10. (a) ^1H NMR spectrum of ethynyl-terminated P3HT, and (b) ^1H NMR spectrum of P3HT detached from the CdSe NR surface in the nanocomposites prepared by click reaction.

The photophysical properties of the resulting P3HT–CdSe NR nanocomposites were explored by absorption and solid state photoluminescence (PL) studies. Figure 2-8 shows the absorption spectra of N_3 -BPA-CdSe NR, ethynyl-terminated P3HT, and P3HT–CdSe

NR nanocomposites in THF. The absorption maxima for P3HT and CdSe NRs were at 448nm and 615nm, respectively. It is clear that the absorption spectrum of nanocomposites was the sum of the absorption spectra of its constituents, which served as additional evidence of successful coupling of nanocomposites. Moreover, the absorption spectrum also revealed the effect of P3HT coating on the band structure of CdSe NRs (Figure 2-8). The absorption maximum was blue-shifted from 615 nm in N₃-BPA-CdSe to 601 nm in P3HT–CdSe nanocomposites, which can be attributed to (i) the changes in the dielectric environment (i.e., grafting a layer of P3HT) that perturb the energy of quantum-confined excitation,²⁶ or (ii) enhanced confinement of electron wave function due to increased exciton-free dead layer thickness on the CdSe NR surface.²⁷ The dry nanocomposite film was characterized by PL measurement, which was acquired from the sample sealed in an Ar-filled vial to prevent possible photodegradation (Figure 2-8b).²⁸ The vibronic structures of ethynyl-terminated P3HT were clearly evident.¹² By contrast, a nearly complete quenching of P3HT fluorescence was seen, implying efficient charge transfer from P3HT to CdSe NRs. This observation further confirmed intimate chemical contact between P3HT and CdSe.¹⁴ Furthermore, the emission of P3HT at 710nm after bonded on the CdSe surface was also blue-shifted to 697nm. As the electronic structure of conjugated polymers is strongly related to their configuration,²⁹ the blue-shift may be associated with a different configuration state of P3HT on CdSe surface than in crystallized bulk.

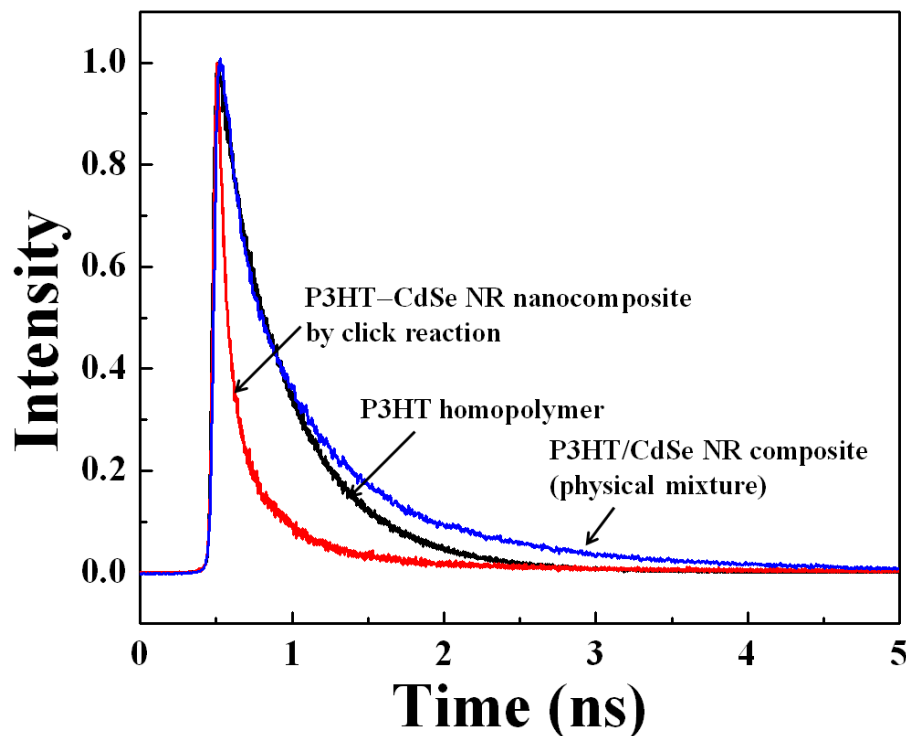


Figure 2-11. Normalized time-resolved photoluminescence decays of P3HT, physical mixture of P3HT/BBPA-CdSe NR, P3HT-CdSe nanocomposites prepared by click coupling, respectively, monitored at $\lambda_{\text{exc}} = 407$ nm and $\lambda_{\text{em}} \geq 500$ nm. The curve fitting yielded the average lifetimes of 370 ps for P3HT, 320 ps for P3HT/CdSe NR composite, and 105 ps for P3HT-CdSe nanocomposites via click reaction, respectively.

In order to provide additional information on the charge transfer dynamics in P3HT-CdSe nanocomposites, time-resolved PL measurements (i.e., ultrafast emission dynamics) monitored at the wavelength above 500 nm were performed by measuring the fluorescence lifetime using time-correlated single-photon counting (TCSPC) methodology (Figure 2-11). The solid state dynamics took place on the picosecond time scale and involved the diffusion of electronic excitations from P3HT to CdSe.¹² The measurements revealed that P3HT/CdSe composites (i.e., mixture of P3HT homopolymer and BBPA-CdSe) had a fluorescence lifetime of 320 ps, close to a 370 ps lifetime for

P3HT homopolymer; this is because the charge transfer between P3HT and CdSe was hindered by the insulating ligands (i.e., BBPA and ODPA) as well as the strong phase segregation in composites.¹² The P3HT–CdSe nanocomposites formed by click coupling, however, exhibited a much faster lifetime of 105 ps, an important signature of an improved interfacial contact between P3HT and CdSe. The direct chemical anchoring of P3HT on CdSe made it easy for excitons to find the interface and dissociate, representing a rapid charge transfer from P3HT to CdSe.^{12,13} This result was well correlated with the static PL study (Figure 2-8b). The charge transfer led to the PL quenching since the photogenerated exciton was dissociated before luminescence occurred.

2.3 Conclusion

In summary, semiconductor organic–inorganic nanocomposites were successfully synthesized by directly grafting end-functional conjugated polymers onto anisotropic nanocrystals that possessed complimentary functional groups for coupling reaction. A simple yet robust “grafting-onto” strategy was exploited to create P3HT–CdSe NR nanocomposites, namely, catalyst-free click reaction of ethynyl-terminated P3HT with azide-benzylphosphonic acid functionalized CdSe NRs, thereby affording direct contact between P3HT and CdSe and dispensing with the need for ligand exchange chemistry as in copious previous work. The success of the formation of nanocomposite was confirmed by NMR and DLS measurements. The CdSe NRs can be well dispersed within the resulting nanocomposites. The grafting density of P3HT was greatly increased as compared to that using conventional ligand exchange approach. The solid-state emission spectra of nanocomposite suggested the charge transfer from P3HT to CdSe. A much

faster lifetime (i.e., fast exciton dissociation at the P3HT/CdSe interface) for the nanocomposites prepared by click reaction was observed. Such nanocomposites, in which P3HT and CdSe NRs are intimately contacted, may be very promising for use in organic–inorganic hybrid solar cells with improved power conversion efficiency due to (i) an increased interfacial contact between conjugated polymers and one-dimensional nanocrystals, and (ii) vectorial pathways provided by the long axis of NRs when they are aligned perpendicularly between two electrodes for effective exciton dissociation and transport. This is the subject of current study.

2.4 Experimental Section

All chemicals, including 4-bromobenzyl bromide, triethyl phosphate, cadmium oxide (CdO), tri-n-octylphosphine oxide (TOPO), sodium azide (NaN_3), tert-Butylmagnesium chloride (2mol/L in diethyl ether), and ethynylmagnesium bromide (0.5mol/L in THF) purchased from Sigma Aldrich, and tetra decyl phosphonic acid (TDPA), octadecyl phosphonic acid (ODPA) purchased from PCI synthesis were used as received. THF (Fisher, 99%) was refluxed over sodium wire and distilled from sodium naphthalenide solution.

Synthesis of bromobenzylphosphonic acid (BBPA). Mixture of 4-bromobenzyl bromide and triethyl phosphite (molar ratio = 1:2) was heated and stirred under Ar at 150 °C for 5 h to yield diethylphosphonate ester. The excess triethyl phosphite and byproducts were then removed by heating at 100 °C under vacuum for several hours. After that, diethylphosphonate ester was hydrolyzed to yield BBPA by adding excess concentrated aqueous HCl and heated at 100°C overnight. After cooling down to room

temperature, the BBPA was filtered out, and then redissolved in CH₃CN. The addition of CH₃CN and its evaporation using rotary evaporator were repeated for three times to remove trace amount of water and HCl. Finally BBPA was recrystallized using ethyl acetate to obtain pure product.

Yield: 56%. ¹H NMR(300MHz, DMSO-d₆): 7.46 (d, 2H, *J* =7.6Hz), 7.19 (d, 2H, *J* =7.4Hz), (AA'XX', 4H), 2.94 (d, 2H, *J* =21 Hz)

Synthesis of BBPA capped CdSe NRs. A mixture of 67 mg BBPA, 333 mg ODPa, 1.5g TOPO, and 0.1 g CdO was first degassed in a 25 ml three-neck flask connected to a Liebig condenser at room temperature in vacuum and subsequently at 120°C for 60 min. It was then slowly heated under Ar until CdO decomposed and the solution turned clear and colorless. Next, 0.7 ml TOP was added, and the temperature was further raised to 320 °C. 36 mg selenium dissolved in 0.5 ml TOP was rapidly injected to the vigorously stirred Cd precursor. The CdSe NRs was allowed to grow for 5 min. The BBPA-functionalized CdSe was isolated by repeated dissolution in THF and precipitation in methanol for three times.

Synthesis of ethynyl-terminated P3HT. The ethynyl-terminated P3HT was synthesized by a quasi-living Grignard metathesis (GRIM) method,³⁰ Briefly, 2,5-dibromo-3-hexylthiophene (0.815g, 2.5 mmol) was dissolved in THF (5 mL) in a three-neck flask and stirred under Ar. Tert-butylmagnesium chloride (1.25 mL, 2.5 mmol) was added via syringe. The mixture was stirred for 2 h at room temperature. Subsequently, it was diluted to 25 mL with THF and Ni(dppp)Cl₂ (22.5 mg, 0.041 mmol) was added. The resulting mixture was first stirred for 10 min at room temperature, producing intermediate P3HT, followed by reacting with ethynylmagnesium bromide (2mL, 1mmol) in THF for

30 min at room temperature. The final product, ethynyl-terminated P3HT was obtained by precipitating the reaction mixture in methanol, filtering in an extraction thimble, and washing by Soxhlet extraction with methanol, hexanes, and chloroform sequentially. The final pure ethynyl-terminated P3HT was recovered after chloroform evaporated. The regioregularity of ethynyl-terminated P3HT was greater than 98%. The number average molecular weight and PDI of ethynyl-terminated P3HT were 5100 g/mol and 1.18, respectively.

Yield: 40.8%. ^1H NMR (300 MHz, CDCl_3 , d (ppm): 6.98 (s, 1H), 6.0 (m, 1H), 3.05 (s, 1H), 2.8 (t, $J=3$ Hz, 2H), 1.7 (m, 2H), 1.43 (m, 2H), 1.36 (m, 4H), and 0.92 (t, 3H).

Synthesis of P3HT–CdSe nanocomposites by click reaction. NaN_3 was added in the BBPA-CdSe NR THF solution. The mixture was sealed and stirred at room temperature for three days. Excess amount of NaN_3 was removed by centrifugation. The resulting azide-benzylphosphonic acid capped CdSe NRs (i.e., $\text{N}_3\text{-BPA-CdSe}$) were then precipitated with methanol. Subsequently, 50 mg $\text{N}_3\text{-BPA-CdSe}$ NRs, 50mg ethynyl-terminated P3HT and 10 ml THF were loaded in a flask and kept at 60 °C under Ar for two days. Same as the case for nanocomposites prepared by Heck coupling, the reaction mixture was cooled, transferred, and centrifuged. The free P3HT molecules in the solution were removed by precipitation.

Characterization. The morphologies of CdSe NRs and nanocomposites were imaged by TEM (JEOL 1200EX scanning/transmission electron microscope (STEM); operated at 80 kV). The absorption spectra were recorded with a UV-Vis spectrometer (UV-1600, SHIMADAZU). The emission spectra were taken with a Nikon Eclipse TE2000-E microscope coupled with an optical insights hyperspectral unit and a Cascade 512B

camera (Roger Scientific). The ^1H NMR and ^{31}P NMR were performed using Varian VXR-400 spectroscopy. The grafting density of P3HT chains on the CdSe surface was determined by thermogravimetry analysis (TGA; TA Instrument TGA Q 50). The fluorescence lifetime measurements were performed using time-correlated single photon counting (TCSPC) technique. The full width at half-maximum (FWHM) of the instrument response function was $\sim 40\text{--}45$ ps. All samples were excited at $\lambda_{\text{ex}} = 407$ nm, and the fluorescence emission was collected at $\lambda_{\text{ex}} \geq 500$ nm at perpendicular polarization orientation of the emission polarizer with respect to the vertical excitation polarization in order to eliminate possible interferences of scattered excitation light from solid surfaces.

BBPA ligand recovery for NMR analysis. To recover the capping ligand of CdSe NRs for NMR analysis, the NR solution was precipitated for three times by adding methanol. The precipitate was isolated by centrifugation and decantation, and dried under vacuum at 80°C overnight. The NR powder was then dissolved in aqua regia (concentrated HNO_3 : concentrated $\text{HCl} = 1 : 3$). The resulting solution was extracted with ethyl ether. After ethyl ether evaporated under vacuum, the white solid was characterized by ^{31}P NMR in dimethyl sulfoxide- d_6 .

P3HT dissociation from nanocomposites for NMR analysis. The grafted P3HT cannot be stripped from the CdSe NR surface using the recovery method for BBPA because of the degradation of P3HT caused by aqua regia.^[1] Despite the fact that pyridine is a weak ligand, grafted P3HT can still be partially exchanged in a thermodynamically controlled process.^[2] Briefly, the purified P3HT–CdSe NR nanocomposites were first dissolved in pyridine. The mixture was then heated at 80°C and intensely stirred for three days under Ar in a 25 ml three-neck flask connected to a Liebig condenser. Excess pyridine was then

vacuumed at 80°C overnight, and the resulting solid was characterized by ¹H NMR in chloroform-d.

References:

- (1) Schwartz, B. J. *Annu. Rev. Phys. Chem.* **2003**, *54*, 141.
- (2) He, M.; Zhao, L.; Wang, J.; Han, W.; Yang, Y. L.; Qiu, F.; Lin, Z. Q. *ACS Nano* **2010**, *4*, 3241
- (3) Peng, X. G.; Manna, L.; Yang, W. D.; Wickham, J.; Scher, E.; Kadavanich, A.; Alivisatos, A. P. *Nature* **2000**, *404*, 59.
- (4) Goodman, M. D.; Xu, J.; Wang, J.; Lin, Z. Q. *Chem. Mater.* **2009**, *21*, 934
- (5) Gur, I.; Fromer, N. A.; Geier, M. L.; Alivisatos, A. P. *Science* **2005**, *310*, 462.
- (6) Coe, S.; Woo, W. K.; Bawendi, M.; Bulovis, V. *Nature* **2002**, *420*, 800.
- (7) Medintz, I. L.; Uyeda, H. T.; Goldman, E. R.; Mattoussi, H. *Nature Mater.* **2005**, *4*, 435.
- (8) Lin, Z. Q. *Chem. Eur. J.* **2008**, *14*, 6294.
- (9) Huynh, W. U.; Dittmer, J. J.; Alivisatos, A. P. *Science* **2002**, *295*, 2425.
- (10) Greenham, N. C.; Peng, X. G.; Alivisatos, A. P. *Phys. Rev. B.* **1996**, *54*, 17628.
- (11) Skaff, H.; Sill, K.; Emrick, T. *J. Am. Chem. Soc.* **2004**, *126*, 11322.
- (12) Xu, J.; Wang, J.; Mitchell, M.; Mukherjee, P.; Jeffries-EL, M.; Petrich, J. W.; Lin, Z. Q. *J. Am. Chem. Soc.* **2007**, *129*, 12828.
- (13) Kang, Y. M.; Park, N. G.; Kim, D. W. *Appl. Phys. Lett.* **2005**, *86*, 113101.
- (14) Zhang, Q. L.; Russell, T. P.; Emrick, T. *Chem. Mater.* **2007**, *19*, 3712.

- (15) Bock, V. D.; Hiemstra, H.; van Maarseveen, J. H. *Eur. J. Org. Chem.* **2005**, 51.
- (16) Moses, J. E.; Moorhouse, A. D. *Chem. Soc. Rev.* **2007**, 36, 1249.
- (17) Liu, H. T.; Owen, J. S.; Alivisatos, A. P. *J. Am. Chem. Soc.* **2007**, 129, 305.
- (18) Peng, Z. A.; Peng, X. G. *J. Am. Chem. Soc.* **2002**, 124, 3343.
- (19) Wang, W.; Banerjee, S.; Jia, S. G.; Steigerwald, M. L.; Herman, I. P. *Chem. Mater.* **2007**, 19, 2573.
- (20) Peng, Z. A.; Peng, X. G. *J. Am. Chem. Soc.* **2001**, 123, 1389.
- (21) Carbone, L.; Kudera, S.; Carlino, E.; Parak, W. J.; Giannini, C.; Cingolani, R.; Manna, L. *J. Am. Chem. Soc.* **2006**, 128, 748.
- (22) Boisselier, E.; Salmon, L.; Ruiz, J.; Astruc, D. *Chem. Commun.* **2008**, 5788.
- (23) Li, H. M.; Cheng, F. O.; Duft, A. M.; Adronov, A. *J. Am. Chem. Soc.* **2005**, 127, 14518.
- (24) Binder, W. H.; Sachsenhofer, R.; Straif, C. J.; Zirbs, R. *J. Mater. Chem.* **2007**, 17, 2125.
- (25) Pan, B. F.; Cui, D. X.; Xu, P.; Li, Q.; Huang, T.; He, R.; Gao, F. *Colloids Surf., A* **2007**, 295, 217.
- (26) Recher, P.; Sukhorukov, E. V.; Loss, D. *Phys. Rev. B* **2001**, 63.
- (27) Nazzal, A. Y.; Qu, L. H.; Peng, X. G.; Xiao, M. *Nano Lett.* **2003**, 3, 819.
- (28) Perepichka, I. F.; Perepichka, D. F.; Meng, H.; Wudl, F. *Adv. Mater.* **2005**, 17, 2281.
- (29) Collini, E.; Scholes, G. D. *Science* **2009**, 323, 369.

- (30) Iovu, M. C.; Craley, C. R.; Jeffries-EL, M.; Krankowski, A. B.; Zhang, R.; Kowalewski, T.; McCullough, R. D. *Macromolecules* **2007**, *40*, 4733.

Chapter 3. Anisotropic Organic–Inorganic Nanocomposites by Placing Conjugated Polymers in Intimate Contact with Quantum Rods

3.1 Introduction

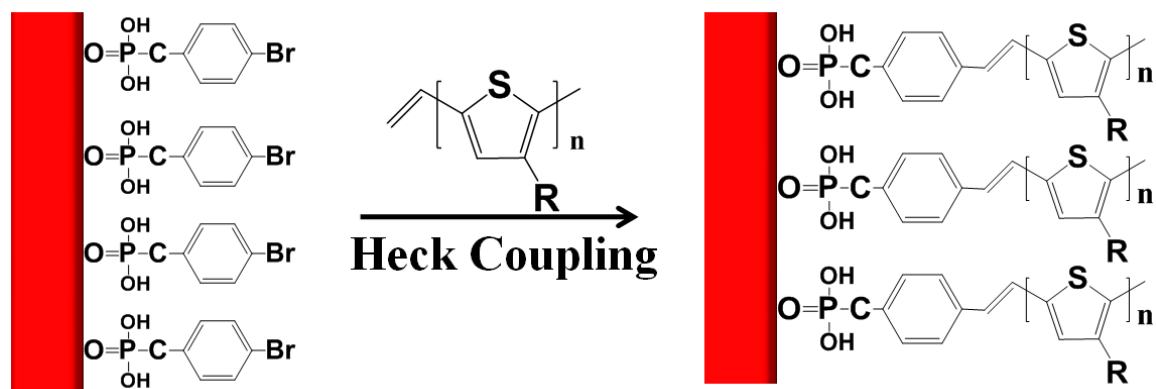
Recent advances in synthesis¹ and assembly² of nanocrystals (NCs) provide unique opportunities to exploit NCs for the development of next generation organic/inorganic hybrid solar cells as one of the most promising alternatives to Si solar cells to deliver efficient energy conversion with inexpensive fabrication.^{3,4} These conjugated polymer-based photovoltaic devices capitalize on the advantages peculiar to conjugated polymers (CPs), such as light weight, flexibility, processability, roll-to-roll production, low cost, and large area, in conjunction with the high electron mobility and tunable optical properties of inorganic NCs. In the organic/inorganic hybrids, poly(3-hexylthiophene) (P3HT) is one of the most extensively utilized CPs due to its excellent solution processability, environmental stability, high charge carrier mobility, and tailorable electrochemical properties;^{5,6} and CdSe quantum dots (QDs) are the commonly investigated NCs because of their quantum-confined nature and well-matched energy level with P3HT.⁷⁻¹³

However, the CP/NC hybrids are widely prepared by simply *physically mixing* CP and NC. As such, it remains challenging to control the detailed morphology and dispersion of NCs within CPs at the nanoscale. The NCs are often passivated with insulating organic ligand that hinders the efficient electronic interaction (e.g., charge transfer) with the surrounding CPs.¹⁴ Moreover, due to the large difference in their solubilities, phase separation of CPs and NCs was inevitable, thereby reducing the

interfacial area between them and limiting the performance of the resulting devices.¹⁵ To this end, the ability to chemically tether NCs with CPs (i.e., preparing CP–NC nanocomposites with well-controlled interfaces) provides a means of achieving a uniform dispersion of NCs and, most importantly, significantly promoting the electronic interaction between the electron-donating CPs and electron-accepting NCs.^{16,17} Notably, this strategy has only recently been developed and primarily implemented via ligand exchange that suffers from incomplete surface coverage.^{16,18}

The ability to manipulate the shape of semiconductor NCs has led to quantum rods (QRs) with diameters ranging from 2 to 10 nm and lengths ranging from 5 to 100 nm.^{19,20} QRs possess improved optical absorption in the visible and near-infrared ranges⁷ and enhanced electron mobility when being aligned in the direction of transport, an advantage over QDs where electron hopping between QDs is required, which make them better NCs than QDs for use in solar cells.²¹ *Herein, we discussed a simple yet robust route to directly placing conjugated polymer, P3HT in intimate contact with anisotropic CdSe QRs (i.e., creating P3HT–CdSe QR nanocomposites), dispensing with the need for ligand exchange chemistry.* The bromobenzylphosphonic acid (BBPA) was utilized as a novel bifunctional ligand with the phosphonic acid and aryl bromide at each end. The phosphonic acid group coordinated with CdSe to induce elongated growth, yielding BBPA-functionalized CdSe QRs (i.e., BBPA–CdSe QRs) with the aryl bromide group on their surface. Subsequently, P3HT–CdSe QR nanocomposites were obtained by Heck coupling of vinyl-terminated P3HT with BBPA–CdSe QRs (i.e., coupling reaction between the vinyl endgroup of P3HT with the aryl bromide of BBPA–CdSe). The success of direct coupling was confirmed by nuclear magnetic resonance spectroscopy (NMR)

and dynamic light scattering. The occurrence of charge transfer at the P3HT/CdSe interface was evidenced by UV-Vis absorption, photoluminescence (PL), and time-resolved PL studies. As such, it stands out as a promising method to simplify the synthesis procedure and opens opportunities to increase the grafting density for large-scale synthesis for use in solar cells.



Scheme 3-1. Direct grafting vinyl-terminated P3HT onto bromobenzylphosphonic acid-functionalized CdSe QRs (i.e., BBPA-CdSe QRs) by Heck coupling, yielding P3HT-CdSe QR nanocomposites.

3.2 Result and Discussion

Bromobenzylphosphonic acid (BBPA; bearing aryl bromide end group) functionalized CdSe QRs (i.e., BBPA-CdSe QRs) were synthesized based on a ligand-exchange free procedure (**Scheme 3-1**; also see *Experimental*). Notably, phosphonic acids are most widely utilized ligands to induce the anisotropic growth of NCs as they coordinate more strongly on the NC surface than other ligands, thereby effectively regulating the growth rate of NCs and raising the energy of (001) faces of CdSe wurtzite structure. Moreover, recent NMR study showed that phosphonic acid was the only

capping ligand on the elongated CdSe nanostructures, even though excess amount of phosphate oxide was used as the solvent.²² The TEM measurements revealed high quality one-dimensional CdSe QR morphology with wurtzite structure with 40 ± 6 nm in length and 5 ± 1 nm in diameter (**Figure 3-1**). The local weak aggregation was due to the self-assembly of BBPA-CdSe QRs on the TEM grid after solvent evaporation.^{1,23} The QRs possessed monodispersed size distribution as evidenced by the dynamic light scattering (DLS) measurement in which a relatively narrow single peak was observed (**Figure 3-2a**). The BBPA was a bifunctional ligand, in which the aryl bromide on one end can readily react with vinyl-terminated P3HT via Heck coupling and the phosphonic acid group on the other end promoted the strong anchoring of BBPA to the CdSe QR surface.

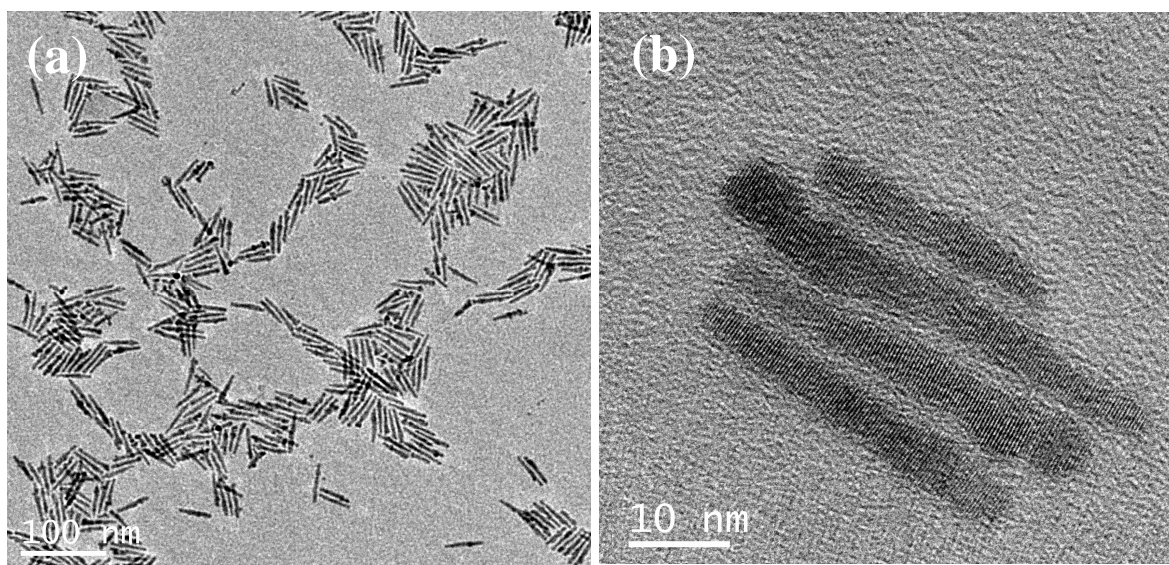


Figure 3-1. TEM images of (a) BBPA-functionalized CdSe QRs (i.e., BBPA-CdSe QRs) prepared using the ODP:BBPA mixture at the 5:1 molar ratio, and (b) close-up of individual BBPA-CdSe QRs in which the crystalline lattice is clearly evident.

The ^{31}P NMR of BBPA-CdSe QRs clearly showed the existence of BBPA. No signal of TOPO used as the solvent (see *Experimental*) was observed due to the much weaker capping ability of TOPO than phosphonic acid; this is in good agreement with previously reported work.^{24,25} The addition of octadecyl phosphonic acid (ODPA; a 18 carbon chain) as a co-ligand was found to play an important role in producing high quality, well-dispersed elongated NCs. Growth of QRs with BBPA solely led to the formation of highly aggregated elongated nanostructures (**Figure 3-3a**) due to poor stabilization of BBPA in relatively low polar organic solvent (i.e., THF and toluene used in the study), in which P3HT, however, was fully dissolved during the grafting process.²⁶ Moreover, the CdSe QRs synthesized with BBPA solely also suffered from low quality, and possessed branches, kinks, and non-uniform cross sections along the diameter of QRs (**Figure 3-3a**). Therefore, phosphonic acids with long alkyl chains (e.g., tetra decyl phosphonic acid (TDPA; an 18 carbon chain) or ODPA) were needed to stabilize the hydrophobic QRs in THF. We note that compared to ODPA or TDPA which are widely used ligands in the synthesis of CdSe QRs, BBPA had much shorter chain length, and thus much higher reactivity due to less steric hindrance during the monomer diffusion and crystal growth process.^{22,27} The QRs synthesized by BBPA are more susceptible to have certain defects,²⁸ including stacking faults and twinning defects, which lead to extensive branching.²⁵ As such, in order to reduce the overall growth rate, phosphonic acid with longer length was added. The presence of these ligands (ODPA or TDPA) acted as the monomer buffer in conjunction with BBPA, thereby effectively regulating the monomer concentration during the anisotropic growth of QRs.^{1,29}

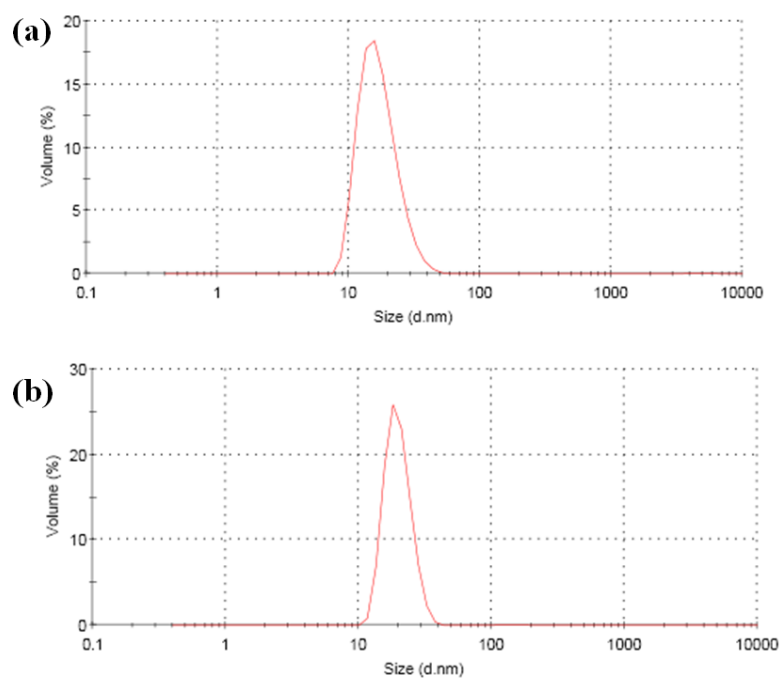


Figure 3-2. Dynamic light scattering (DLS) measurements on (a) BBPA-CdSe QRs, and (b) P3HT-CdSe QR nanocomposites prepared by Heck coupling.

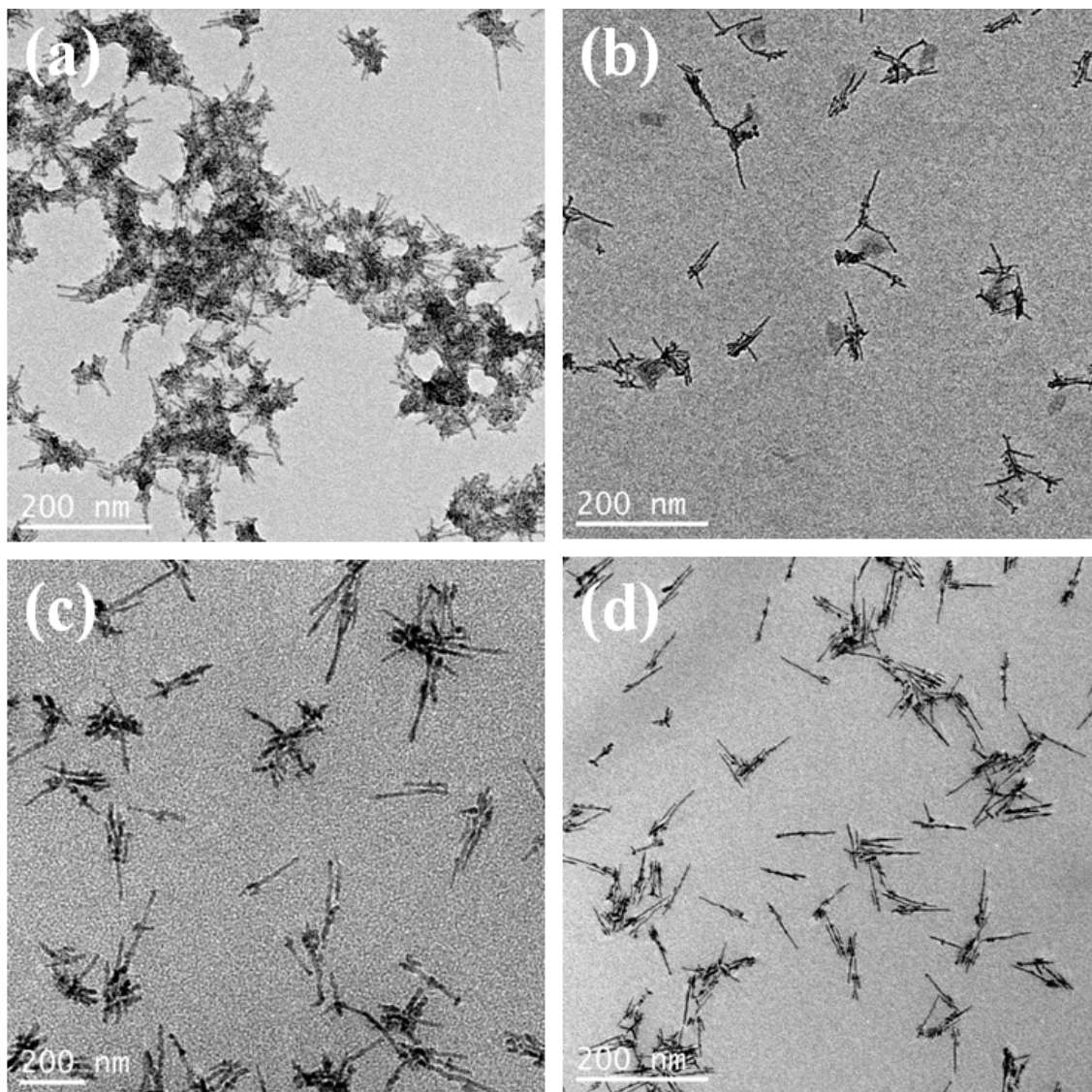


Figure 3-3. TEM images of CdSe QRs synthesized with (a) BBPA solely, (b) TDPA:BBPA mixture at 3:1 molar ratio, (c) TDPA:BBPA mixture at 5:1 molar ratio, and (d) ODPa:BBPA mixture at 3:1 molar ratio.

Both TDPA and ODPa were explored in order to improve the quality and dispersion of QRs. The ligand mixtures at different molar ratio (i.e., ODPa (or TDPA):BBPA = 3:1, and ODPa (or TDPA):BBPA = 5:1) were systematically investigated. The QR quality can be greatly improved with the increase of ODPa (or TDPA) ratio in the ligand mixture (**Figure 3-3**), with ODPa being more effective than

TDPA (i.e., ODPa:BBPA = 3:1 in **Figure 3-3d** and ODPa:BBPA = 5:1 in **Figure 3-1a**). The best quality of CdSe QRs was obtained at the ODPa:BBPA = 5:1 (**Figure 3-1a**), which was comparable to those reported using the HPA:TDPA ligand mixture.^{24,29} Compared to TDPA, ODPa had longer alkyl chain and thus lower reactivity, leading to more short and less branched structures.²⁵ The TEM observations suggested that larger activity difference in the ligand mixture (e.g., ODPa:BBPA) tended to yield better quality QRs by serving as the precursor concentration buffer and regulating the anisotropic growth of QRs.

It is noteworthy that similar amounts of BBPA and ODPa passivated the CdSe QR surface as revealed by ³¹P NMR regardless of the initial molar ratio of ODPa:BBPA = 5:1.³⁰ The higher coordination efficiency of short-chain molecules than long-chain counterparts has been widely observed in the synthesis of CdSe QRs. For example, hexylphosphonic acid (HPA) was found to be predominately covered at the QR surface when the ligand mixture of HPA:TDPA was utilized.^{24,25} This phenomenon can be explained by the change in free energy after the attachment of free molecules on solid surface. It was less energetic favorable for longer-chain ligand to coordinate with CdSe because of larger repulsive osmotic force experienced by long chains that were packed on the surface.³¹ As a result, due to its long alkyl chain, the ODPa ligand was much less competitive than BBPA for the QR surface functionalization, leading to CdSe QRs possessing high density of BBPA despite the initial molar ratio of ODPa:BBPA was 5:1. By contrast, TDPA (a shorter chain than ODPa) may be relatively comparable to BBPA for the QR surface passivation. As a result, the QR surface was primarily capped with TDPA due to the large initial molar ratio of TDPA:BBPA; and the extremely weak ³¹P

NMR signal of BBPA was detected from the CdSe QRs at the TDPA:BBPA = 5:1 (data not shown). Taken together, among various mixed ligands investigated, CdSe QRs synthesized with the ODPA:BBPA ratio of 5:1 possessed the best quality and BBPA grafting density, most suitable for grafting vinyl-terminated P3HT (a “grafting-onto” approach;**Scheme3-1**).

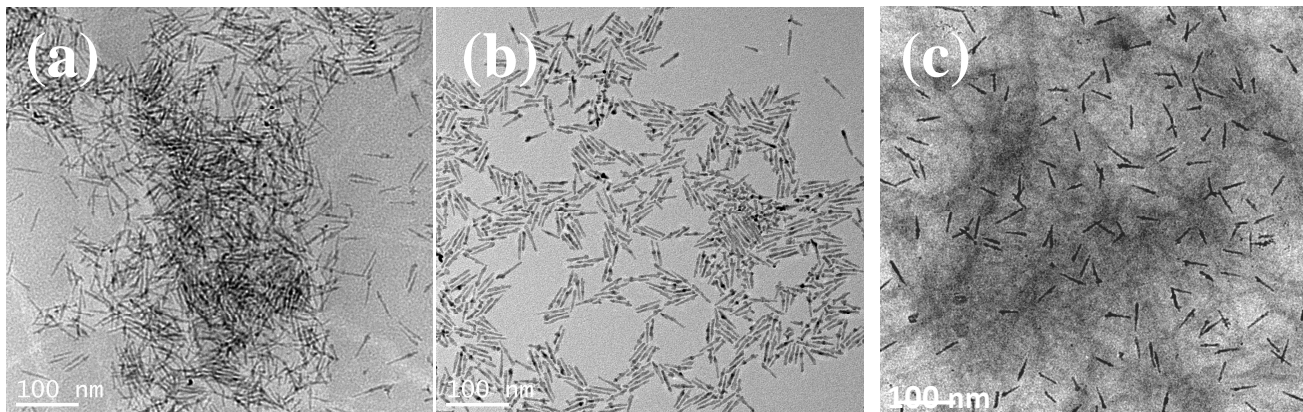


Figure 3-4. TEM images of (a) physical mixture of vinyl-terminated P3HT and BBPA-CdSe QRs, (b) P3HT–CdSe QR nanocomposites synthesized by Heck coupling, and (c) P3HT–CdSe QR nanocomposites in the P3HT homopolymer matrix.

We note that in our previous work, P3HT–CdSe QDs nanocomposites were synthesized by *directly* grafting vinyl-terminated P3HT onto [(4-bromophenyl)methyl]dioctylphosphine oxide (DOPO-Br) functionalized CdSe QD surface.²⁶ The strategy of capitalizing on the DOPO-Br ligand to produce DOPO-Br-functionalized CdSe QDs to render the chemical tethering of vinyl-terminated P3HT, however, cannot be extended to the CdSe QR synthesis. This is because phosphate oxide, the capping group in DOPO-Br, was not a suitable ligand to induce elongated growth of CdSe NCs.¹ The growth in phosphate oxide occurred too rapidly at the high monomer concentration desired for the elongated growth, thereby resulting in primarily isotropic

dot-like NCs.¹ Thus, prior to the coupling with vinyl-terminated P3HT, the ligand exchange was utilized to functionalize QR with DOPO-Br.³² However, the ligand exchange process is often plagued by incomplete surface coverage.¹⁶

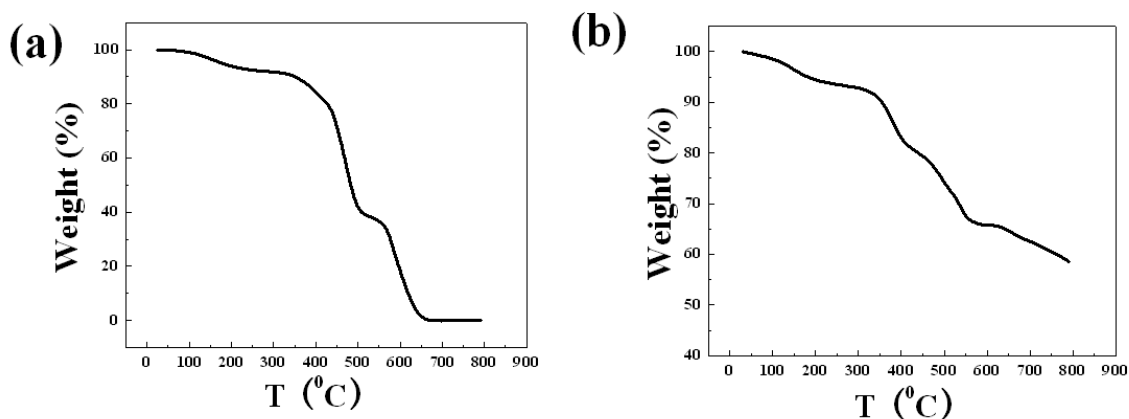


Figure 3-5. Thermogravimetry analysis (TGA) of (a) vinyl-terminated P3HT, (b) P3HT-CdSe QR nanocomposites prepared by Heck coupling.

In this context, as illustrated in **Scheme 3-1**, vinyl-terminated P3HT was grafted onto BBPA functionalized CdSe QRs via a mild palladium-catalyzed Heck coupling of aryl bromide of BBPA with vinyl group of P3HT, yielding P3HT-CdSe QR nanocomposites in the absence of ligand exchange chemistry. The color of the solution changed from brown (CdSe) to light purple (P3HT) after the reaction and subsequent purification, indicating P3HT was grafted onto CdSe QRs. TEM images of P3HT/CdSe QR composites prepared by physically blending vinyl-terminated P3HT and BBPA-CdSe, and P3HT-CdSe QR nanocomposites are shown in **Figure 3-4a** and **3-4b**, respectively. Compared to the physical mixture counterpart that showed significant phase segregation (**Figure 3-4a**) and thus reduced the interfacial area needed for charge separation, CdSe QRs were well dispersed within the P3HT-CdSe QR nanocomposites

as evidenced in **Figure 3-4b**. The self-assembly of nanocomposites was clearly evident, which can be attributed to strong dipole-dipole interaction of CdSe QRs typically observed in the elongated nanostructures (**Figure 3-4b**).^{33,34} The P3HT/CdSe weight ratio in composites (~1: 3.135) was made to be the same as that of nanocomposites; the ratio in the latter was determined by TGA measurements (**Figure 3-5**). Quite intriguingly, the P3HT–CdSe QR nanocomposites can also be readily dispersed in the P3HT homopolymer matrix (**Figure 3-4c**); this is in sharp contrast to phase segregation observed in the P3HT/CdSe composites (**Figure 3-4a**).¹⁵ It is interesting to note that no clear grafted P3HT at the periphery of CdSe QRs was imaged by TEM (**Figure 3-6**) due to low electron density of P3HT compared to inorganic QRs.²⁶ However, the existence of P3HT grafting can be indirectly verified by the DLS measurement, which had been proven to be an effective method to confirm the coating at the surface of QRs (e.g., Au).³⁵ After P3HT grafting, the average size of QRs actually increased from 17.37 nm to 20.03 nm (**Figure 3-4**).

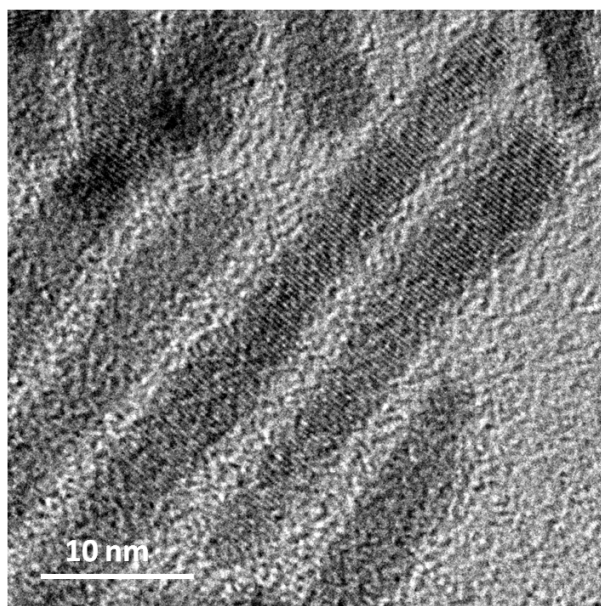


Figure 3-6. HRTEM image of P3HT–CdSe QR nanocomposites synthesized by Heck coupling.

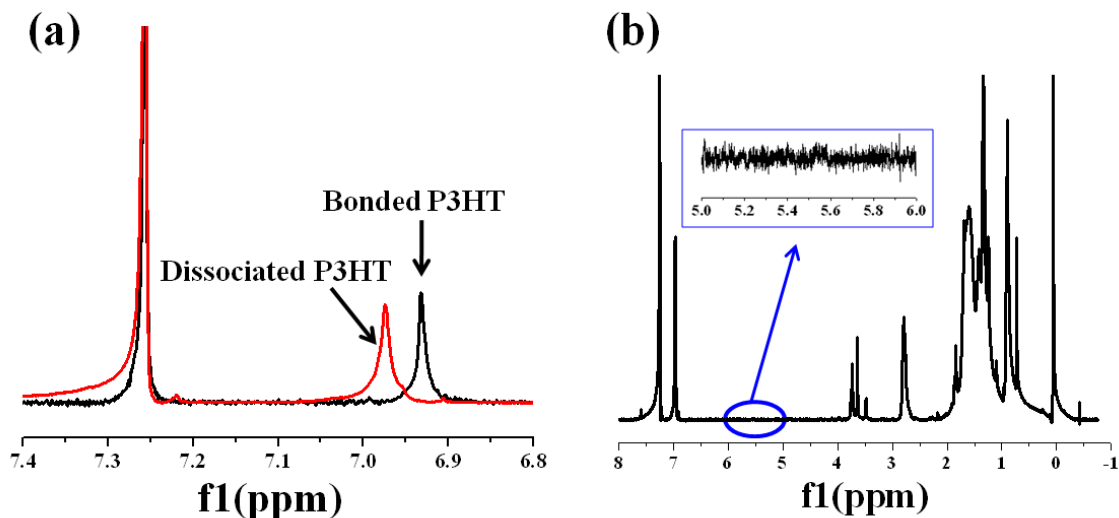


Figure 3-7. (a) ^1H NMR traces of P3HT bonded on the CdSe surface (black curve) and in the free state (red curve) in the chloroform. The signal from *d*-chloroform at 7.26 ppm was shown as reference. (b) ^1H NMR traces of P3HT stripped from P3HT–CdSe nanocomposites. Insert shows the close-up from 5 ppm to 6 ppm.

The success of coupling of vinyl-terminated P3HT with BBPA-CdSe QRs was confirmed by the solution ^1H -NMR. Compared with the molecules and QDs,³⁶ QRs are large in volume, the vibration of bonded P3HT was strongly confined under magnetic wave, resulting in low resolution NMR signal of the vinyl coupling group (i.e., double bond) nearby the QR surface.²⁵ Therefore, a dissociation procedure was employed to detach grafted P3HT chain from the QR surface, and thus P3HT coupled with BBPA ligand can be characterized in a free unbonded state (see *Experimental*). After Heck coupling, the proton signal from thiophene ring at 6.93ppm was observed,²⁶ and it was shifted to 6.97ppm after dissociation of P3HT, indicating that P3HT was originally

bonded to CdSe (**Figure 3-7a**).³⁰ Furthermore, two proton signals from vinyl end group on P3HT at 5.1 and 5.5 ppm disappeared after coupling with BBPA-CdSe QRs, suggesting P3HT was grafted onto CdSe QRs (**Figure 3-7b**).²⁶ The grafting density of P3HT chains was determined by thermogravimetry analysis (TGA) (**Figure 3-5**). The molecular weight of CdSe QRs was estimated to be 9.81×10^6 g/mol based on TEM images shown in **Figure 3-1**, and the P3HT/CdSe weight ratio was 1 : 3.135 from TGA. Thus the P3HT/CdSe molar ratio was approximately 600:1, much higher than that obtained from ligand exchange approach, which was 250:1.³²

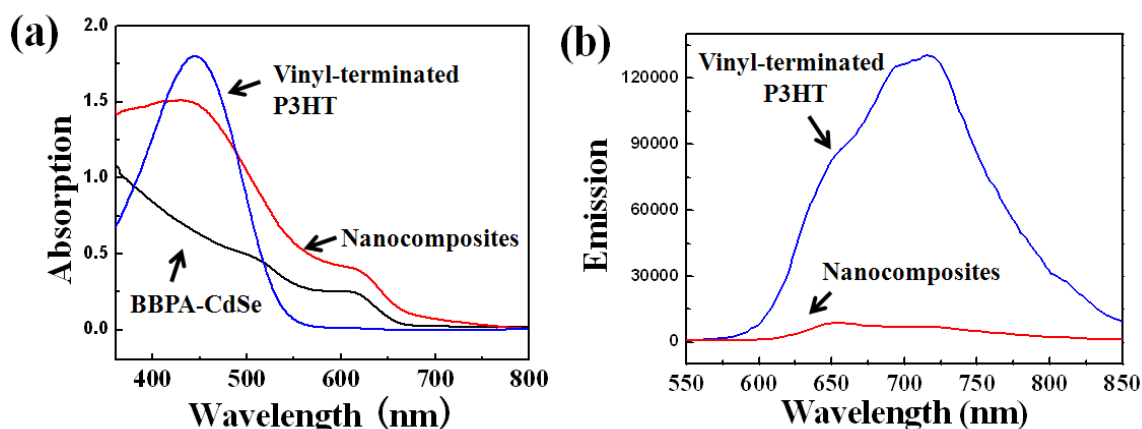


Figure 3-8. (a) Absorption spectra of the P3HT–CdSe nanocomposites prepared by Heck coupling (red curve), BBPA-CdSe QRs (black curve), and vinyl-terminated P3HT (blue curve); (b) Emission spectra of vinyl-terminated P3HT (blue curve) and the P3HT–CdSe nanocomposites (red curve) in dry state.

The photophysical properties of the resulting P3HT–CdSe QR nanocomposites were explored by absorption and solid state photoluminescence (PL) studies. **Figure 3-8a** shows the absorption spectra of BBPA-CdSe QR, vinyl-terminated P3HT, and P3HT–CdSe QR nanocomposites in THF. The absorption maxima for P3HT and CdSe QRs were at 448nm and 614nm, respectively. It is clear that the absorption spectrum of

nanocomposites was simply the sum of the absorption spectra of its constituents, which served as additional evidence of successful coupling of nanocomposites. The dry nanocomposite film was characterized by PL measurement, which was acquired from the sample sealed in an Ar-filled vial to prevent possible photodegradation (**Figure 3-8b**).³⁷ The vibronic structures of vinyl-terminated P3HT were clearly evident.²⁶ By contrast, a nearly complete quenching of P3HT fluorescence was seen, implying efficient charge transfer from P3HT to CdSe QRs. This observation further confirmed intimate chemical contact between P3HT and CdSe.³²

In order to provide additional information on the charge transfer dynamics in P3HT–CdSe nanocomposites, time-resolved PL measurements (i.e., ultrafast emission dynamics) monitored at the wavelength above 550 nm were performed by measuring the fluorescence lifetime using time-correlated single-photon counting (TCSPC) methodology.²⁶ The solid state dynamics took place on the picosecond time scale and involved the diffusion of electronic excitations from P3HT to CdSe.^{26,38} The measurements revealed that P3HT/CdSe composites (i.e., mixture of P3HT and BBPA-CdSe) had a fluorescence lifetime of 320 ps, close to a 375 ps lifetime for P3HT homopolymer;³⁰ this is because the charge transfer between P3HT and CdSe was hindered by the insulating ligands (i.e., BBPA and ODPA) as well as the strong phase segregation in composites (**Figure 3-4a**).²⁶ The P3HT–CdSe nanocomposites formed by Heck coupling, however, exhibited a much faster lifetime of 170 ps, an important signature of an improved interfacial contact between P3HT and CdSe. The direct chemical anchoring of P3HT on CdSe made it easy for excitons to find the interface and dissociate, representing as a rapid charge transfer from P3HT to CdSe.^{7,26} This result was

well correlated with the static PL study (**Figure 3-8b**). The charge transfer led to the PL quenching since the photogenerated exciton was dissociated before luminescence occurred.

3.3 Conclusion:

In summary, a simple yet robust “grafting-onto” strategy was exploited to successfully produce semiconductor organic–inorganic nanocomposite by anchoring end-functional CPs (i.e., vinyl-terminated P3HT) onto anisotropic NCs that possessed complimentary functional group (i.e., BBPA-CdSe QRs) via a mild palladium-catalyzed Heck coupling, thereby affording direct contact between P3HT and CdSe QRs and dispensing with the need for ligand exchange chemistry as in copious previous work. The success grafting was confirmed by NMR and DLS measurements. The CdSe QRs were well dispersed within the resulting P3HT–CdSe QR nanocomposites, and the nanocomposites can also be well distributed in the P3HT homopolymer matrix. The grafting density of P3HT was greatly increased as compared to that using conventional ligand exchange approach. The solid-state emission spectra of nanocomposites suggested the charge transfer from P3HT to CdSe. While the CdSe QRs were studied here, this synthetic strategy is not restricted to them but can be easily extended to other various elongated nanostructures (e.g., nanowire, tetrapods, etc.) as well as other types of semiconductors (e.g., CdS, CdTe, PbS, PbSe, etc.). Such nanocomposites, in which CPs and anisotropic NCs are intimately contacted, may be very promising for use in organic–inorganic hybrid solar cells with improved power conversion efficiency due to

(i) an increased interfacial contact these two constituents, and (ii) continuous pathways provided by the long axis of anisotropic NCs.

3.4 Experimental Section

All chemicals, including 4-Bromobenzyl bromide, triethyl phosphate, cadmium oxide (CdO), tri-n-octylphosphine oxide (TOPO), N-methyldicyclohexylamine, 2,5-dibromo-3-hexylthiophene, Ni(dppp)Cl₂, tert-Butylmagnesium chloride (2mol/L in diethyl ether), vinylmagnesium bromide (0.5 mol/L in THF) purchased from Sigma Aldrich, tetra decyl phosphonic acid (TDPA), and octadecyl phosphonic acid (ODPA) purchased from PCI synthesis were used as received. THF (Fisher, 99%) was refluxed over sodium wire and distilled from sodium naphthalenide solution.

Synthesis of bromobenzylphosphonic acid (BBPA): The bromobenzylphosphonic acid (BBPA) was synthesized by modifying a reported procedure.³⁹ In general, mixture of 4-Bromobenzyl bromide and triethyl phosphate (molar ratio = 1:2) was heated and stirred under Ar at 150 °C for 5 h to yield diethylphosphonate ester. The excess triethyl phosphate and byproducts were then removed by heating at 100 °C under vacuum for several hours. After that, diethylphosphonate ester was hydrolyzed to yield BBPA by adding excess concentrated aqueous HCl and heated at 100°C overnight. After cooling down to room temperature, the BBPA was filtered out, and then redissolved in CH₃CN. The addition of CH₃CN and its evaporation using rotary evaporator were repeated for

three times to remove trace amount of water and HCl. Finally BBPA was recrystallized using ethyl acetate to obtain pure product.

Yield: 56%. ^1H NMR: 7.46 and 7.19 (AA'XX', 4H), 2.94 (d, 2H, $J=21$ Hz)

Synthesis of BBPA capped CdSe QRs: A mixture of 67 mg BBPA, 333 mg ODPa, 1.5g TOPO, and 0.1 g CdO was first degassed in a 25 ml three-neck flask connected to a Liebig condenser at room temperature in vacuum and subsequently at 120°C for 60 min. It was then slowly heated under Ar until CdO decomposed and the solution turned clear and colorless. Next, 0.7 ml TOP was added, and the temperature was further raised to 320 °C. 36 mg selenium dissolved in 0.5 ml TOP was rapidly injected to the vigorously stirred Cd precursor. The CdSe QRs was allowed to grow for 5 min. The heating mantle was then removed to stop the reaction. After the solution was cooled to 60 °C, 2 ml THF was added to the flask. The BBPA-functionalized CdSe was isolated by repeated dissolution in THF and precipitation in methanol for three times.

Synthesis of vinyl-terminated P3HT: Vinyl-terminated P3HT was synthesized by a quasi-living Grignard metathesis (**GRIM**) **method**.⁴⁰ Briefly, 2,5-dibromo-3-hexylthiophene (0.815g, 2.5 mmol) was dissolved in THF (5 mL) in a three-neck flask and stirred under Ar. Tert-butyilmagnesium chloride (1.25 mL, 2.5 mmol) was added via syringe. The mixture was stirred for 2 h at room temperature. Subsequently, it was diluted to 25 mL with THF and Ni(dppp)Cl₂ (22.5 mg, 0.041 mmol) was added. The resulting mixture was first stirred for 10 min at room temperature, producing intermediate P3HT, followed by reacting with vinylmagnesium bromide (2mL, 1mmol) in THF for 30

min. The product vinyl-terminated P3HT was obtained by precipitating the reaction mixture in methanol, filtering in an extraction thimble, and washing by Soxhlet extraction with methanol, hexanes, and chloroform sequentially. The final pure vinyl-terminated P3HT was recovered after chloroform evaporated. The regioregularity of P3HT was greater than 98% as determined by ^1H -NMR. The number average molecular weight and polydispersity index (PDI) of P3HT were 4900 g/mol and 1.2, respectively, as measured by GPC.

Yield: 46.6%. ^1H NMR (300 MHz, CDCl_3 , d (ppm): 6.98 (s, 1H), 6.0 (m, 1H), 5.19 (dd, $J = 8$ Hz and 3 Hz, 1H), 5.10 (dd, $J = 8$ Hz and 3 Hz, 1H), 2.8 (t, $J = 3$ Hz, 2H), 1.7 (m, 2H), 1.43 (m, 2H), 1.36 (m, 4H), and 0.92 (t, 3H).

Synthesis of P3HT–CdSe nanocomposites by Heck coupling: In the glove box 1 mg $\text{Pd}_2(\text{dba})_3$, 10 mg vinyl-terminated P3HT, and 10 mg BBPA functionalized CdSe QRs (i.e., BBPA–CdSe) were loaded in a reaction vial. 0.08 mL N-methyldicyclohexylamine, 0.06 mL tri-*t*-butylphosphine THF solution at a concentration of 100 mg/mL, and 0.5 mL THF were added sequentially. The reaction mixture was kept stirring under Ar in a 50 °C oil bath for 20 h. The final product, P3HT–CdSe nanocomposites was cooled to room temperature, transferred to new vial, and centrifuged at 2000 rpm for 0.5 h to remove catalyst. The supernatant (i.e., P3HT–CdSe nanocomposites) was diluted 10 times with THF and precipitated with methanol twice to remove free P3HT chains that were coupled with CdSe.

P3HT dissociation from nanocomposites for NMR analysis: The grafted P3HT cannot be stripped from the CdSe QR surface using the recovery method for BBPA because of the degradation of P3HT caused by aqua regia.⁴¹ Despite the fact that pyridine is a weak ligand, grafted P3HT can still be partially exchanged in a thermodynamically controlled process.⁴² Briefly, the purified P3HT–CdSe QR nanocomposites were first dissolved in pyridine. The mixture was then heated at 80°C and intensely stirred for three days under Ar in a 25 ml three-neck flask connected to a Liebig condenser. Excess pyridine was then vacuumed at 80°C overnight, and the resulting solid was characterized by ¹H NMR in chloroform–d.

BBPA ligand recovery for NMR analysis: To recover the capping ligand of CdSe QRs for NMR analysis, the QR solution was precipitated for three times by adding methanol. The precipitate was isolated by centrifugation and decantation, and dried under vacuum at 80 °C overnight. The QR powder was then dissolved in aqua regia (concentrated HNO₃ : concentrated HCl = 1 : 3). The resulting solution was extracted with ethyl ether. After ethyl ether evaporated under vacuum, the white solid was characterized by ³¹P NMR in dimethyl sulfoxide–d.

Characterizations: The morphology of CdSe QRs and nanocomposites were imaged by TEM (JEOL 1200EX scanning/transmission electron microscope (STEM); operated at 80 kV). The absorption spectra were recorded with a UV-Vis spectrometer (UV-1600, SHIMADAZU). The emission spectra were taken with a Nikon Eclipse TE2000-E microscope coupled with an optical insights hyperspectral unit and a Cascade 512B

camera (Roger Scientific). The ^1H NMR and ^{31}P NMR were performed using Varian VXR-400 spectroscopy. The grafting density of P3HT chains on the CdSe surface was determined by thermogravimetry analysis (TGA; TA Instrument TGA Q 50). The fluorescence lifetime measurements were performed using time-correlated single photon counting (TCSPC) technique. The apparatus for TCSPC is described in details elsewhere.⁴³ The full width at half-maximum (FWHM) of the instrument response function was $\sim 40\text{-}45$ ps. All samples were excited at $\lambda_{\text{ex}} = 407$ nm, and the fluorescence emission was collected at $\lambda_{\text{ex}} \geq 500$ nm at perpendicular polarization orientation of the emission polarizer with respect to the vertical excitation polarization in order to eliminate possible interferences of scattered excitation light from solid surfaces.

References:

- (1) Peng, X. G.; Manna, L.; Yang, W. D.; Wickham, J.; Scher, E.; Kadavanich, A.; Alivisatos, A. P. *Nature* **2000**, *404*, 59.
- (2) Tang, Z. Y.; Zhang, Z. L.; Wang, Y.; Glotzer, S. C.; Kotov, N. A. *Science* **2006**, *314*, 274.
- (3) Coakley, K. M.; McGehee, M. D. *Chem. Mater.* **2004**, *16*, 4533.
- (4) Huynh, W. U.; Dittmer, J. J.; Alivisatos, A. P. *Science* **2002**, *295*, 2425.
- (5) Byun, M.; Laskowski, R. L.; He, M.; Qiu, F.; Jeffries-EL, M.; Lin, Z. Q. *Soft Mater.* **2009**, *5*, 1583.
- (6) He, M.; Zhao, L.; Wang, J.; Han, W.; Yang, Y. L.; Qiu, F.; Lin, Z. Q. *ACS Nano* **2010**, *4*, 3241
- (7) Kang, Y. M.; Park, N. G.; Kim, D. W. *Appl. Phys. Lett.* **2005**, *86*, 113101.
- (8) Kharlampieva, E.; Kozlovskaya, V.; Zavgorodnya, O.; Lilly, G. D.; Kotov, N. A.; Tsukruk, V. V. *Soft Mater.* **2010**, *6*, 800.
- (9) Goodman, M.; Zhao, L.; DeRocher, K. A.; Wang, J.; Mallapragada, S. K.; Lin, Z. *ACS Nano* **2010**, *4*, 2043
- (10) Goodman, M. D.; Xu, J.; Wang, J.; Lin, Z. Q. *Chem. Mater.* **2009**, *21*, 934
- (11) Wang, J.; Xu, J.; Goodman, M. D.; Chen, Y.; Cai, M.; Shinar, J.; Lin, Z. Q. *J. Mater. Chem.* **2008**, *18*, 3270
- (12) Xu, J.; Xia, J.; Lin, Z. Q. *Angew. Chem., Int. Ed.* **2007**, *46*, 1860.

- (13) Xu, J.; Xia, J. F.; Wang, J.; Shinar, J.; Lin, Z. Q. *Appl. Phys. Lett.* **2006**, *89*, 133110.
- (14) Greenham, N. C.; Peng, X. G.; Alivisatos, A. P. *Phys. Rev. B.* **1996**, *54*, 17628.
- (15) Huynh, W. U.; Dittmer, J. J.; Libby, W. C.; Whiting, G. L.; Alivisatos, A. P. *Adv. Funct. Mater.* **2003**, *13*, 73.
- (16) Lin, Z. Q. *Chem. Eur. J.* **2008**, *14*, 6294.
- (17) Khanal, B. P.; Zubarev, E. R. *Angew. Chem. Int. Ed.* **2009**, *48*, 6888.
- (18) Genson, K. L.; Holzmüller, J.; Jiang, C. Y.; Xu, J.; Gibson, J. D.; Zubarev, E. R.; Tsukruk, V. V. *Langmuir* **2006**, *22*, 7011.
- (19) Fu, A.; Gu, W.; Boussert, B.; Koski, K.; Gerion, D.; Manna, L.; LeGros, M.; Larabell, C. A.; Alivisatos, A. P. *Nano Lett.* **2007**, *7*, 179.
- (20) Hu, J.; Li, L.; Yang, W.; Manna, L.; Wang, L.; Alivisatos, A. P. *Science* **2001**, *292*, 2060.
- (21) Zhang, Q. L.; Gupta, S.; Emrick, T.; Russell, T. P. *J. Am. Chem. Soc.* **2006**, *128*, 3898.
- (22) Peng, Z. A.; Peng, X. G. *J. Am. Chem. Soc.* **2002**, *124*, 3343.
- (23) Zimnitsky, D.; Xu, J.; Lin, Z. Q.; Tsukruk, V. V. *Nanotechnology* **2008**, *19*.
- (24) Peng, Z. A.; Peng, X. G. *J. Am. Chem. Soc.* **2001**, *123*, 1389.
- (25) Wang, W.; Banerjee, S.; Jia, S. G.; Steigerwald, M. L.; Herman, I. P. *Chem. Mater.* **2007**, *19*, 2573.

- (26) Xu, J.; Wang, J.; Mitchell, M.; Mukherjee, P.; Jeffries-EL, M.; Petrich, J. W.; Lin, Z. Q. *J. Am. Chem. Soc.* **2007**, *129*, 12828.
- (27) Liu, H. T.; Owen, J. S.; Alivisatos, A. P. *J. Am. Chem. Soc.* **2007**, *129*, 305.
- (28) Carbone, L.; Kudera, S.; Carlino, E.; Parak, W. J.; Giannini, C.; Cingolani, R.; Manna, L. *J. Am. Chem. Soc.* **2006**, *128*, 748.
- (29) Peng, Z. A.; Peng, X. G. *J. Am. Chem. Soc.* **2001**, *123*, 183.
- (30) Zhao, L.; Pang, X. C.; Adhikary, R.; Petrich, J.; and Lin, Z. Q. *Angew. Chem. Int. Ed.* **2011**, *In processing*.
- (31) Huang, J.; Kovalenko, M. V.; Talapin, D. V. *J. Am. Chem. Soc.* **2010**, *132*, 15866.
- (32) Zhang, Q. L.; Russell, T. P.; Emrick, T. *Chem. Mater.* **2007**, *19*, 3712.
- (33) Titov, A. V.; Kral, P. *Nano Lett.* **2008**, *8*, 3605.
- (34) Li, L. S.; Walda, J.; Manna, L.; Alivisatos, A. P. *Nano Lett.* **2002**, *2*, 557.
- (35) Pan, B. F.; Cui, D. X.; Xu, P.; Li, Q.; Huang, T.; He, R.; Gao, F. *Colloids Surf., A* **2007**, *295*, 217.
- (36) Genson, K. L.; Hoffman, J.; Teng, J.; Zubarev, E. R.; Vaknin, D.; Tsukruk, V. V. *Langmuir* **2004**, *20*, 9044.
- (37) Perepichka, I. F.; Perepichka, D. F.; Meng, H.; Wudl, F. *Adv. Mater.* **2005**, *17*, 2281.
- (38) van Herrikhuyzen, J.; George, S. J.; Vos, M. R. J.; Sommerdijk, N. A. J. M.; Ajayaghosh, A.; Meskers, S. C. J.; Schenning, A. P. H. J. *Angew. Chem. Int. Ed.* **2007**, *46*, 1825.

- (39) Pogorelova, S. P.; Kharitonov, A. B.; Willner, I.; Sukenik, C. N.; Pizem, H.; Bayer, T. *Anal. Chim. Acta* **2004**, *504*, 113.
- (40) Miyakoshi, R.; Yokoyama, A.; Yokozawa, T. *J. Am. Chem. Soc.* **2005**, *127*, 17542.
- (41) Briseno, A. L.; Holcombe, T. W.; Boukai, A. I.; Garnett, E. C.; Shelton, S. W.; Frechet, J. J. M.; Yang, P. D. *Nano Letters* **2010**, *10*, 334.
- (42) Querner, C.; Reiss, P.; Bleuse, J.; Pron, A. *J. Am. Chem. Soc.* **2004**, *126*, 11574.
- (43) Adhikary, R.; Carlson, P. J.; Kee, T. W.; Petrich, J. W. *J. Phys. Chem. B* **2010**, *114*, 2997.

Chapter 4. Self-Assembly of Ultrahigh Molecular Weight Comb Block Copolymer at the Air/Water Interface

4.1 Introduction:

Because of their broad range of potential applications in microlithography,¹ devices,² and biomimetic thin films,³ controlled patterning of amphiphilic copolymers at the air/water interface is attracting considerable attention. Upon deposition of amphiphilic copolymers on the water surface, the unfavorable interfacial interaction between the hydrophobic block and water leads to the aggregation of hydrophobic blocks, forming different morphologies to reduce the overall free energy of the system. On the other hand, the hydrophilic block tends to adsorb on the water surface, forming starfish-like structures for amphiphilic copolymers.⁴⁻⁶ To date, a variety of amphiphilic copolymers at the air/water interface, including linear block copolymers,^{1,4,5,7,8} star copolymers,⁹⁻¹³ and dendritic polymers,^{14,15 16} have been investigated, where a wide range of morphologies, for example dots,^{6,13,16,17} spaghetti,^{1,6,7,18} ribbons,^{15,16,19} islands,^{13,15,16} and continents,^{6,18} were observed. These surface features were heavily depended upon a number of parameters, including the polymer structure, surface pressure, and temperature,^{1,4,7,19} and have been extensively studied. However, due to the limited size and amorphous nature of these copolymers, it is often challenging to determine the microstructure of aggregates and their initial self assembly process at the zero surface pressure, which is critical for designing or predicting controllable patterns of newly synthesized polymers. Unlike the familiar self-assembly process of block copolymers in three dimension under the equilibrium condition, amphiphilic copolymers at the air/water interface are kinetically trapped in

their “frozen state” after the solvent removal,^{1,18} dictated by the chain entanglement between hydrophobic blocks in the spreading solution.^{1,17}

4.2 Experimental Section

Introduction of the ultrahigh molecular weight comb block copolymer

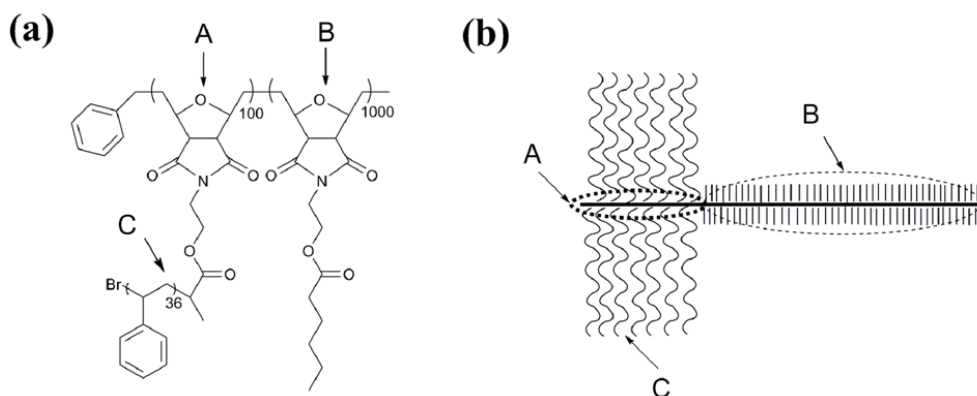


Figure 4-1. (a) Chemical structure and (b) schematic representation of the newly synthesized CBCP, which can be viewed as a triblock polymer. Each block is labeled as A (within a thick dotted circle), B (within a thin dotted circle), and C, respectively.

The chemical structure of CBCP is depicted in Figure 4-1a. It can be regarded as a triblock copolymer with one hydrophobic PS blocks as arm (i.e., C block) and two hydrophilic blocks in the backbone (i.e., short A block and long B block with very short alkyl side chains). It is an ultrahigh molecular weight, amphiphilic comb block copolymer (CBCP) with the domain size exceeding 100 nm.^{20,21} The block with the polystyrene arms assumed a rigid rod shape due to the steric crowding between the arms, resulting in elongation of the backbone polymer in that block (Figure 4-1b).²¹ The large molecular size and well-defined molecular structure make this CBCP an excellent candidate to study the microstructure of aggregates and their formation mechanism.

Fabrication and characterization of comb block copolymer LB monolayer

Previously synthesized CBCP with an ultrahigh molecular weight of 510 kg/mol was utilized in the present study.^{20,21} The dimension of the CBCP was estimated from molecular models by performing energy minimization using Material Studio 4.1. Chloroform (99.9%), toluene (99.8%), and carbon disulfide (99.8%) were purchased from Fisher Chemicals and used without further purification. The CBCP chloroform and toluene solutions at the concentration, $c = 6.29 \mu\text{M/L}$ were prepared. Surface pressure - area ($\pi - A$) isotherms and polymer monolayers were obtained with R&K Langmuir Blodgett (LB) system (Riegler & Kirstein, GmbH, 160 cm² Teflon trough). The trough was carefully cleaned with 1:1 H₂O₂:NH₃OH solution overnight and subsequently rinsed with DI water (NanoPure, > 18 M Ω cm) for 5 times. A 5 μL CBCP chloroform or toluene solution was gently placed on the water surface to ensure initial gas state.¹¹ After the solvent evaporated for 30 min, the monolayer film was compressed at a rate of 150 $\mu\text{m/sec}$.

Si substrate used for depositing LB films was cleaned with a mixture of sulfuric acid and Nonchromix, followed by rinsing with DI water and blown dry with N₂. For LB depositions, the Si substrate was withdrawn at a rate of 35 $\mu\text{m/sec}$ while keeping the pressure constant. Solvent vapor annealing was performed by placing the deposited film onto an elevated platform in a sealed container with approximate 10 mL of solvent in the reservoir.

Morphologies of LB films were examined by Atomic Force Microscopy (AFM; Dimension 3000) in the tapping mode. The scanning rate was 2 Hz. Each sample was imaged at more than 5 locations to ensure the reproducibility of features observed. The

average height and surface coverage of LB films were obtained by performing the bearing analysis.

4.3 Result and discussion

In this part, the self-assembly process of this newly synthesized CBCP was presented. The morphological changes influenced by the surface pressure, the assembly time, and the spreading solvent were systematically explored. The mechanism for surface pressure induced morphological changes was explored and further confirmed by the compression–expansion cycle and solvent annealing studies.

Effect of surface pressure

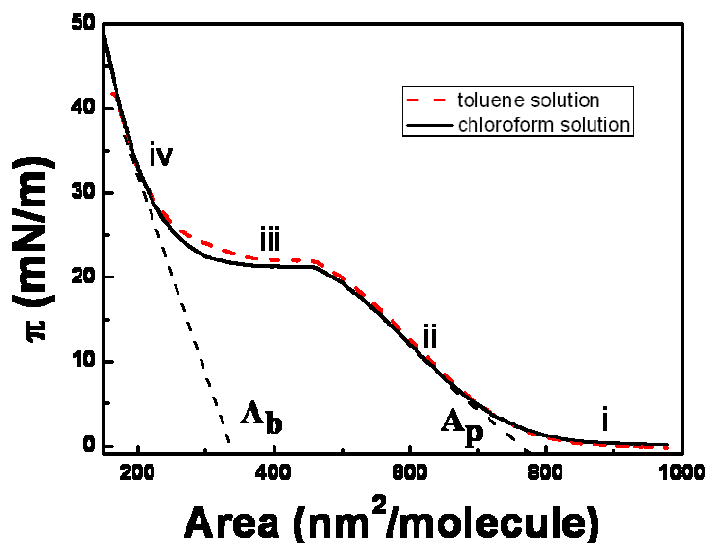


Figure 4-2. Pressure–area isotherms of the Langmuir monolayer of CBCP obtained from the chloroform solution (black solid line) and the toluene solution (red dash line), respectively. A_b and A_p are the area of brush-like structures and the area of pancake-like structures, respectively.

Langmuir isotherm, i.e., surface pressure – area ($\pi - A$) plot, of the CBCP is shown in

Figure 4-2. The continuous pressure rise was indicative of the formation of LB monolayer. The entire isotherm can be divided into four regions; they were (i) gas state at $\pi = 0$ mN/m, (ii) extended liquid state, (iii) plateau region at $\pi = 22$ mN/m, and (iv) condensed state. The similar isotherms were observed for both the chloroform solution and the toluene solution, suggesting that the solvent had no effect on the monolayer formation (Figure 4-2). Representative AFM height images of LB monolayers obtained at four regions are shown in Figure 4-3. Table 1 summarizes the height of self-assembled structures and the resulting surface coverage.

Table 4-1 Height and surface coverage of CBCP ribbons obtained from AFM images.

	Chloroform Solution						Toluene Solution	CS ₂ Annealing	Methanol Annealing	
	$\pi = 0$	$\pi = 10$	$\pi = 20$	$\pi = 22$	$\pi = 45$	$\pi = 0$	$\pi = 0$	$\pi = 20$	$\pi = 20$	$\pi = 20$
Pressure (mN/m)										
Time (hr)	0.5	0.5	0.5	0.5	0.8	2 h	2 h	2 h	2 h	7 h
Height, h (nm)	4.36	4.47	4.57	5.57	10.45	5.54	4.44	4.43	13.57	17.54
Surface Coverage (%)	24	30.7	31.5	55.1	43.3	30	21.4	40.5	54	93.1

Region (i) gas state ($\pi = 0$ mN/m): Ribbon-like structures with a broad size distribution were observed at the surface pressure $\pi = 0$ mN/m (Figure 4-3a). The height of ribbons was about 4.36 nm. These ribbons represented the aggregates of the raised PS chains (i.e., C block in Figure 1a) due to the hydrophobic characteristics of PS.^{17,19} Since the pressure has not yet been applied on the CBCP, the aggregation of PS blocks was a direct consequence of spontaneous self assembly of PS chains. The driving force for the self-assembly was an interplay of the attractive interaction between hydrophilic chains (i.e., B blocks) and the water phase, and the repulsive interactions between PS chains and water as well as between PS chain and hydrophilic chains as chloroform evaporated.^{6,22} With no

surface pressure applied, the self-assembled ribbons were highly dispersed as evidenced in Figure 4-3.

Region (ii) extended liquid state region ($\pi = 0\text{--}22$ mN/m): A typical AFM height image of LB film deposited at surface pressure $\pi = 10$ mN/m is shown in Figure 4-3 b. Compared with the sample obtained at $\pi = 0$ mN/m, the ribbon length dramatically increased. However, the average width and height of ribbons did not change within the error limit (Table 1; i.e., $h = 4.47$ nm at $\pi = 10$ mN/m vs. $h = 4.36$ nm at $\pi = 0$ mN/m). At $\pi = 10$ mN/m, the ribbons were still separated from each other, indicating that the hydrophilic chains (i.e., B blocks) formed the corona around the ribbons (i.e., aggregates of PS blocks) as schematically illustrated in Figure 4-6 a,¹⁷ and the elastic repulsive force between the hydrophilic corona distanced PS ribbons.¹⁹ The scratch tests showed no height difference between the inter-ribbon area, occupied by the hydrophilic corona and the Si substrate. Similar to other typical amphiphilic block copolymers,^{5,6} the CBCP exhibited a so called pancake-like structure with hydrophilic B blocks adsorbed on the water surface (Figure 4-6 a). The pancake surface area A_P was 795 nm^2 , determined by extrapolating the initial pressure rise from 0 mN/m to 22 mN/m (Figure 4-3); the large A_P was consistent with the ultrahigh molecular weight nature of CBCP.

Region (iii) plateau region ($\pi = 22$ mN/m): The plateau at surface pressure $\pi = 22$ mN/m can be attributed to a “pancake-to-brush” transition (i.e., a first order phase transition)⁷ as the hydrophilic B chains desorbed from the water surface and submerged into the water subphase upon further compression, forming a brush-like structure (Figure 4-6b).¹⁹ While the shape of PS ribbons was retained, the ribbons coalesced side by side shown in the inset of Figure 3c. This led to the increase in the height of ribbons,

yielding $h = 5.57$ nm (Table 1).

Region (iv) condensed state region ($\pi > 22$ mN/m): Continuing compression of the CBCP led it to the condensed state. The hydrophilic B blocks completely submerged into the water subphase and the hydrophilic PS chains remained on the water surface. The incompressible PS chains further overlapped and the surface pressure increased dramatically as a result of compression. A representative AFM height image obtained at $\pi = 45$ mN/m is shown in Figure 4-3 d. The ribbon-like structures disappeared; surface morphology was dominated by island-like domains. The average domain height markedly increased, yielding $h = 10.45$ nm (Table 1).

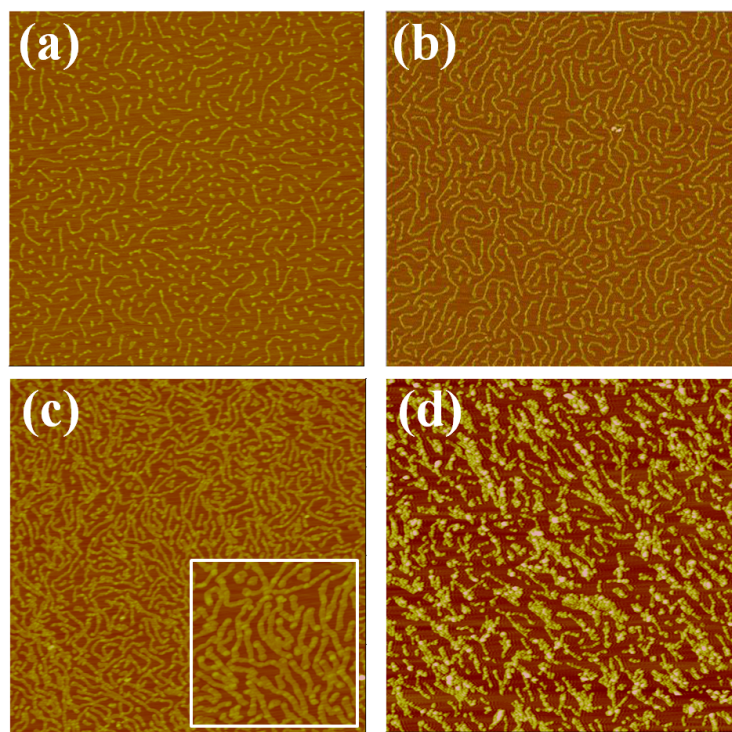


Figure 4-3. AFM height images of the CBCP Langmuir monolayers obtained from the chloroform solution at various transfer pressure: (a) $\pi = 0$ mN/m, (b) $\pi = 10$ mN/m, (c) $\pi = 22$ mN/m, and (d) $\pi = 45$ mN/m. Scan size = $10\ \mu\text{m} \times 10\ \mu\text{m}$ and z scale = 30 nm for all images. Scan size = $3\ \mu\text{m} \times 3\ \mu\text{m}$ for the insert in (c).

Effects of assembly time and solvent at zero surface pressure

The spontaneous self assembly of CBCP at $\pi = 0$ mN/m for longer time was investigated. After being placed on the water surface, the CBCP solution was allowed to evaporate for 2 h rather than 30 min as described in the above (Figure 4-4). Figure 4-4a shows a typical AFM height image of resulting LB film after the evaporation of chloroform for 2 h. In comparison with the surface morphology assembled for 30 min (Figure 4-4a), the longer assembly time led to a substantial elongation of ribbons (Figure 4-4 b); the surface coverage of ribbons increased from 24% to 30% (Table 1). The ribbon width, however, remained constant within the error limit, suggesting that more CBCP molecules diffused to the tip of ribbon to grow into a longer ribbon. The diffusion of free CBCP molecules was enabled by the trapped solvent around ribbons. The sample after even longer evaporation time (i.e., 3 h) was also measured; notably, no further increase in the ribbon length was observed. The growth of ribbons was locked after complete solvent evaporation (i.e., 2 h). The morphological change (comparing Figure 4-3a with Figure 4-4a) signified that the aggregation (i.e., self-assembly) of polymers at the air/water interface for a short period of time was not in its equilibrium state but rather represented a kinetically trapped situation.¹⁷

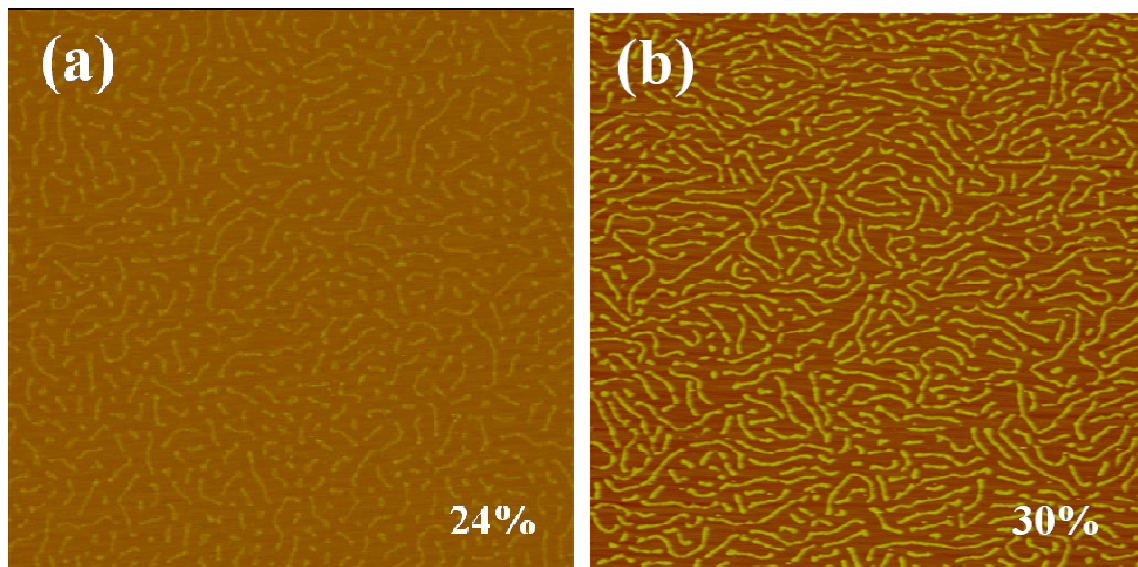


Figure 4-4. AFM height images of the CBCP Langmuir monolayers obtained after solvent evaporation from chloroform solution for 30 min (a) and 2h (b). The surface coverage of a is 24% and b is 30%.

Solvent was found to exert profound influence on the self-assembly of CBCP at $\pi = 0$ mN/m. Chloroform is a highly volatile solvent with the boiling point, bp = 61.2 0C, thus CBCP had much shorter time to self assemble before kinetically trapped in its “frozen state” upon the complete solvent evaporation. By contrast, toluene is a less volatile solvent with bp = 110.6 0C. Therefore, comparing to the CBCP chloroform solution, when toluene was used as the spreading solvent, it is possible to achieve a state that was relatively closer to the final equilibrium state by providing CBCP molecules with longer time to self assemble, yielding a cellular pattern (i.e., interconnected network structures; Figure 4-5b) composed of ribbons of the same width and height as those shown in Figure 4-6 a.

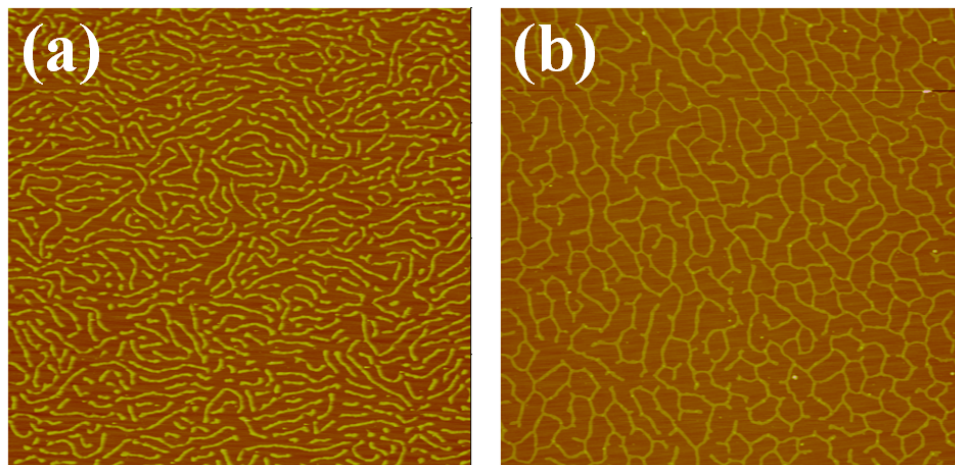


Figure 4-5. AFM height images of the CBCP Langmuir monolayers obtained after solvent evaporation for 2 h. (a) from chloroform solution, and (b) from toluene solution. The deposition pressure, $\pi = 0$ mN/m. Scan size = $10\ \mu\text{m} \times 10\ \mu\text{m}$ and z scale = 30 nm for both images.

Mechanism for self-assembly at $\pi = 0$ mN/m

Ribbon-like structures have been observed in LB depositions of amphiphilic copolymers, for example, arborescent graft copolymers polystyrene-*graft*-poly(ethylene oxide) (PS-*g*-PEO in which PS and PEO were the core and the shell, respectively).¹⁵ They were formed by the pressure-induced association of these dendritic molecules. The formation of ribbons was reversible; upon the release of pressure, the ribbons dissociated into dendritic graft copolymers.¹⁵ In stark contrast, the ribbons produced from the CBCP were inherently a stable structure: it yielded at $\pi = 0$ mN/m and can grow with time at that pressure or at higher pressure. Steric crowding between the hydrophobic PS blocks caused the hydrophilic A block to stretch. As a result, A chain appeared as a rigid rod.²¹ The length of rigid A block was about 53.6 nm, estimated using *Material Studio*.

As depicted in Figure 4-6 a, two CBCP molecules aggregated head to head to yield a pair (i.e., red B blocks on the top and the bottom with blue C blocks in the middle). Then

this polymeric pair assembled side by side with adjacent pairs to form a long ribbon (for example, ribbon 1 in Figure 4-6 a). The long hydrophilic B chains were adsorbed on the water surface around the chemically linked PS arms (i.e., C blocks), keeping the neighboring ribbons apart (for example, ribbon 2 in Figure 4-6 a). In such a model, the width of ribbon was dictated by the length of two stretched A block in the pair. According to the calculation from *Material Studio*, the length of two A blocks was about 107 nm, which coincided with the width of ribbon measured from the AFM images (i.e., ~ 100 nm). The small discrepancy between the prediction and the measured width can be attributed to the fact that, in the experiment, two CBCP molecules may overlap one another to some extent when forming a polymeric pair.

We now address qualitatively how the dispersed ribbons initially formed at $\pi = 0$ mN/m by discussing the formation of cellular pattern when the CBCP toluene solution was used. The stability of a thin liquid film (< 100 nm) on the substrate was governed by the interplay of the long range intermolecular force (within the continuous film) and the short range intermolecular force (between the film and the substrate).²³ When the CBCP solution was placed on the water surface, it formed a thin continuous liquid film (312.5 nm thick, which was calculated by dividing the solution volume (5 μ L) by the surface area of LB trough (160 cm²)), stabilized by the positive spreading coefficient of toluene on the water.²⁴ As the solvent evaporated, the liquid film became thinner (< 100 nm), and the increased contribution from the unfavorable interfacial interactions between PS arms (i.e., C blocks) and water eventually resulted in the dewetting of thin film. The dewetting of thin film can be proceeded via three stages.²³ First, the film ruptures, thereby generating randomly distributed holes.

Second, the holes then grow and the rims ahead of the holes eventually merge to form a cellular structure. Third, the resulting ribbons in the cellular pattern are unstable and decay into droplets. It is clear that the observed cellular pattern resembled the morphology formed in the second stage of dewetting process.²⁴ As the holes grew during the solvent evaporation, the concentration of CBCP was greatly increased, leading to the aggregation of PS chains (i.e., C blocks) and thus the formation of ribbon-like structures (Figure 4-6a) to reduce the overall free energy of the system. Because the formation of cellular pattern could eliminate the existence of ribbon tips, a position possessing high free energy, the ribbons tended to be connected, forming continuous cellular pattern.

When the more volatile solvent chloroform was used, the dewetting process occurred very quickly. The rapid solvent evaporation happened faster than the CBCP molecules can proceed to a relatively energetically favorable state by forming the cellular structures. As such, the limited polymer mobility only allowed short dispersed ribbons to be formed (Figure 4a).

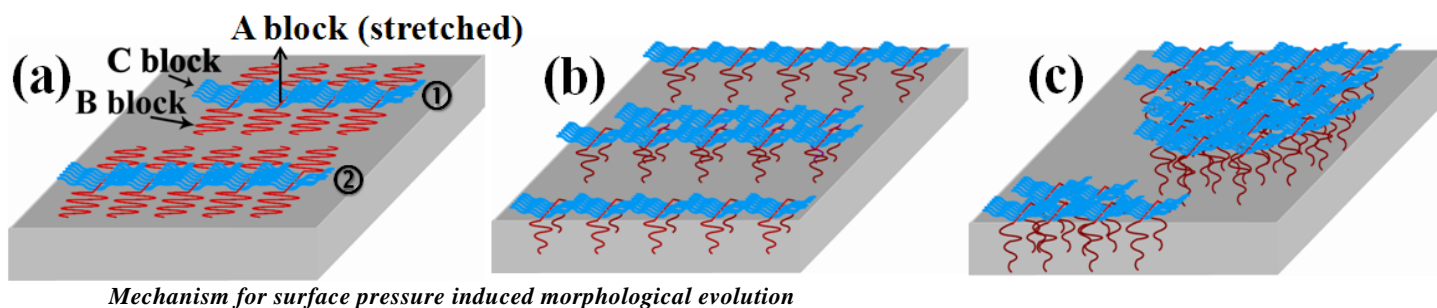


Figure 4-6. Schematic illustration of the packing of microstructures at different surface pressures.

B block in red = hydrophilic block, and C block in blue = PS block (i.e., arms).

Figure 4-6 illustrates the mechanism for the surface pressure induced morphological change in CBCP. At low surface pressure, the PS aggregates (i.e., ribbons) were separated by the hydrophilic B blocks, which were adsorbed on water surface (Figure 5a). There was internal pressure built up by elastic repulsive force between these hydrophilic chains to keep adjacent ribbons apart.

In the plateau region, the hydrophilic B blocks partially submerged into water subphase to form a brush-like structure (Figure 4-6 b), and thus the surface pressure remained constant while the surface area progressively decreased. Such desorption of hydrophilic chains from water surface and submergence into water subphase led to weaker repulsive force between the ribbons. Consequently, the ribbons can associate one another side by side (the insert in Figure 4-2c and Figure 4-6b). This process also caused an increase in the ribbon height from roughly 4.5 nm to 5.57 nm. This is because when the film was transferred onto the Si substrate, the hydrophilic chains in the water subphase were trapped between the PS chains and the Si substrate. As a result, the PS ribbons were situated on a layer of hydrophilic B blocks, giving rise to a larger height.

When the surface pressure was larger than 22 mN/m, the hydrophilic chains were completely submerged into the water, leading to a dramatic increase in height from 5.57 nm to 10.45 nm (Table 4-1). Because no repulsive force caused by hydrophilic chains was present, the PS chains can aggregate in any direction. Thus, an island-like morphology was formed (Figure 4-3d).

In order to verify the above proposed model for the surface pressure induced morphological evolution, compression–expansion cycle and solvent annealing studies

were preformed. Hysteresis effects have been proven to be very informative in elucidating the dynamic behavior of amphiphilic polymers under different surface pressure.^{4,19} Before the plateau region (curve a in Figure 4-7), a small hysteresis was observed, which may be caused by the rearrangement or overlap of hydrophilic chains on the water surface.⁴ The hysteresis in the plateau region was due to the desorption of hydrophilic chains from the water surface (i.e., partial submergence into water subphase), and upon the release of surface pressure, these chains must overcome the energy barrier to become adsorbed again on the water surface (curve b in Figure 4-7).¹⁹ After the release of surface pressure at $\pi = 24$ mN/m in the condensed state region, the pressure dramatically decreased to a minimum of 18 mN/m at the surface area of 240 nm²/molecule and then increased again to form the hysteresis (curve c in Figure 4-7). This may be due to the entanglement of hydrophilic B blocks in the brush-like structure (Figure 4-6c). Similar phenomenon has been observed in PS-b-PEO diblock copolymer.⁴

Effect of solvent vapor annealing on the morphology of CBCP

Selective solvents were used in solvent vapor annealing on the deposited CBCP films. Specially, carbon disulfide (CS₂) and methanol were utilized to selectively swell the hydrophobic PS block and the hydrophilic blocks in CBCP, respectively. Four LB films obtained at $\pi = 20$ mN/m were annealed in CS₂ and methanol vapors for 2 h and 7 h, respectively. The typical morphologies after annealing are shown in Figure 19. Comparing the sample before annealing with one annealed in CS₂ vapor, the height of ribbons remained unchanged (Table 4-1) and the morphology did not change perceptibly. However, the surface coverage of ribbons increased to 40.5%

(Table 4-1), resulting from the swelling of PS blocks laterally by CS₂. For the annealing by methanol vapor, however, the morphology profoundly changed. The height of ribbons increased dramatically from roughly 4.5 nm to 13.57 nm after annealed for 2 h. It further increased to 17.54 nm after annealed for 7 h. The methanol vapor annealing greatly enhanced the mobility of ribbons on the Si substrate by promoting the mobility of the hydrophilic A and C blocks which were anchored to the Si substrate for the LB film deposited at $\pi = 20$ mN/m. Additionally, upon methanol vapor annealing, the unfavorable interfacial interaction between the hydrophobic PS blocks and the hydrophilic Si substrate may drive the hydrophilic chains under the PS ribbons. This would form a continuous layer of hydrophilic chains between the PS blocks and the Si substrate and explain a large increase in the ribbon height. Taken together, the ribbons were dragged closer to one another, yielding densely packed morphology. As a consequence, the surface coverage of ribbons markedly increased from 31.5% to 54% after 2 h to 93.1% after 7 h methanol vapor annealing. Since methanol is non-solvent for PS, the shape of PS was not changed.

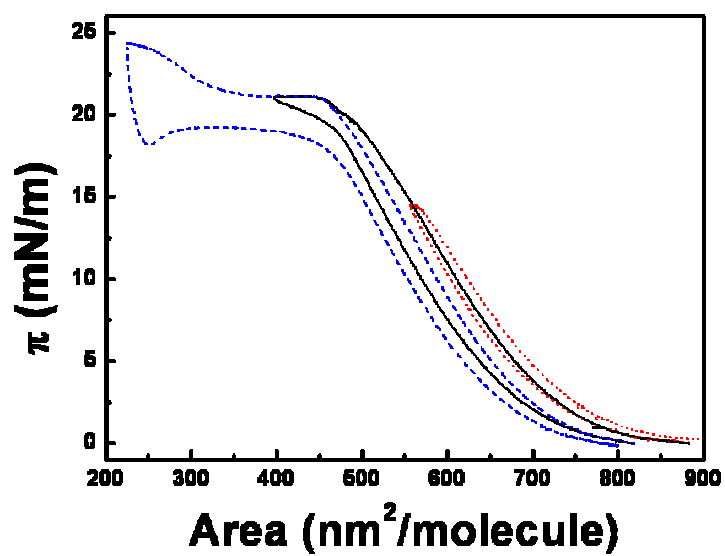


Figure 4-7. Representative compression–expansion cycles of the CBCP ended in the different regions: (a) extended liquid state region, (b) plateau region, and (c) condensed state region.

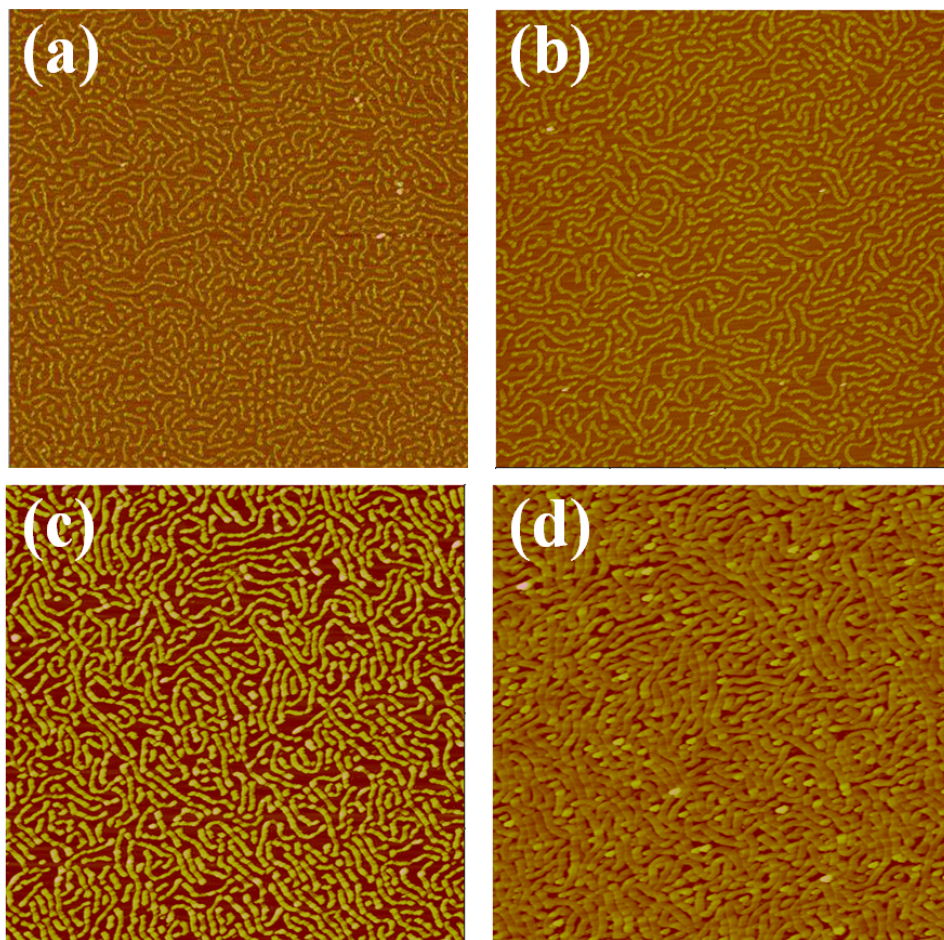


Figure 4-8. AFM height images of the CBCP film originally deposited from the chloroform solution at $\pi = 20$ mN/m (a) before, and (b) after CS₂ vapor annealing for 7 h; after methanol vapor annealing for (c) 2 h, and (d) 7 h. Scan size = 10 $\mu\text{m} \times 10 \mu\text{m}$ and z scale = 30 nm

4.4 conclusion

In summary, we have systematically explored the self-assembly of a newly synthesized amphiphilic CBCP at the air/water interface. The CBCP spontaneously assembled into ribbon-like structures on the water surface at the zero surface pressure. Combining the *Materials Studio* modeling with the assembly time effect study, a possible model was proposed to illustrate the formation of ribbons. The dewetting process was found to play a key role in initiating the self-assembly process and leading to the formation of the

dispersed ribbons. The morphological change of the LB films induced by the surface pressure was also scrutinized and was caused by the desorption of hydrophilic blocks on the water surface. This mechanism was supported by the compression–expansion cycle and the solvent vapor annealing experiments. The present study provides insight into the design of controllable pattern formation using amphiphilic copolymers.

References:

- (1) Cheyne, R. B.; Moffitt, M. G. *Langmuir* **2006**, *22*, 8387.
- (2) Fasolka, M. J.; Harris, D. J.; Mayes, A. M.; Yoon, M.; Mochrie, S. G. J. *Physical Review Letters* **1997**, *79*, 3018.
- (3) Aksay, I. A.; Trau, M.; Manne, S.; Honma, I.; Yao, N.; Zhou, L.; Fenter, P.; Eisenberger, P. M.; Gruner, S. M. *Science* **1996**, *273*, 892.
- (4) daSilva, A. M. G.; Filipe, E. J. M.; dOliveira, J. M. R.; Martinho, J. M. G. *Langmuir* **1996**, *12*, 6547.
- (5) Cox, J. K.; Yu, K.; Eisenberg, A.; Lennox, R. B. *Physical Chemistry Chemical Physics* **1999**, *1*, 4417.
- (6) Cox, J. K.; Yu, K.; Constantine, B.; Eisenberg, A.; Lennox, R. B. *Langmuir* **1999**, *15*, 7714.
- (7) Cheyne, R. B.; Moffitt, M. G. *Langmuir* **2005**, *21*, 5453.
- (8) Park, J. Y.; Koenen, N.; Forster, M.; Ponnampati, R.; Scherf, U.; Advincula, R. *Macromolecules* **2008**, *41*, 6169.
- (9) Francis, R.; Skolnik, A. M.; Carino, S. R.; Logan, J. L.; Underhill, R. S.; Angot, S.; Taton, D.; Gnanou, Y.; Duran, R. S. *Macromolecules* **2002**, *35*, 6483.
- (10) Peleshanko, S.; Gunawidjaja, R.; Jeong, J.; Shevehenko, V. V.; Tsukruk, V. V. *Langmuir* **2004**, *20*, 9423.
- (11) Peleshanko, S.; Jeong, J.; Gunawidjaja, R.; Tsukruk, V. V. *Macromolecules* **2004**, *37*, 6511.
- (12) Genson, K. L.; Hoffman, J.; Teng, J.; Zubarev, E. R.; Vaknin, D.; Tsukruk, V. V. *Langmuir* **2004**, *20*, 9044.

- (13) Gunawidjaja, R.; Peleshanko, S.; Tsukruk, V. V. *Macromolecules* **2005**, *38*, 8765.
- (14) Peleshanko, S.; Sidorenko, A.; Larson, K.; Villavicencio, O.; Ornatska, M.; McGrath, D. V.; Tsukruk, V. V. *Thin Solid Films* **2002**, *406*, 233.
- (15) Njikang, G. N.; Cao, L.; Gauthier, M. *Langmuir* **2008**, *24*, 12919.
- (16) Njikang, G. N.; Cao, L.; Gauthier, M. *Macromolecular Chemistry and Physics* **2008**, *209*, 907.
- (17) Baker, S. M.; Leach, K. A.; Devereaux, C. E.; Gragson, D. E. *Macromolecules* **2000**, *33*, 5432.
- (18) Devereaux, C. A.; Baker, S. M. *Macromolecules* **2002**, *35*, 1921.
- (19) Zhu, J.; Eisenberg, A.; Lennox, R. B. *Macromolecules* **1992**, *25*, 6547.
- (20) Runge, M. B.; Lipscomb, C. E.; Ditzler, L. R.; Mahanthappa, M. K.; Tivanski, A. V.; Bowden, N. B. *Macromolecules* **2008**, *41*, 7687.
- (21) Runge, M. B.; Bowden, N. B. *Journal of the American Chemical Society* **2007**, *129*, 10551.
- (22) Logan, J. L.; Masse, P.; Dorvel, B.; Skolnik, A. M.; Sheiko, S. S.; Francis, R.; Taton, D.; Gnanou, Y.; Duran, R. S. *Langmuir* **2005**, *21*, 3424.
- (23) Reiter, G. *Physical Review Letters* **1992**, *68*, 75.
- (24) Muller-Buschbaum, P. *Journal of Physics-Condensed Matter* **2003**, *15*, R1549.

Chapter 5. Self-Assembly of Polystyrene-Polylactide Bottlebrush Block Copolymer at the Air/Water Interface

5.1 Introduction

As one of most typical film preparation methods, the Langmuir-Blodgett (LB) technology has been widely utilized to produce copolymer films with mono- or multi-molecule layers.¹ These copolymer films with well controlled thickness have been attracting considerable attention due to their broad range of potential applications in microlithography,² devices,³ and biomimetic thin films.⁴ The overall property of these copolymer Langmuir films is closely related to their surface morphology, which is dictated by a number of parameters, including the solution concentration, surface pressure, and temperature.^{2,5-7}

The interfacial behavior of amphiphilic copolymer at the air/water interface has been extensively studied since the pioneering work of Eisenberg and Lennox.^{5,8-10} To date, the so called “pancake” and “brush” models have been established and proved quite effective in understanding the air/water interfacial behavior of a variety of amphiphilic copolymers, such as linear block copolymers,^{2,6,7,11,12} star copolymers,¹³⁻¹⁷ comb block copolymers,¹⁸ dendritic polymers,^{19,20} ²¹ etc. The “pancake” model refers to the morphology of copolymer LB film formed at low surface pressure. In this model, the hydrophilic blocks spread over the water surface, forming the pancake-like morphology; while the hydrophobic blocks aggregate and sit on the hydrophilic “pancake” to reduce the surface energy. Under the higher compression pressure, the “pancake” is transformed into the “brush”, i.e., the spread hydrophilic blocks are expelled into the water subphase, yielding the brush-like morphology (“brush” model). According to these two models, the

presence of hydrophilic blocks is essential for the formation of Langmuir monolayer because they facilitate the tethering of whole copolymer chain on the water surface. As a result, self-assembly of LB films has been primarily focused on amphiphilic copolymers. By contrast, no study on hydrophobic copolymers at the air/water interface has been pursued. In this paper, both bottle brush and linear block copolymers of hydrophobic polystyrene-poly lactide were found, for the first time, to be capable of forming the Langmuir monolayers on the water surface. The systematic studies showed that they displayed unique assembly behaviors at the air/water interface, which can no longer be understood by the classic “pancake” and “brush” models.

The polystyrene-poly lactide (PS-PLA) block copolymers were selected in the present study because of the biodegradable nature of PLA blocks.²² The thin films of these copolymers are promising in biomedical and pharmaceutical application.²³ Notably, all previous research on the PS-PLA block copolymers are limited in their self-assembly in bulk and thin films,²⁴⁻²⁷ and no self-assembly of Langmuir monolayer has ever been reported. Recently, a novel ultrahigh molecular weight PS-PLA bottle brush block copolymer (BBCP) was synthesized by a combination of living radical and ring-opening polymerizations.²⁴ The PS-PLA BBCP is a comb-like macromolecule with highly densely grafted PS and PLA branches along the polymethacrylate backbone. The backbone is much longer than the branches. The steric effect of adjacent branches cause the backbone to stretch out, leading to the formation a rigid cylindrical macromolecule as illustrated in Figure 5-1a.^{24,28,29} Furthermore, the densely branched structure and large cross sectional area of cylindrical shape of BBCP result in little entanglement between the BBCP melts.^{29,30} The unique properties described above together with their large

domain size and domain spacing originating from the ultrahigh molecular weight nature of BCCP, make BCCP a perfect candidate to explore their self-assembly behavior at the air/water interface.

In this paper, the Langmuir isotherms and surface morphologies of BCCP were presented. The structure of deposited LB films of BCCP was then determined by the AFM measurement, thermal annealing, and enzymatic degradation experiment. A linear block copolymer (LBCP) of PS-PLA with relatively similar molecular length and composition ratio to BCCP was employed and served as the reference to elucidate the influence of chemical architecture on the air/water interfacial behavior of PS-PLA Langmuir monolayers (Figure 5-1b). Combined with the study of PS-PLA LBCP, the surface behavior of PS-PLA block copolymer systems at the air/water interface was finally revealed.

The chemical structure and molecular morphology of PS-PLA BCCP are depicted in Figure 5-1 a and 5-1 c. The PS (red) and PLA (white) branches are densely grafted along the polymethacrylate backbone through the ester group. The backbone can be divided into two parts with same length, namely, one grafted with PLA arms (i.e., PLA part) and the other grafted with PS arms (i.e., PS part). The volume fraction of PS is calculated to be 60% using the known densities of $\rho_{PS} = 1.04$ and $\rho_{PLA} = 1.25$ g/mL. The length of BCCP backbone, L_{BCCP} was about 90 nm (Figure 5-2 a) and the length of PLA and PS arms are 6.3 nm and 6.5 nm, respectively obtained by performing energy minimization using *Material Studio 4.1*. Because of steric crowding of PLA and PS arms, the BCCP adopts a relatively rigid cylindrical morphology, with the aspect ratio of the length to diameter, $L/D = 9$ (Figure 5-2 a). The chemical structure of PS-PLA linear block

copolymer (LBCP) is shown in Figure 5-2 b; the MW of PS and PLA blocks are 23,000 g/mol and 11,000 g/mol, respectively. The LBCP assumes a random coil conformation due to the absence of the steric effect of arms as in the case of BBCP. The length of LBCP is estimated to be 79 nm with PS block of 45 nm and PLA block of 34 nm (Figure 5-2 b). The volume fraction of PS in the LBCP is 71.4%.

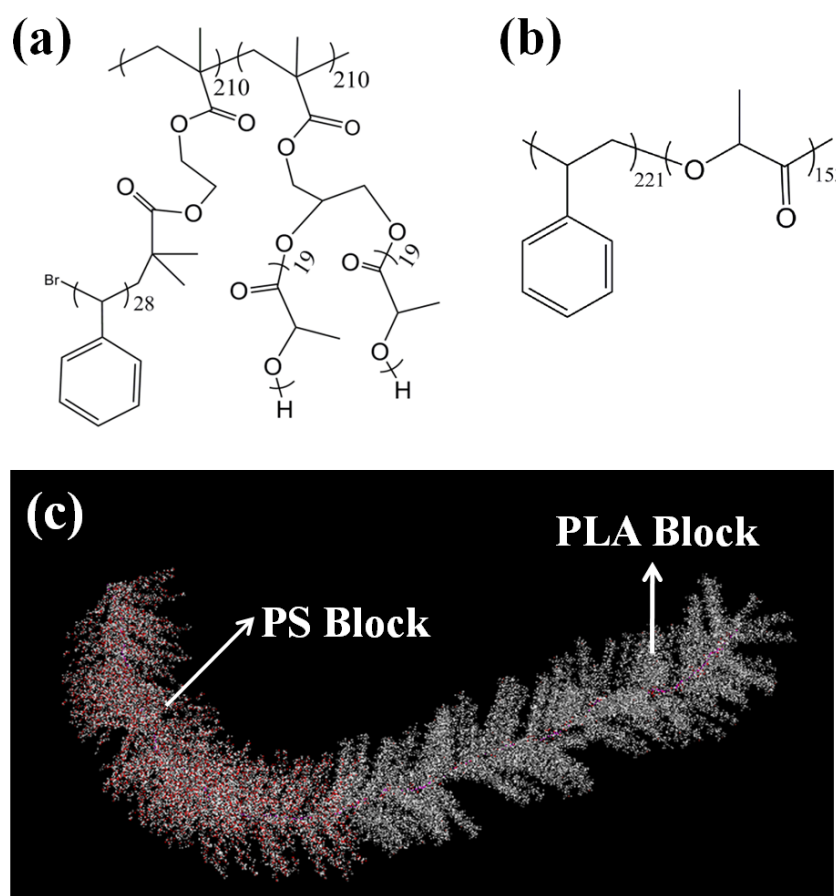


Figure 5-1. Chemical structures of (a) bottlebrush copolymer (BBCP), and (b) PS-b-PLA linear block copolymer (LBCP). (c) Molecular morphology of BBCP

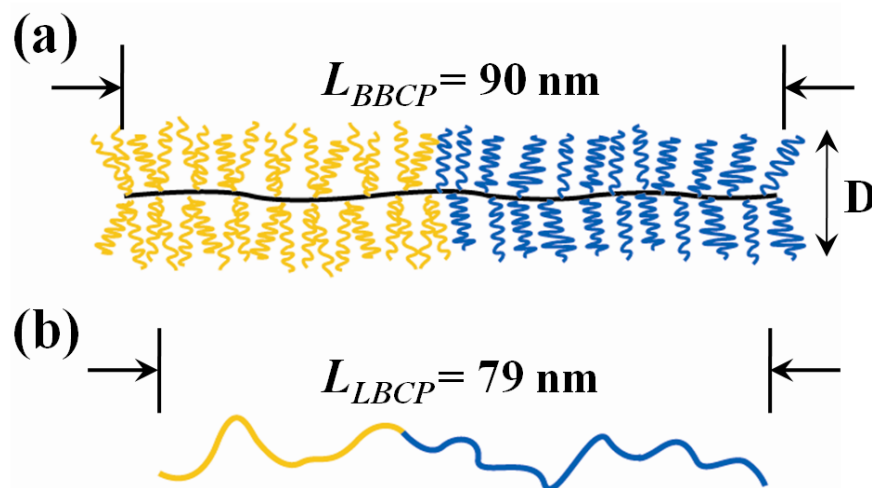


Figure 5-2. Schematic representations of (a) *bottlebrush copolymer* with PLA (yellow) and PS (blue), and (b) a *linear block copolymer* of PS-b-PLA, in which PLA and PS blocks are in yellow and blue, respectively.

5.2 Experimental Section

Previously synthesized BBCP with an ultrahigh molecular weight of 1200 kg/mol was utilized in the present study. Linear PS-PLA block polymer with M_w 34 kg/mol was used as the reference. The dimensions of both copolymers were estimated from molecular models by performing energy minimization using *Material Studio 4.1*. Chloroform (99.9%, Fisher Chemicals), Proteinase K (sigma, lyophilized powder) were purchased and used without further purification. The BBCP and LBCP chloroform solutions at the concentration, $c = 2 \times 10^{-3} \text{ g/ml}$, were prepared. Surface pressure \sim area ($\pi \sim A$) isotherms and polymer monolayers were obtained with R&K Langmuir Blodgett (LB) system (Riegler & Kirstein, GmbH, 160 cm^2 Teflon trough). The trough was carefully cleaned with 1:1 H_2O_2 : NH_3OH solution overnight and subsequently rinsed with DI water.

(NanoPure, $> 18 \text{ M}\Omega \text{ cm}$) for 5 times. After the solvent evaporated for 30 min, the monolayer film was compressed at a rate of $150 \text{ }\mu\text{m/sec}$.

Si substrate used for depositing LB films was cleaned with a mixture of sulfuric acid and Nonchromix, followed by rinsing with DI water and blown dry with N_2 . For LB depositions, the Si substrate was withdrawn at a rate of $35 \text{ }\mu\text{m/sec}$ while keeping the pressure constant. Thermal annealing was performed by keeping the deposited film at furnace for desired time and temperature.

The enzymatic degradation was performed by vertically immersing the CBCP deposited LB film into the degradation solution, prepared by adding 1.0 mg of Proteinase K into 5ml of Tris-HCl buffer (PH 8.6). The degradation was carried on at 37°C for 1hour in an oil bath. The scratch experiment was carried out by scratching the deposited LB film with a blade gently.

Morphologies of LB films were examined by Atomic Force Microscopy (AFM; Dimension 3000) in the tapping mode. The scanning rate was 2 Hz. Each sample was imaged at more than 5 locations to ensure the reproducibility of features observed. The average height and surface coverage of LB films were obtained by performing the bearing analysis. The spectral period was analyzed by performing 2 Fourier transform (FFT) of height image.

5.3 Result and discussion

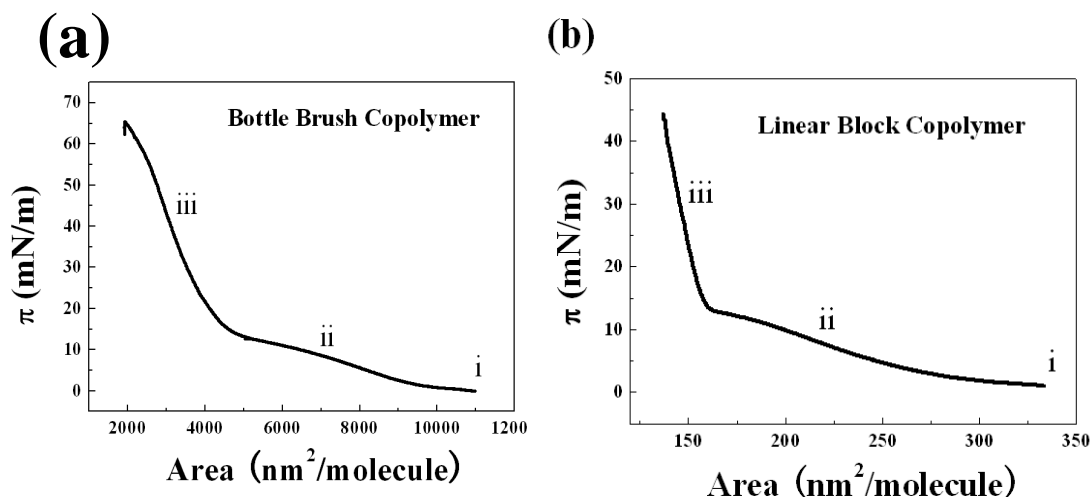


Figure 5-3. Pressure ~ area isotherms of the Langmuir monolayer of (a) BBCP and (b) LBCP.

Three regions are labelled as (i) gas state, (ii) liquid state, and (iii) condensed state.

Table 5-1 Height and surface coverage of BBCP dot-like domains obtained from AFM images

LB film	P=1 mN/m	P=5 mN/m	P=13 mN/m	P=30 mN/m
Domain height (nm)	3.672 ± 0.689	3.931 ± 0.871	3.643 ± 0.674	3.819 ± 0.89
Domain Diameter (nm)	68.753 ± 8.2	66.723 ± 7.79	66.065 ± 4.873	N
Domain Area Coverage (%)	29.839	37.945	52.995	66.123

Langmuir isotherm, i.e., surface pressure ~ area ($\pi \sim A$) plot, of the BBCP was shown in Figure 5-3 a. The continuous pressure rise was indicative of the formation of LB monolayer.¹ The entire isotherm can be generally divided into typical three regions according the slop of the curve, in other words, the pressure increasing rate with molecular area.^{1,5} They are (i) gas state region at $\pi = 0$ mN/m, (ii) liquid state region at $\pi = 0 \sim 13$ mN/m, (iii) condensed state region at $\pi > 13$ mN/m. Figure 5-4 shows the

representative AFM height images of LB monolayers obtained at three regions (deposited at $P=1, 5, 13$ and 30 mN/m, respectively). Dots-like structures with a broad size distribution were observed at all three regions. Table 2 summarizes the height of these domains and the resulting surface coverage. With the increasing of surface pressure, the domain shape did not change obviously, but its density was increased greatly, with surface coverage increasing from 29.839% to 66.123%. Besides, the initial dispersed dots-like domain begin to form the island-like morphology at the condensed state region. The height of these domains shows little difference in all the three regions within the limits of error.

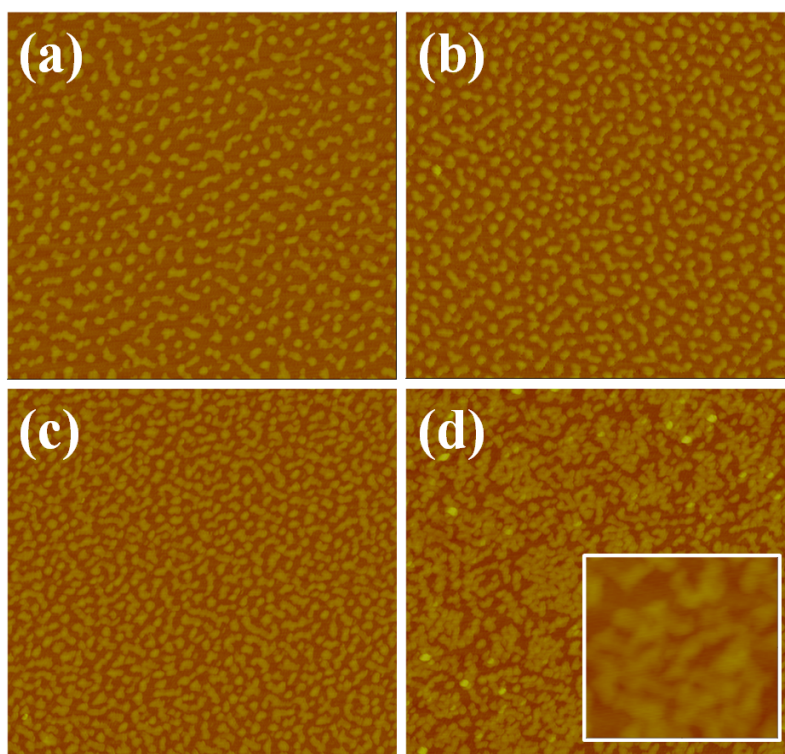


Figure 5-4. AFM height images of the BBCP Langmuir monolayers obtained from the chloroform solution at various transfer pressures: (a) $\pi = 1$ mN/m, (b) $\pi = 5$ mN/m, (c) $\pi = 13$ mN/m, and (d) $\pi = 30$ mN/m. Scan size = $3 \mu\text{m} \times 3 \mu\text{m}$ and scan size = $0.5 \mu\text{m} \times 0.5 \mu\text{m}$ for the insert in (d). The Height of the domain is shown in the up-right corner, and the its surface coverage is shown in the low-right corner.

The isotherm and dots-like morphology of BBCP resemble that of amphiphilic block copolymer,^{5,15,21} which assumes the “pancake” structure on the water surface (the hydrophobic blocks aggregate into the dot-like domain and the hydrophilic blocks forms the spreading phase among them). However, the facts, no domain height difference in all regions, can hardly be explained within the theory of amphiphilic copolymers (domain height should be greatly increased due to the formation of brush structure).⁵⁻¹¹ In order to understand surface behavior of the hydrophobic BBCP, the fine structure of the dots-like domains needs to be completely investigated. In the following step, the fine structure of the LB film was determined by the scratch test, enzyme degradation, as well as the thermal annealing.

Scratch test

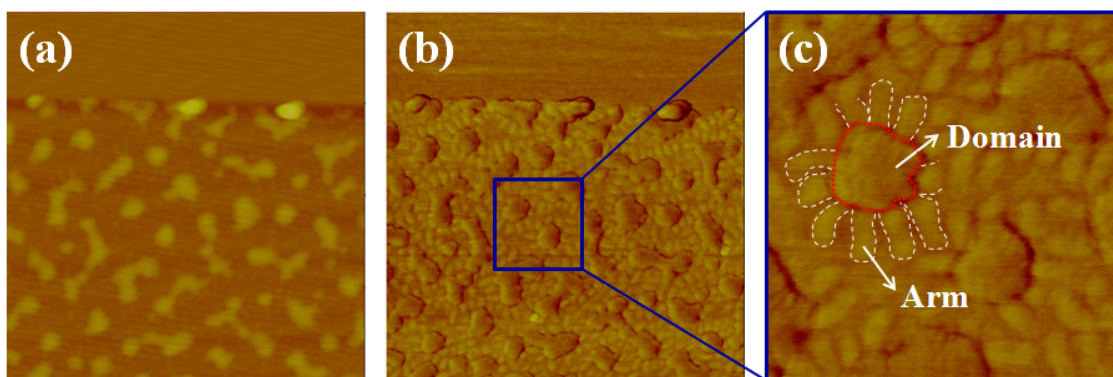


Figure 5-5. (a) AFM height image of the BBCP Langmuir monolayer obtained after scratching off the top portion of monolayer. Scan size = $1\ \mu\text{m} \times 1\ \mu\text{m}$. (b) The corresponding phase image of (a). (c) Close-up of the phase image in (b); the domain is enclosed with red dash line, and arms with white. Scan size = $0.3\ \mu\text{m} \times 0.3\ \mu\text{m}$

The Lb film (deposited at $P=5\ \text{mN/m}$) was scratched with a sharp blade, and the position around the cutting edge was examined with AFM (as shown in figure 5-5). The section analysis shows that the height different between cutting line and inter-domain

space is around 0.7 nm. Considering the damage caused by the blade on the silicon substrate, this height difference should be even smaller and can be ignored. This result shows that a spreading phase should also exist between the dot-like domains. This is reasonable, because no pressure can be applied on the LB film if the space between dot-like domains is empty. A Better resolution of morphology was achieved by phase image (as shown in figure 5-5b and 5-5c). It is well known that, in the phase image soft-tapping mode, the magnitude of the phase shift is directly related to the elastic modulus of the sample³¹, which means a better image contrast can be achieved for different materials. As shown in figure 5-5b, two distinct phases can be determined besides the silicon substrate: one phase (darker) composes the dot-like domain, and the other (lighter) is the cylindrical “arms” around the domain, forming the spreading phase. As shown in figure 5-5c, these arms are closely connected with the dots domains in a radial pattern. To the best of our knowledge, this is the time to observe the morphology of spreading phase with microscopy technique. The length of the arm is around 40 nm, and the width around 20 nm. Considering the twisting of polymer backbones,²⁴ these arms have the similar size as one part of BBCP (PS part or PLA part). This result shows that one part of BBCP (PS or PLA) composes the dot-like domains, and the other forms the spreading phases among them. By far, both the PS³² and PLA³³ has been reported to be able to form the spreading phase at air/water interface. To indentify the two phase in the LB film, thermal annealing experiment is performed.

Thermal Annealing

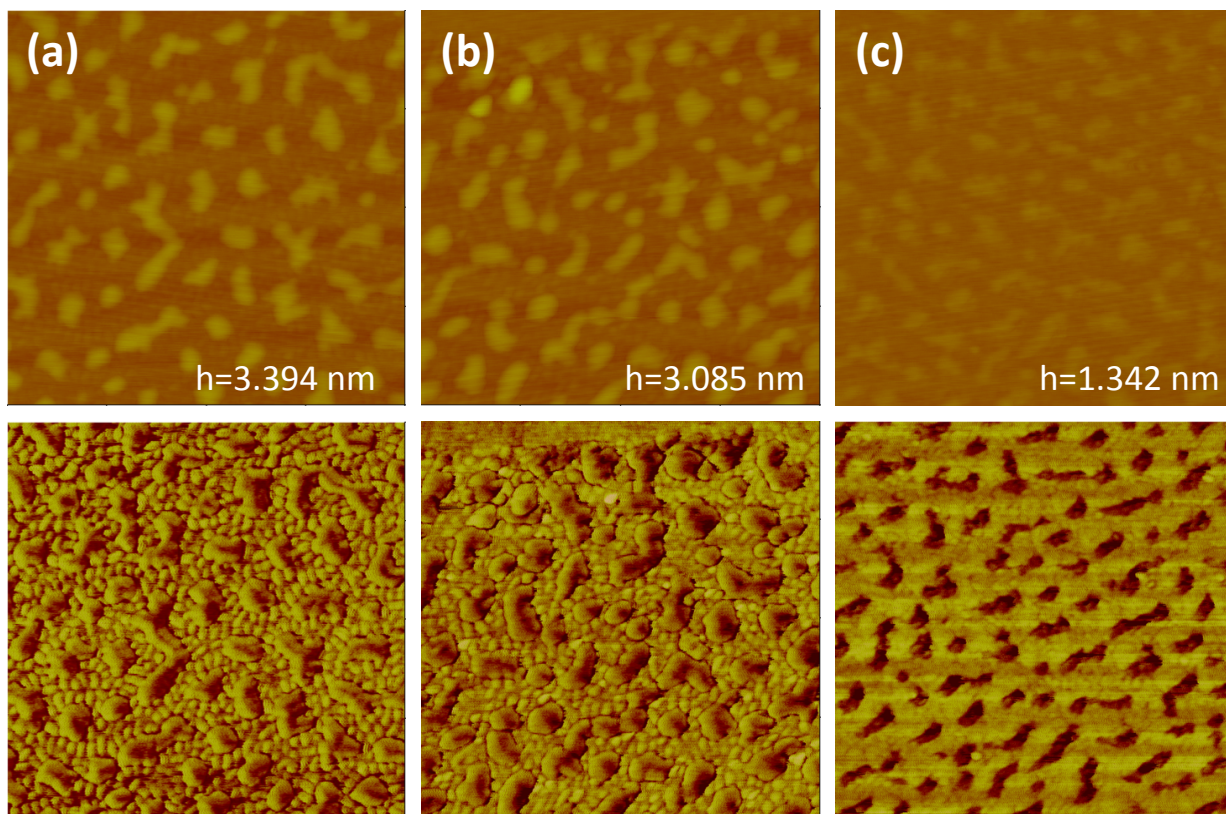


Figure 5-6. AFM height image (top) and phase image (low) of (a) original Langmuir monolayer, (b) monolayer annealed at 95°C for 12h, (c) monolayer annealed at 170°C for 5h. Scan size = 1 $\mu\text{m} \times 1 \mu\text{m}$, z scale = 50 nm, and phase scale = 50°. The bearing height of domains are labeled on each height images.

The molecular weight of PS and PLA braches in the BBCP is 3.0 and 1.4 Kg/mol respectively, which are smaller than critical entanglement molecular weights (14 kg/mol for PS³⁴, and 4 kg/mol for PLA³⁵). Therefore the whole molecules should be mostly free of entanglements above the glass transition temperature.^{24 29,30} The DSC analysis shows that the BBCP have two separate glass transitions at 54 °C and 104 °C, corresponding to PLA and PS respectively. Thus, the phase of dot-like domain can be identified by checking its decomposition temperature. The LB film (deposited at P=5 mN/m) was

annealed at 95 °C and 170°C, respectively. Figure 5-6 shows the AFM image of annealed morphology, and the domain height is labeled on each height image. The spectral periods (λ_c -c) of domains, analyzed by 2D FFT, are 124.6 ± 29.4 nm and 119.8 ± 28.1 nm, for the original and annealed samples respectively. The domain height remained the same and the armed domain morphology was well reserved as shown in the phase images (figure 5-6b). Considered the irregularity of domains and error limits of data, a conclusion can be drawn that no obvious change has been observed after annealing at 95 °C (far beyond the T_g of PLA). While annealed at 170°C (far beyond the T_g of PS), the domain height decreased dramatically, and the phase image was changed greatly. This result indicated that the domain is formed by the PS, and the “arm” like structure is the PLA part. When annealed at 170 °C, PS part of BBCP tend to separate from each, resulting in the decomposition of domains. The cylindrical molecular shape can be distinguished in the domain region from the phase image (figure 5-6c). Since the PLA “arms” are already well separated from each other, thus no obvious morphology change has been observed when annealed at 95 °C.

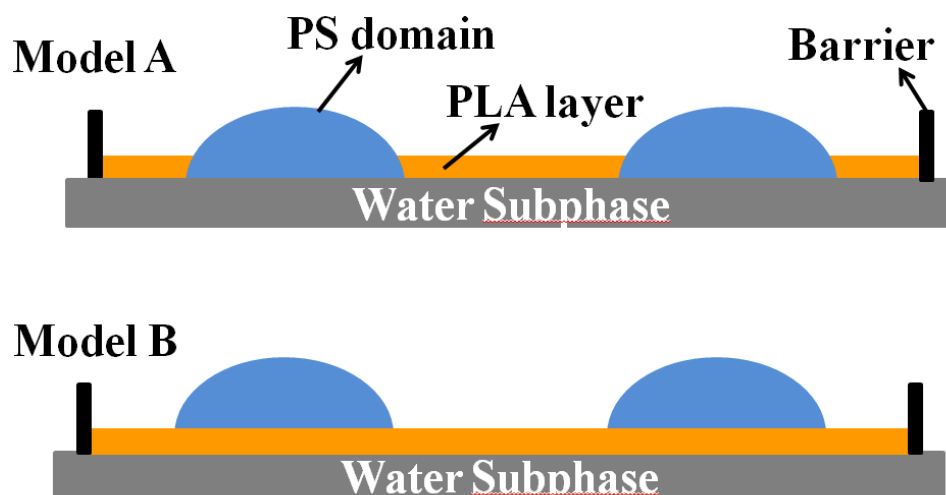


Figure 5-7. Schematic illustration of two models PS-b-PLA block copolymer at the air/water interface.

By now, there are still two different ways in which the polymer blocks could be arranged to yield the observed images. Two simple descriptions are shown schematically in figure 5-7. In model A, the domains are made up of the PS, which are separated by spread PLA arms. In model B, the PLA exist both around PS domain and beneath it, and PS domain sit on top of a coherent PLA layer. Such controversy also broadly exists in explaining air/water interfacial behavior of various amphiphilic copolymers^{5,11}. In order to determine the right model for the PS-PLA system, the enzyme degradation experiment was performed as following.

Enzymatic Degradation

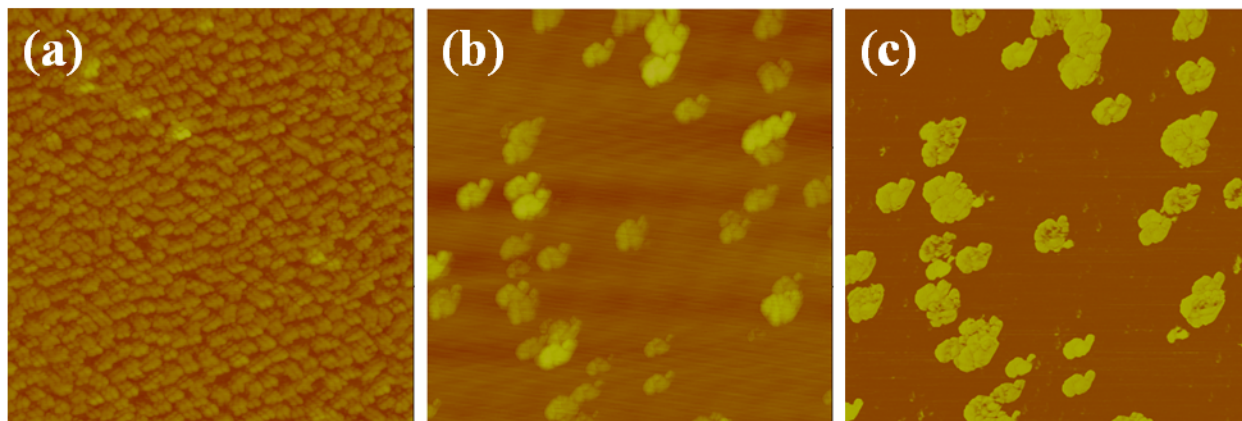


Figure 5-8. (a) AFM height image of Langmuir monolayer after immersion in the buffer solution without the addition of enzyme for 1h. (b) AFM height image of Langmuir monolayer undergoing enzymatic degradation for 1h. (c) Corresponding phase image of (b). Scan size = 3 μm \times 3 μm .

The basic idea behind this work was to degrade PLA polymer from the LB film, so that the positions of PLA phase can be directly identified. As shown in the introduction part, PLA is biodegradable polymers which can be degraded by both enzymatic degradation and alkaline hydrolysis.^{22,36} Considering the hydrolysis of ester group which connects PS branches and molecule backbone, enzymatic degradation was utilized here to keep PS part intact. The LB film (deposited at $P=5$ mN/m) was vertically immersed in both the buffer solution with and without enzyme under the same condition, so as to eliminate the influence of other factors. As shown in figure 5-8 a, the general dots-like domain morphology was generally reserved after soaked at buffer for 1h. The morphology is little blurry, which may be caused by the shearing force during the withdraw process or the swelling effect of water. After degradation in enzyme solution for 1hour, the circular domain still exists. However, they aggregated to form the huge aggregates, and nothing was left on the space region between these aggregates (as shown in figure 5-8 b and c).

First of all, the enzymatic degradation result confirms the fact that the dots-like domain is composed of PS part. Otherwise, it will be degraded and dissolved into the water. Besides, this result also shows that model B is the right case for PS-PLA system. As it is well known, the silicon substrate is one of the most common used high energy surfaces materials. The low energy surface materials, like organic polymers or water, tend to adsorb strongly onto it.³⁷ That is why the LB film can hardly be rinsed by the bare buffer solution. As for the case of model A, the intact PS domain array should be finally well reserved, with only spreading phase degraded. In contrast, when LB film takes the structure of model B, the PS domains can be stripped off the substrate after degradation of PLA beneath them. Since the water have a stronger wetting ability on the silica surface,³⁷ a water layer should form on the silicon substrate during PLA degradation process. The decreased attractive interaction between silicon substrate and PS polymers will lead to the aggregation of PS domains into huge aggregates, to reduce its surface tension in water. The AFM images in figure 5-8 b and 5-8 c clearly shows that the huge aggregates is actually composed of dot-like domains with same size as that of freshly deposited LB film (figure 5-4b).

Interfacial behavior of PS-PLA block copolymer

The fine structure of the BBCP film at low pressure has been clearly determined by the scratch test, thermal annealing, and enzymatic degradation experiment. After evaporation of spreading solvent (gas state region), the micro pressure, existing in the gas state region, assist the PS parts of BBCP to aggregates, forming the dots-like domain shape domains to reduce its surface energy. Although the PLA is a hydrophobic polymer,³³

they have certain hydrophilic units on its surface, like ester group, which can form the hydrogen bond with water and result in the attractive interaction between PLA and water subphase.³³ Therefore, the PLA part highly spread over the water subphase, and prevent the PS parts from further aggregation. Thus a monolayer is formed, with the structure shown in figure 5-9. With the increasing of surface pressure (liquid state region), the spreading PLA phase closely contacts with each other. The PLA parts were compressed, and a strong elastic repulsive force exist between them, just like the behavior of spreading phase in amphiphilic blocks copolymers.^{5,10} Therefore, a continuous pressure increase was observed in the region (ii) of the isotherm (figure 5-3 a). However, the PLA blocks were hydrophobic polymers, and can hardly be expelled into the water subphase. PLA arms around the PS domain have to rearrange themselves to release the elastic stress (as shown figure 5-9 b). Thus the surface area of spreading PLA phase was greatly decreased, leading to the increased density of dots-like domains. Finally, the PLA arms are strongly compressed and their arrangement is finished at the condensed region. The condensed LB film is hardly compressible, and the surface pressure increased dramatically with little decrease of molecular area, as shown in region (iii) of figure 5-3a. Under this highly pressure, the PLA arms can be expelled apart or overlapped (as shown in figure 5-9c), the PS domain become connected, forming a island like morphology (as shown in figure 5-4d). Since certain PLA arm still exist between the PS domains, the island is only loosely composed with gaps as shown in the insert of figure 4d. In the contrary, the amphiphilic block copolymer can form the more continuous island morphology, as the spreading phase was completely expelled into water subphase.³⁸

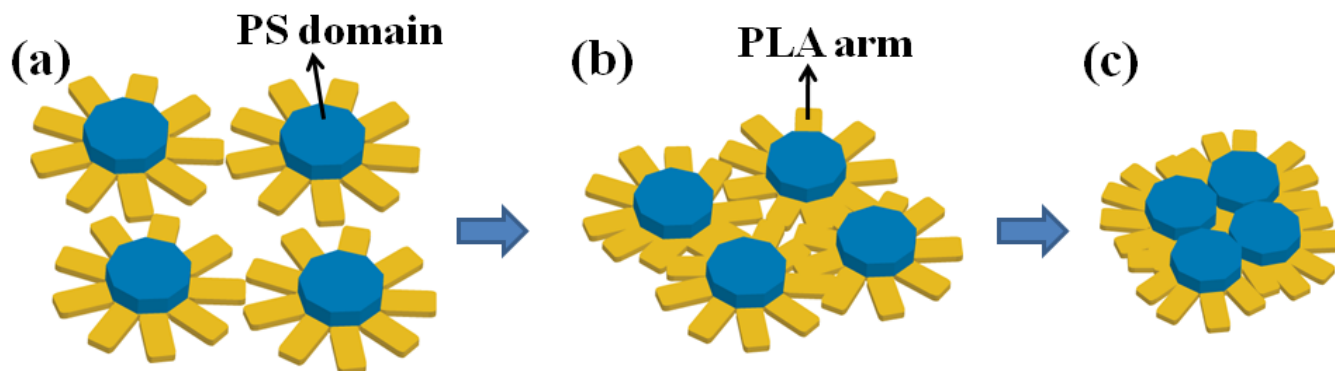


Figure 5-9. Schematic stepwise representation of the packing of microstructures of BBCP. (a) at the low pressure (i.e., between regions **i** and **ii**, where PLA arms (yellow) highly spread over the water surface, and PS (blue) form domains on the top of PLA; (b) at the intermediate pressure (i.e., region **ii**), where the rearrangement of PLA arms occur; and (c) at the high pressure (i.e., region **iii**), where the PLA arms are highly compressed, and PS domains become connected.

Result of linear block copolymer

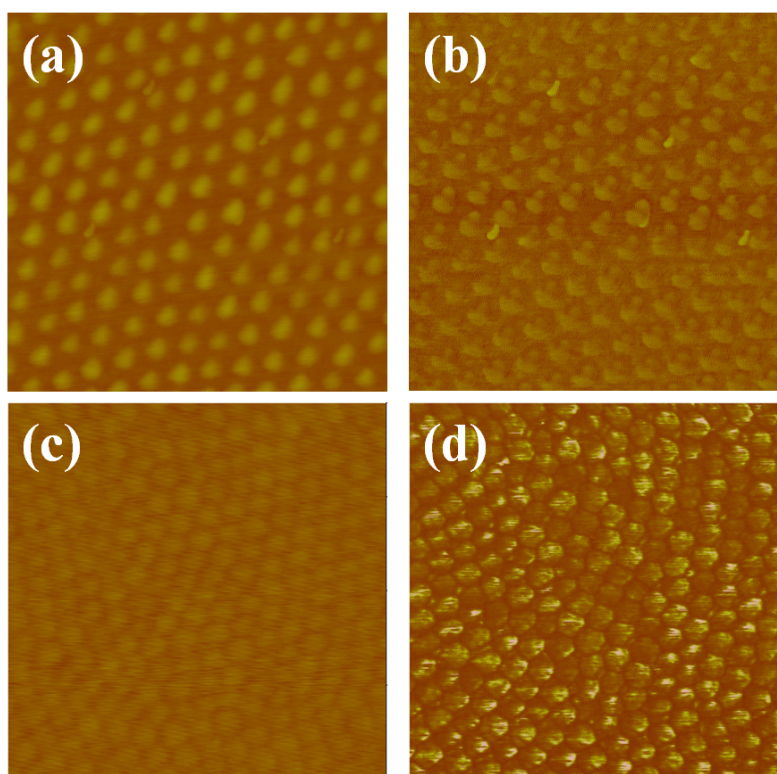


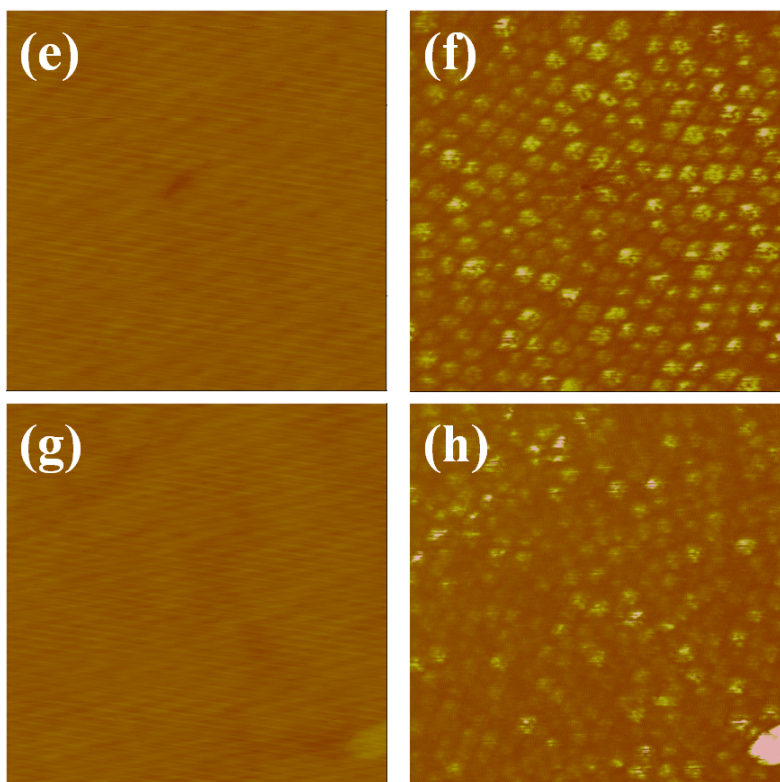
Figure 5-10 Continued

Figure 5-10. AFM height images (a, c, e and g) and corresponding phase images (b, d, f and h) of Langmuir monolayers of PS-b-PLA LBCP obtained from the chloroform solution at various surface pressures: (a) and (b) $\pi = 1$ mN/m, (c) and (d) $\pi = 5$ mN/m, (e) and (f) $\pi = 13$ mN/m, and (g) and (h) $\pi = 30$ mN/m. Scan size = $1 \mu\text{m} \times 1 \mu\text{m}$

To check the influence of bottle brush chemical structure on the LB film, linear PS-PLA block copolymer was used as the reference. As shown in figure 5-3 b, the Linear PS-PLA copolymer has similar isotherm curve as that of BBCP. The only different is the area of per molecule, due to different size of two polymers. The result shows that LBCP have the similar air/water interfacial behavior as BBCP. The AFM images of linear polymer LB film, deposited at pressures just like that of BBCP, were shown at figure 5-10. As shown in figure 5-10 a, more perfect dots-like structure was observed, with

similar diameter (around 59 nm) and bearing height (3.349 nm) as that of BBCP (68 nm and 3.672 nm respectively). It shows that PS domain is composed of more LBCP molecules, and the flexible characteristic of linear structure lead to more preface circular shape, which benefit the decrease of its surface energy. Due to higher volume fraction of PS block in LBCP (71.4%) than in BBCP (60%), the PS domain has a higher surface coverage (37.36%), compared with BBCP at same pressure (29.83%), No arm like structure can be observed in the phase image, since the PLA blocks has flexible linear structure, which entangled and spread on the water surface.

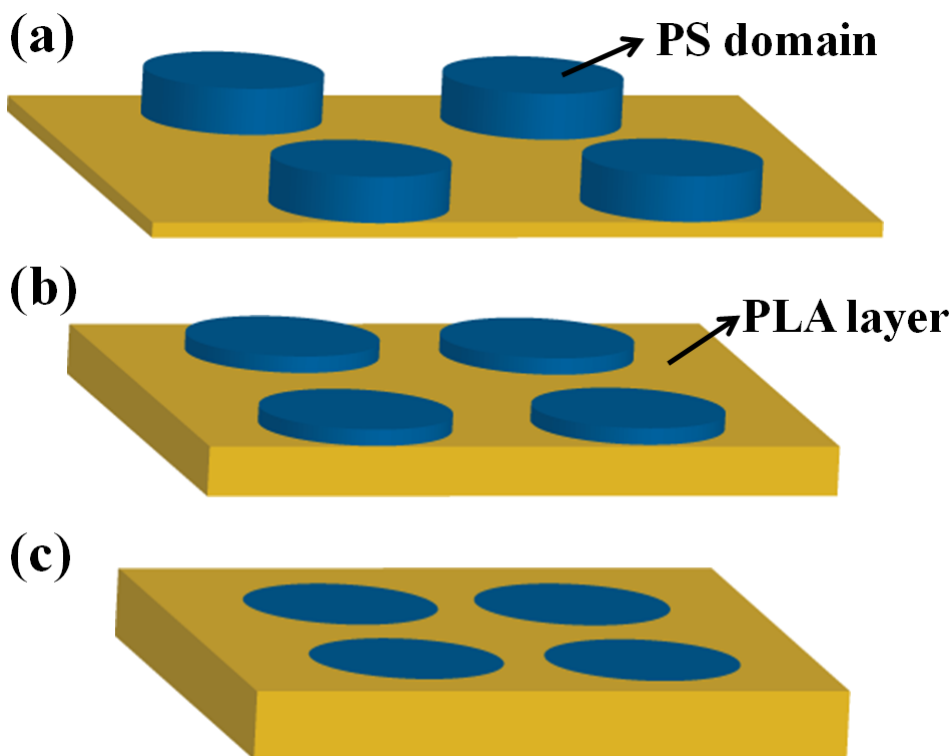


Figure 5-11. Schematic illustration of the packing of microstructures of PS-b-PLA LBCP at different surface pressures. (a) at the low pressure, where PLA arms (yellow) highly spread over the water surface, and PS (blue) form domains on the top of PLA). (b) at the intermediate pressure (i.e., region **ii**), where the folding of PLA chains lead more PLA to occupy the space between PS domains; and (c) at the high pressure (i.e., region **iii**), where the folding of PLA chains is complete, thereby leading to the formation of a topologically continuous film

At the pressure $P=5$ (liquid region), the domain height was decreased so dramatically that the PS domains was relatively hard to distinguish in the AFM height image (as shown in figure 5-10b). This result is in contrast with the common amphiphilic copolymers¹¹ and the BBCP in this work, which show little change in the domain height. However, the isotherm and phase image indicate that plenty PLA phase should exist between the PS domains. The decrease of domain height can be attributed to folding of flexible PLA chain. This folding process of PLA chains have also been reported in air/water interfacial behavior of linear PLA-PEO block copolymer.³³ Due to the folding of PLA chain, the surface stress can be released, and the space gap between PS domains can be filled (as shown in figure 5-11b). Therefore, the height difference between PS domain and spreading PLA phase is greatly reduced. At higher pressure ($P=13$ mN/m), the folding process of PLA chain is complete (as shown in figure 5-11c), and all the gap space between PS domain have been fully filled. Thus a smooth surface was detected by AFM height image as shown in figure 10c. But the PS domains (lighter) and PLA phase (darker) can still be distinguished at the corresponding phase images. As for the BBCP, the PLA arms can hardly be folded, due to their rigid backbones. Thus the PS domains is still highly dispersed under the sample pressure (figure 5-4c), and no changed was observed in the domain height (table 5-1). At extremely high pressure ($P=30$ mN/m), the film is highly compact (as shown in figure 29d), and the surface pressure increase dramatically with slight decrease of molecular area (region iii in figure 5-3b).

5.4 conclusion

In this project, we systematically investigated the air/water interfacial behavior of bottlebrush/ linear PS-PLA block copolymer. These hydrophobic blocks copolymer have unique behavior at the air/water interface, which can't be explained by the classic theory for amphiphilic copolymers. The fine structure of the LB film is clearly determined by the scratch test, thermal annealing and enzymatic degradation experiment. PLA blocks were found to spread over the water surface; while PS forms the dot-like domains and sit on the top of PLA phases. The AFM test show that the PLA form arm like structure around the PS domain in LB film of BBCP. It is the first time to observe the morphology of spreading phases in the LB work of block copolymer. A new model is proposed to illustrate the novel behavior of these two copolymer, and the influence of molecular chemical structure is also well analyzed .The present study not only fulfills the basic theory of langumuir-blodgett (LB) method, but also greatly enlarge the application range of this technology.

References:

- (1) Petty, M. C. *Cambridge ; New York : Cambridge University Press* **1996**.
- (2) Cheyne, R. B.; Moffitt, M. G. *Langmuir* **2006**, 22, 8387.
- (3) Fasolka, M. J.; Harris, D. J.; Mayes, A. M.; Yoon, M.; Mochrie, S. G. J. *Physical Review Letters* **1997**, 79, 3018.
- (4) Aksay, I. A.; Trau, M.; Manne, S.; Honma, I.; Yao, N.; Zhou, L.; Fenter, P.; Eisenberger, P. M.; Gruner, S. M. *Science* **1996**, 273, 892.
- (5) Zhu, J.; Eisenberg, A.; Lennox, R. B. *Macromolecules* **1992**, 25, 6547.
- (6) daSilva, A. M. G.; Filipe, E. J. M.; dOliveira, J. M. R.; Martinho, J. M. G. *Langmuir* **1996**, 12, 6547.
- (7) Cheyne, R. B.; Moffitt, M. G. *Langmuir* **2005**, 21, 5453.
- (8) Zhu, J.; Lennox, R. B.; Eisenberg, A. *Langmuir* **1991**, 7, 1579.
- (9) Zhu, J. Y.; Eisenberg, A.; Lennox, R. B. *Journal of the American Chemical Society* **1991**, 113, 5583.
- (10) Zhu, J.; Hanley, S.; Eisenberg, A.; Lennox, R. B. *Makromolekulare Chemie-Macromolecular Symposia* **1992**, 53, 211.
- (11) Cox, J. K.; Yu, K.; Eisenberg, A.; Lennox, R. B. *Physical Chemistry Chemical Physics* **1999**, 1, 4417.
- (12) Park, J. Y.; Koenen, N.; Forster, M.; Ponnampati, R.; Scherf, U.; Advincula, R. *Macromolecules* **2008**, 41, 6169.
- (13) Francis, R.; Skolnik, A. M.; Carino, S. R.; Logan, J. L.; Underhill, R. S.; Angot, S.; Taton, D.; Gnanou, Y.; Duran, R. S. *Macromolecules* **2002**, 35, 6483.

- (14) Peleshanko, S.; Gunawidjaja, R.; Jeong, J.; Shevehenko, V. V.; Tsukruk, V. V. *Langmuir* **2004**, *20*, 9423.
- (15) Peleshanko, S.; Jeong, J.; Gunawidjaja, R.; Tsukruk, V. V. *Macromolecules* **2004**, *37*, 6511.
- (16) Genson, K. L.; Hoffman, J.; Teng, J.; Zubarev, E. R.; Vaknin, D.; Tsukruk, V. V. *Langmuir* **2004**, *20*, 9044.
- (17) Gunawidjaja, R.; Peleshanko, S.; Tsukruk, V. V. *Macromolecules* **2005**, *38*, 8765.
- (18) Zhao, L.; Goodman, M. D.; Bowden, N. B.; Lin, Z. Q. *Soft Matter* **2009**, *5*, in press.
- (19) Peleshanko, S.; Sidorenko, A.; Larson, K.; Villavicencio, O.; Ornatska, M.; McGrath, D. V.; Tsukruk, V. V. *Thin Solid Films* **2002**, *406*, 233.
- (20) Njikang, G. N.; Cao, L.; Gauthier, M. *Langmuir* **2008**, *24*, 12919.
- (21) Njikang, G. N.; Cao, L.; Gauthier, M. *Macromolecular Chemistry and Physics* **2008**, *209*, 907.
- (22) Tokiwa, Y.; Calabia, B. P. *Applied Microbiology and Biotechnology* **2006**, *72*, 244.
- (23) Ikada, Y.; Tsuji, H. *Macromolecular Rapid Communications* **2000**, *21*, 117.
- (24) Rzaev, J. *Macromolecules* **2009**, *42*, 2135.
- (25) Olayo-Valles, R.; Lund, M. S.; Leighton, C.; Hillmyer, M. A. *Journal of Materials Chemistry* **2004**, *14*, 2729.

- (26) Zalusky, A. S.; Olayo-Valles, R.; Wolf, J. H.; Hillmyer, M. A. *Journal of the American Chemical Society* **2002**, *124*, 12761.
- (27) Ho, R. M.; Tseng, W. H.; Fan, H. W.; Chiang, Y. W.; Lin, C. C.; Ko, B. T.; Huang, B. H. *Polymer* **2005**, *46*, 9362.
- (28) Nakamura, Y.; Norisuye, T. *Polymer Journal* **2001**, *33*, 874.
- (29) Wintermantel, M.; Gerle, M.; Fischer, K.; Schmidt, M.; Wataoka, I.; Urakawa, H.; Kajiwar, K.; Tsukahara, Y. *Macromolecules* **1996**, *29*, 978.
- (30) Tsukahara, Y.; Namba, S.; Iwasa, J.; Nakano, Y.; Kaeriyama, K.; Takahashi, M. *Macromolecules* **2001**, *34*, 2624.
- (31) Peng, J.; Kim, D. H.; Knoll, W.; Xuan, Y.; Li, B. Y.; Han, Y. C. *Journal of Chemical Physics* **2006**, *125*.
- (32) Logan, J. L.; Masse, P.; Dorvel, B.; Skolnik, A. M.; Sheiko, S. S.; Francis, R.; Taton, D.; Gnanou, Y.; Duran, R. S. *Langmuir* **2005**, *21*, 3424.
- (33) Kubies, D.; Machova, L.; Brynda, E.; Lukas, J.; Rypacek, F. *Journal of Materials Science-Materials in Medicine* **2003**, *14*, 143.
- (34) Fetters, L. J.; Lohse, D. J.; Milner, S. T.; Graessley, W. W. *Macromolecules* **1999**, *32*, 6847.
- (35) Dorgan, J. R.; Janzen, J.; Clayton, M. P.; Hait, S. B.; Knauss, D. M. *Journal of Rheology* **2005**, *49*, 607.
- (36) Numata, K.; Srivastava, R. K.; Finne-Wistrand, A.; Albertsson, A. C.; Doi, Y.; Abe, H. *Biomacromolecules* **2007**, *8*, 3115.
- (37) Souheng, W. *New York : M. Dekker* **1982**.
- (38) Devereaux, C. A.; Baker, S. M. *Macromolecules* **2002**, *35*, 1921.

Chapter 6. Patterning of Conjugated Polymer with Enhanced Photoluminescence via Self-Assembly at the Air/Water Interface

6.1 Introduction

Conjugated polymers (CPs) have received considerable attention as promising materials for use in organic photovoltaics, light-emitting diodes (LEDs), thin film transistors, and biosensors.¹ Among various types of CPs, poly(3-alkylthiophene) (PAT), e.g. P3HT, is one of the most widely studied organic semiconductors due to its excellent solution processability, environmental stability, high charge carrier mobility, and tailorable electrochemical properties.² Currently PAT devices are mainly fabricated by conventional film formation techniques, e.g. drop- or spin-casting, which suffer from a fast and uncontrolled self-assembly process. However, it is of paramount importance to achieve precise control of the assembly process, since electronic and optical properties of solution processed conjugated polymer thin films are intimately connected to the packing motifs of the molecules in the films. The drive towards nanometer scale devices for future electronic applications further emphasizes the need for such nanoscale control.³

Langmuir-Blodgett (LB) techniques are a very useful tool to control the assembly of polymers owing to the asymmetry of the air-water interface. The organization of molecules at the air-water interface can be readily altered as a function of surface pressure, trough temperature, water subphase pH, etc, in contrast to conventional film fabrication methods as drop- or spin-casting.⁴ At this time, the application of the LB technique to conjugated polymers has produced a variety of electrical and optical ultrathin film devices, such as light emitting diodes,⁵⁻¹⁰ thin film conductors,¹¹⁻¹⁵ memory devices,¹⁶ ferroelectric thin films,¹⁷⁻²⁰ nonlinear optical devices,^{21,22} sensors²³⁻²⁷ and field-

effect transistors.^{28,29} Due to strong intermolecular interactions and weak water affinity, however, the stability of PAT monolayers is usually low and thus, they hardly transfer onto the solid substrate. Currently, two main approaches have been developed to resolve those problems: (1) *Spreading a solution of PAT together with inert amphiphilic molecules on water subphase.* The amphiphilic molecules, e.g. e fatty acid, works as lubricant and matrix. After their gradually detachment from water surface, PAT polymer chains came closer to each other and started to align in response to the compression pressure.³⁰ The resulting monolayers were stable and transferrable but had the drawback of giving rise to mixed structures with complete phase separation between the two components. Moreover, defects in films, in the form of either impurities or cavities, are inevitable, and polymer chains are randomly oriented, which is detrimental to their photo-electrical properties. (2) *The molecular structure of polythiophenes can be modified to render them amphiphilic by replacing the alky side chains with polar ones.* Bjørnholm³ et.al recently fabricate the LB film with new designed amphiphilic polythiophenes, which allows the coexistence of a fully conjugated and π -stacked polymer structural motif and a membrane forming motif.

Given the various progress made recently, the PAT chain in current LB works are mainly strongly packed and crystallized, which is important in the application of conductive polymeric films but detrimental to utilization of conjugated polymer as electroluminescent devices, since the strong π - π stacking leads to strong interchain electron transfer, which works as traps and severely quench photoluminescence that originates from the intra-chain electron transfer.³¹ Moreover, many modern applications, including the fabrication of optoelectronic devices and electromagnetic storage media,

demands conjugated polymer patterns that exhibit controlled ordering at different length scales.³² So far, no patterning of conjugated polymer has been achieved by self-assembly process at the air/water interface. *Therefore, it is promising to develop a technique to pattern the PAT with prohibited intra-chain energy transfer.*

Currently, block copolymers occupy a huge area of research since they offer a vast range of possibilities for architecture, size, and chemical composition, due to their selective solvation in solution and microscopic phase separation in the solid state.^{33,34} Numerous LB studies on block copolymer clearly showed that the variation of molecular shapes, architecture of macromolecular backbones and specific intermolecular interactions are very effective way in tailoring air/water interfacial behavior of these materials and thus obtaining the desirable morphology. Limited by the synthesis techniques, the block polymer with conjugated blocks is researched in less intensity with quite few works on the linear block copolymer showing little difference from corresponding homopolymers.³³

For the branched block copolymer, the presence of joints, branches, and a low level of entanglements leads to a greater number of parameters to modify hydrophobic-hydrophilic balance, which enables the controlled self-assembly process and thus well organized LB film.³⁵ Star-like block copolymer is one of the most well studied branched systems which have several linear polymer chains are attached to one compact core. In the work, we design a novel multi-arm star like PtBA-P3HT block copolymer (MSBC) (Figure 1), with P3HT as the conjugated blocks and PtBA as the anchoring block on the water surface. The P3HT was selected because it can easily produce the unique red color that is difficult to achieve with other conjugated polymer.³⁶ An interesting net-like pattern

can be obtained through self-assembly at high surface pressure, and most importantly the intra-chain energy transfer can be effectively prohibited, resulting in highly photoluminescent patterns. The self-assembly process of SBC at air/water was systematically investigated through AFM and TEM, and the possible model has been proposed to illustrate the patterning mechanism as well as energy transfer process. To the best of our knowledge, this is the *first report* on the LB work of branched P3HT based block polymer, and also the *first work* to obtain conjugated polymer patterns with enhanced photoluminescence. As such, it stands out as a promising technique to fabricate micro optoelectronic devices but also provides a platform to investigate the complex self-assembly process and charge transfer of conjugated polymer system confined in 2 dimensions.

6.2 Experimental Section

Chemicals. 2-Bromoisobutyryl bromide (98%), *N,N,N',N'',N''*-pentamethyldiethylene triamine (PMDETA, 99%), anhydrous 1-methyl-2-pyrrolidinone (99.5%), sodium azide ($\geq 99.5\%$), 2,5-dibromo-3-hexyl-thiophene (97%), *tert*-butyl magnesium chloride (2.0 M solution in diethyl ether), [1,3-bis(diphenyl phosphino) propane] dichloronickel(II), ethynyl magnesium bromide (0.5 M solution in tetrahydrofuran) and trifluoroacetic acid (TFA, 99.9%) were purchased from Sigma-Aldrich, and used as received. CuBr (98%, Sigma-Aldrich) was stirred overnight in acetic acid, filtrated, washed with ethanol and diethyl ether successively, and dried in vacuum. β -Cyclodextrine (β -CD, Sigma-Aldrich) was used as received. *tert*-Butyl acrylate (*t*BA, Sigma-Aldrich 98%), methy ethyl ketone (Fisher Scientific, 99.9%) and *N,N*-dimethyl formamide (DMF, Fisher Scientific, 99.9%) were distilled over CaH₂ under reduced

pressure prior to use. Tetrahydrofuran (THF, 99%) was refluxed over potassium wire and distilled from potassium naphthalenide solution. All other reagents were purified by common purification procedures.

Synthesis of Heptakis[2,3,6-tri-O-(2-bromo-2-methylpropionyl)]- β -Cyclodextrin (21Br- β -CD). 21Br- β -CD was synthesized by β -CD with 21 hydroxyl groups esterified by the reaction of end hydroxyl groups with 2-bromoisobutyryl bromide. In a typical process, β -CD (6.82 g, 6 mmol, vacuum dried at 80 °C over calcium oxide overnight immediately before use) was dissolved in 60 mL of anhydrous 1-methyl-2-pyrrolidone (NMP) and was cooled to 0 °C. 2-Bromoisobutyryl bromide (58.0 mL, 252 mmol) was then added dropwise to the β -CD solution with magnetic stirring. The reaction temperature was maintained at 0 °C for 2 h and then allowed to rise slowly to ambient temperature after which the reaction was allowed to continue for 22 h. The brown solution obtained was concentrated in a vacuum oven for 12 h. Then dilute the syrup with 100 mL of dichloromethane, and then wash sequentially with saturated NaHCO₃ aqueous solution (3 \times 200 mL) and DI water (3 \times 200 mL). The organic layer obtained was concentrated in a vacuum oven and then crystallized in cold n-hexane to produce a white precipitate (18.21 g, yield 71.2%). ¹H-NMR (CDCl₃, δ): 1.8-2.2 (126 H, the methyl protons of 21Br- β -CD), 3.5-5.5 (49H, residues of β -CD). FT-IR: 2931 cm⁻¹ ($\square_{\text{C-H}}$), 1737 cm⁻¹ ($\square_{\text{C=O}}$), 1158 cm⁻¹ ($\square_{\text{C-O-C}}$), 1039 and 1105 cm⁻¹ (coupled $\square_{\text{C-C}}$ and $\square_{\text{C-O}}$).

Synthesis of 21-Arm Star-like PtBA with Azide End Group (PtBA-N3). 21-Arm Star-like PtBA with bromine end group (PtBA-Br) was prepared by ATRP of *t*BA in methy ethyl ketone, using 21Br- β -CD with 21 ATRP initiation sites as macroinitiator and CuBr/PMDETA as a catalyst. In a typical process, an ampoule charged with the CuBr

(0.0707 g), PMDETA (0.1707 g), 21Br- β -CD (0.1 g), *t*BA (42.9 mL) and 43 mL of methyl ketone was vacuumed by three freeze-thaw-cycles at the temperature of liquid nitrogen, then sealed and placed in an oil bath at 60 °C for 8h. The ampoules were taken out from the oil bath and dipped in liquid nitrogen to stop the polymerization. The solution was diluted with acetone and passed through a neutral alumina column to remove the catalyst and then precipitated into methanol/water (v/v=1/1). After filtration, the products were purified by dissolution/precipitation twice with acetone and methanol/water and then dried at 40 °C in vacuo for 2 days. Conversion of *t*BA monomer: 19.4%. ¹H-NMR (CDCl₃, δ): 2.56-2.06 (CH₂CH, repeating unit of *Pt*BA), 2.05-1.30 (CH₂CH and -(CO)-OC(CH₃)₃, repeating units of *Pt*BA), 1.21 (-(CO)-C(CH₃)₂).

Then, the precipitate of star-like *Pt*BA with bromine end group (*Pt*BA-Br) (3.60 g) was dissolved in DMF (15 mL), and sodium azide (Br in star-like *Pt*BA : sodium azide= 1:10, molar ratio) was added to the solution. The reaction mixture was stirred 24 h at room temperature. Dichloromethane (25.0 mL) was added into the mixture and washed three times with distilled water. The organic layer was dried with anhydrous MgSO₄, and the solvent was removed by vacuum. Then the product was collected and dried at 40 °C in vacuum oven for 4 h (yield: 95.4%). The number average molecular weight of star-like *Pt*BA-N₃: 120,600 g/mol (based on GPC), 317,940 g/mol (based on ¹H-NMR), 307,210 g/mol (the theoretical value of number average molecular weight calculated from the monomer conversion and concentration of initiators), 14,940 g/mol (number average molecular weight of each arm *Pt*BA calculated from the ¹H-NMR data). PDI of star-like *Pt*BA-N₃: 1.07 (GPC).

$^1\text{H-NMR}$ (CDCl_3 , δ): 1.45 ($-\text{C}(\text{CH}_3)_3$), 1.21 ($-(\text{CO})-\text{C}(\text{CH}_3)_2$), 3.08-3.20 ($\text{CH}_2\text{CH-N}_3$, end group of PtBA). FT-IR: 2112 cm^{-1} ($\square\text{-N}_3$).

Synthesis of Ethynyl-Terminated P3HT (P3HT-ethynyl). Ethynyl-terminated P3HT (P3HT-ethynyl) was synthesized by a quasi-living Grignard metathesis (**GRIM**) **method**. Briefly, 2,5-dibromo-3-hexylthiophene (0.815g, 2.5 mmol) was dissolved in THF (5 mL) in a three-neck flask and stirred under Ar. *Tert*-butylmagnesium chloride (1.25 mL, 2.5 mmol) was added via syringe. The mixture was stirred for 2 h at room temperature. Subsequently, it was diluted to 25 mL with THF and Ni(dppp)Cl_2 (22.5 mg, 0.041 mmol) was added. The resulting mixture was first stirred for 10 min at room temperature, producing intermediate P3HT, followed by reacting with ethynylmagnesium bromide (2mL, 1mmol) in THF for 30 min. The product ethynyl-terminated P3HT (P3HT-ethynyl) was obtained by precipitating the reaction mixture in methanol, filtering in an extraction thimble, and washing by Soxhlet extraction with methanol, hexanes, and chloroform sequentially. The final pure ethynyl-terminated P3HT was recovered after chloroform evaporated. The regioregularity of P3HT was greater than 98% as determined by $^1\text{H-NMR}$. The number average molecular weight and PDI of ethynyl-terminated P3HT were 5100 g/mol (based on $^1\text{H-NMR}$), 4100 g/mol (based on GPC) and 1.18 (GPC), respectively. Yield: 40.8%. $^1\text{H-NMR}$ (CDCl_3 , δ (ppm)): 6.98 (s, 1H), 3.05 (s, 1H), 2.8 (t, $J=3\text{ Hz}$, 2H), 1.7 (m, 2H), 1.43 (m, 2H), 1.36 (m, 4H), and 0.92 (t, 3H). FT-IR: 3296 cm^{-1} ($\nu\equiv\text{C-H}$), 2132 cm^{-1} ($\nu\text{C}\equiv\text{C}$).

Synthesis of 21-Arm Star-like Block Copolymers PtBA-*b*-P3HT by Click Reaction. 21-Arm star-like PtBA with azide end group (PtBA-N_3) and P3HT-ethynyl were dissolved in DMF (10 mL) in a dry ampule. CuBr and PMDETA were added, and

the reaction mixture (P3HT-ethynyl: N₃ in star-like PtBA-N₃: copper bromide: PMDETA = 1.2:1:10:10, molar ratio) was degassed by three freeze-pump-thaw cycles and left under nitrogen. The ampule was immersed in oil bath at 90 °C for 24 h, then taken from the oil bath, and dipped in liquid nitrogen to stop the polymerization. The products were diluted with THF, and solution was passed through alumina column to remove copper salt, precipitated into cold methanol, and dried in vacuum oven at 40 °C for 4 h. The 21-arm star-like block copolymers PtBA-*b*-P3HT was obtained. Yield: 80.9%. Efficiency of click reaction, calculated by ¹H-NMR spectra of the star-like PtBA-*b*-P3HT: 98.6%. The number average molecular weight of star-like diblock copolymer PtBA-*b*-P3HT: 177,800 g/mol (based on GPC), 425,040 g/mol (based on ¹H-NMR). PDI of star-like diblock copolymer PtBA-*b*-P3HT: 1.11 (GPC). ¹H-NMR (CDCl₃, δ): 1.45 (-C(**CH**₃)₃), 1.21 (- (CO)-C(**CH**₃)₂), 6.98 (repeating unit of P3HT), 0.92-2.80 (hexyl group of repeating unit of P3HT)), 7.60-7.41(triazole ring). FT-IR: 1684 cm⁻¹ (stretching band of triazole ring).

Monolayer preparation. The PtBA-P3HT chloroform solutions at the concentration, $c = 6.29 \mu\text{M/L}$ were prepared. Surface pressure - area (π - A) isotherms and polymer monolayers were obtained with R&K Langmuir Blodgett (LB) system (Riegler & Kirstein, GmbH, 160 cm² Teflon trough). The trough was carefully cleaned with 1:1 H₂O₂:NH₃OH solution overnight and subsequently rinsed with DI water (NanoPure, > 18 M Ω cm) for 5 times. A 10 μL toluene solution was gently placed on the water surface to ensure initial gas state. After the solvent evaporated for 30 min, the monolayer film was compressed at a rate of 150 $\mu\text{m/sec}$. Si substrate used for depositing LB films was cleaned with a mixture of sulfuric acid and Nonchromix, followed by

rinsing with DI water and blown dry with N₂. For LB depositions, the Si substrate was withdrawn at a rate of 35 $\mu\text{m}/\text{sec}$ while keeping the pressure constant.

Characterizations. Morphologies of LB films were examined by Atomic Force Microscopy (AFM; Dimension 3000) in the tapping mode. The scanning rate was 2 Hz. Each sample was imaged at more than 5 locations to ensure the reproducibility of features observed. The fine structure was determined by TEM measurements (JEOL 1200EX scanning/transmission electron microscope (STEM); operated at 80 kV). The emission spectra were taken with a Nikon Eclipse TE2000-E microscope coupled with an optical insights hyperspectral unit and a Cascade 512B camera (Roger Scientific). The molecular weight of polymers was measured by GPC, equipped with an Agilent1100 with a G1310A pump, a G1362A refractive detector, and a G1314A variable wavelength detector. THF used as eluent at 35°C at 1.0 mL/min. One 5 μm LP gel column (500 Å, molecular range: $500 - 2 \times 10^4$ g/mol) and two 5 μm LP gel mixed bed columns (molecular range: $200 - 3 \times 10^6$ g/mol) were calibrated with PS standard samples. ¹H-NMR spectra were obtained by a DMX 500 MHz spectrometer. CDCl₃ and d₇-DMF were used as solvents. FTIR spectra were recorded by a Magna-550 Fourier transform infrared spectrometer.

6.3 Results and Discussion

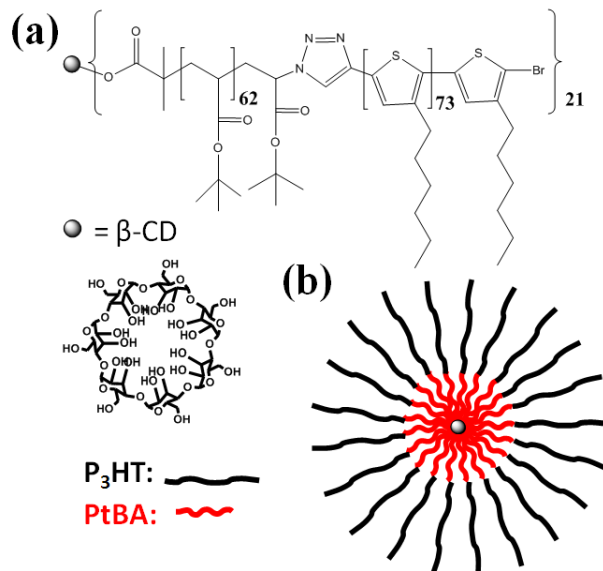


Figure 6-1. (a) Chemical structure and (b) schematic representation of multi-arm PtBA-P3HT block copolymer.

The chemical structure of star like block copolymer is depicted in Figure 6-1a. It can be regarded as 21 PtBA-P3HT linear block copolymer chains attached to one branching point (β -Cyclodextrin), with PtBA block forming the core and P3HT the shell. It has huge molecular weight (425 kg/mol), and large size. The molecule structure of MSBC was built and measured by *Materials Studio*, with PtBA block estimated around 16 nm and the P3HT blocks around 26 nm in length, respectively. The PtBA blocks were selected as anchoring blocks for the following reasons: (1) *Facilitating the morphology transformation*. Given possessing hydrophilic units, enabling its spread on the water surface, PtBA is a hydrophobic polymer in nature, and has much weaker water

affinity (thus the anchoring ability) compared with pure hydrophilic blocks, e.g. PEO, PAA.^{37,38} Therefore, the phase transfer of the monolayer becomes much easier in response to surface pressure, an paramount advantage to manipulate the patterning process. (2) *Prohibiting the crystalization of P3HT*. Due to the its hydrophobic nature, the PtBA forms monolayer on water surface,³⁹ blocking the direct contact between hydrophobic P3HT blocks and polar water subphase and therefore reducing the drive force for P3HT to stacking.

Morphology evolution under surface pressure

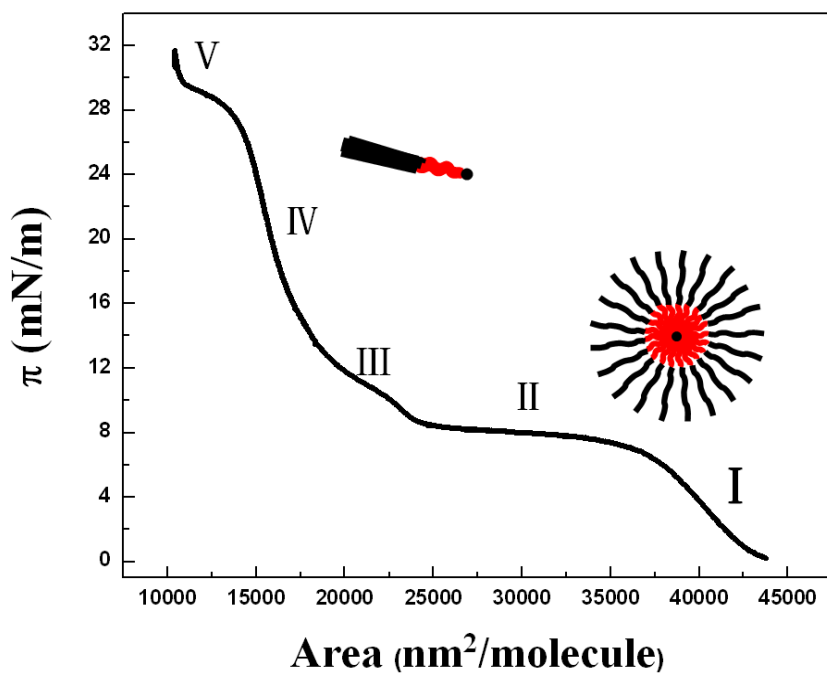


Figure 6-2. Pressure -area isotherms of multi-arm PtBA-P3HT block copolymer: (I) liquid region, (II) plateau region, (III) sub-condensed region, (IV) condensed region,(V) post condensed region. Insertion shows the illustration of molecular architecture at gas state (right) and condensed state (left).

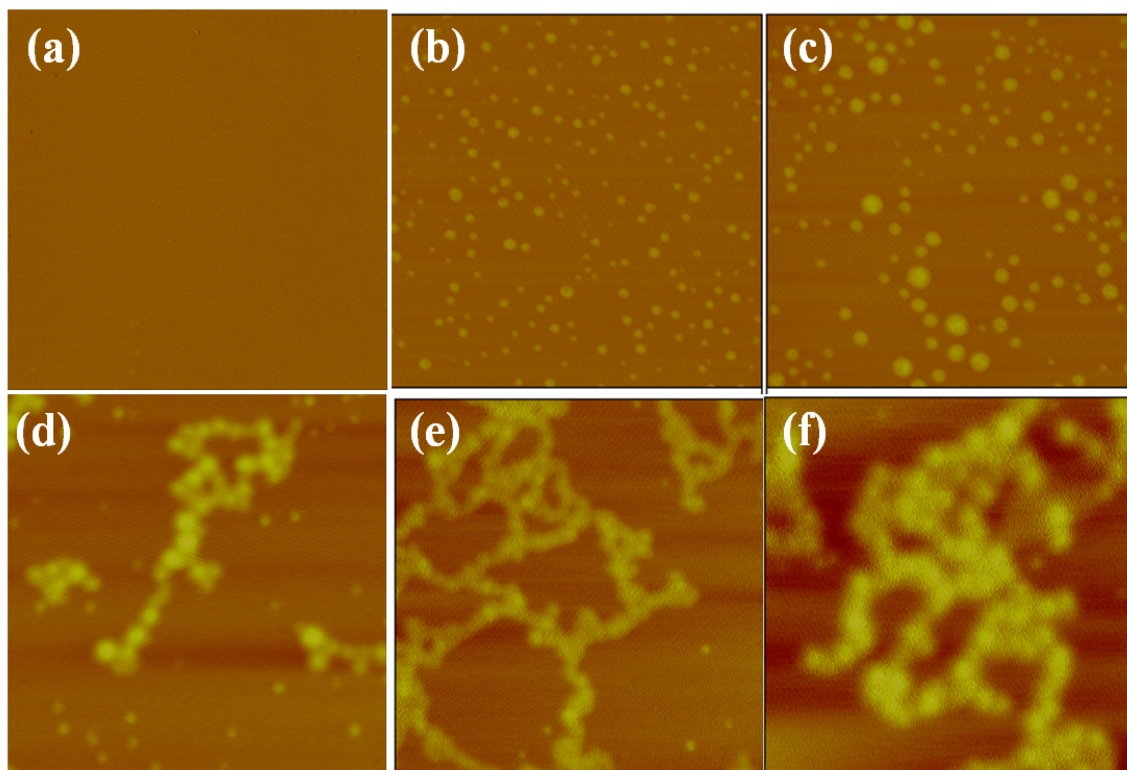


Figure 6-3. AFM height images of the MSBC Langmuir monolayers obtained from the chloroform solution at various transfer pressure: (a) gas region; (b) liquid region; (c) plateau region; (d) sub-condensed region; (e) condensed region; (f) post condensed region. Scan size = $5\ \mu\text{m} \times 5\ \mu\text{m}$ and z scale = 100 nm for all images

Langmuir isotherm, i.e., surface pressure- area (π -A) plot, of the PtBA-P3HT star-like block polymer is shown in Figure 6-2. The continuous pressure rise was indicative of the formation of LB monolayer. In contrast to the previous hydrophobic block copolymers, which usually exhibited featureless curves,⁴⁰ multiple plateau regions can be clearly observed in the isotherm, indicating more complex phase transitions process in response to the surface pressure. Therefore, besides the gas state, the entire isotherm can be divided into five regions; they were (I) liquid state, (II), plateau region at $\pi =$

7mN/m, (III) sub-condensed region at $\pi = 9$ mN/m, (IV) condensed state, (IV) post-condensed region. Representative AFM height images of LB monolayer obtained at those regions are shown in Figure 6-3.

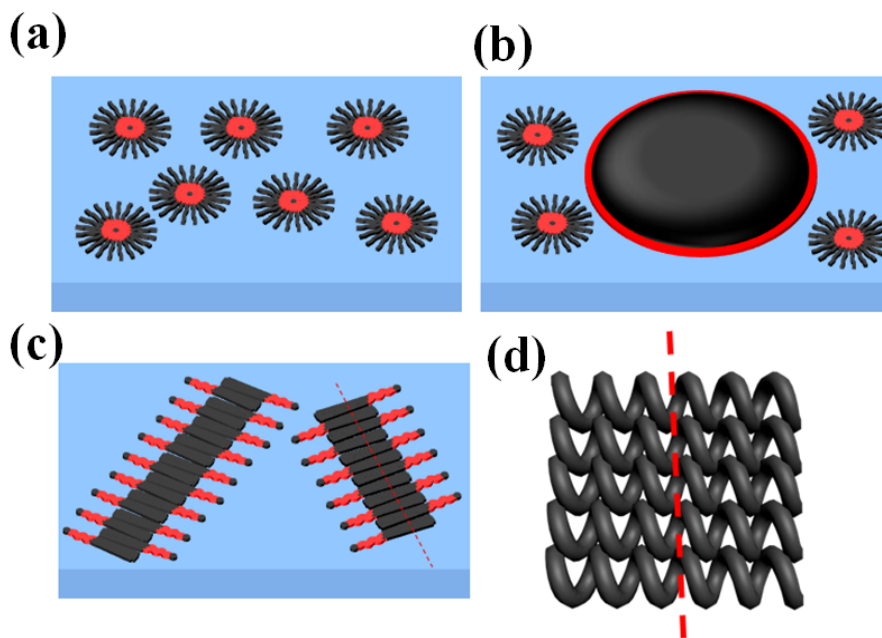


Figure 6-4. Schematic illustration of the packing of microstructures at different surface pressures. (a) gas region where multi-arm molecules are fully spread; (b) liquid and plateau plateau region, (c) condensed state region, as well as possible P3HT packing (d) in this region. Red dot line represents the axis of nano-fiber.

In the absence of surface pressure (gas state), the whole molecule are highly dispersed without interaction on water surface, resulting in a featureless surface morphology as characterized by both AFM and TEM images (Figure 6-3a). Due to existence of polar groups on both two blocks,⁴¹ both PtBA and P3HT blocks have certain water affinity, enabling them attach to the water surface forming monolayer. This is consistent with the previous report on PtBA and P3HT homopolymers.^{30,37,38} Considering the highly branched molecular architecture and rigidity of P3HT backbone, each

molecules may fully spread and assume star like morphology (Figure 6-2 right-insertion and Figure 6-4a).

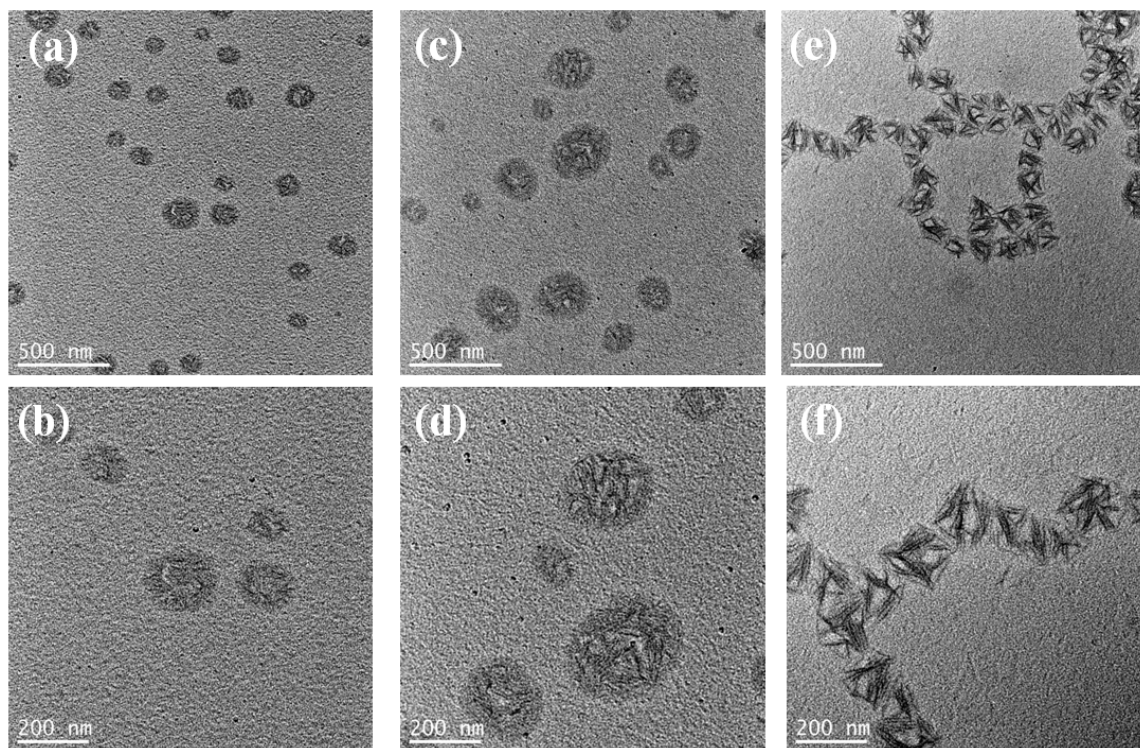


Figure 6-5. TEM images of LB monolayer deposited from (a),(b) liquid region; (c),(d) plateau region; (e),(f) condensed region.

In contrast to PtBA blocks, which have stronger water affinity due to formation of hydrogen bond between the ester group and water molecules,⁴² P3HT is less stable and detached from water surface easily under gentle surface pressure, thus forming circular aggregation in the liquid region (Figure 6-3b). The PtBA blocks, on the other hand, still spread on the water subphase, anchoring the MSBC on the water surface. This can be confirmed by the TEM measurement. Due to its highly localized electron density compared with that of PtBA,⁴³ P3HT aggregates can be directly imaged by TEM without

staining, while the PAA phase is totally transparent to electron beam giving no contrast in the final images. Therefore, all the morphological features in TEM images originate solely from P3HT phases. It clearly shows the circular domain is composited of amorphous P3HT blocks, with size consistent with corresponding AFM images (Figure 6-5a,b). As consequence, in this region, it is safe to assume a “pancake” model with P3HT aggregating on the top of continuous PtBA monolayer (Figure 6-4b).^{40,42} The remanent spreaded molecules, on the other hand, fill the space between circular domains, transferring surface pressure among LB monolayer (Figure 6-4b).

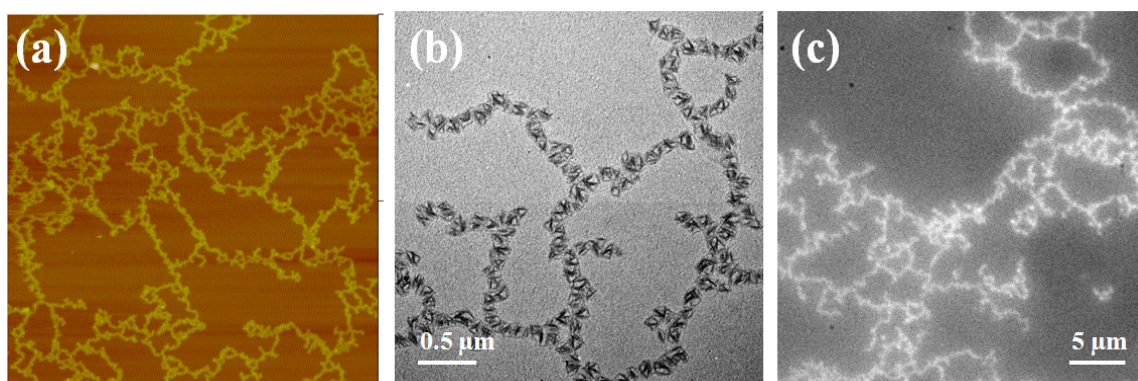


Figure 6-6. (a)AFM height image, (b) TEM image, and (c) fluorescent image of MSBC pattern deposited at condensed region. Scan size = $20\ \mu\text{m} \times 20\ \mu\text{m}$ and z scale = 100 nm for AFM images.

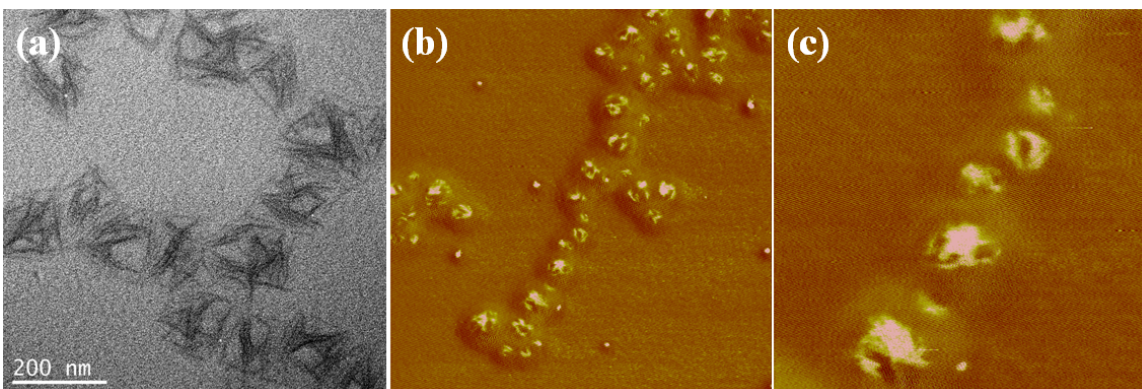


Figure 6-7. (a) Close up TEM image of MSBC network deposited at condensed region, as well as its AFM phase images at different magnification (b) size = $3\ \mu\text{m} \times 3\ \mu\text{m}$ and phase scale = 50° and (C) size = $3\ \mu\text{m} \times 3\ \mu\text{m}$ and phase scale = 30° .

With further pressure increase, more spread P3HT are detached and join the existing circular domain, enlarging its size obviously in plateau region (Figure 6-3c). It is confirmed by TEM measurement by showing similar morphology with only increased size (Figure 6-5c,d). Moreover, the AFM phase images clearly show that the circular domain is even and only composed of single phases. The long plateau region can be attributed to phase transition of PtBA during which the tert-butyl side groups reorientate from a prone to vertical position,⁴⁴ leading to collapse of PtBA blocks layer. Due to its hydrophobic nature, PtBA blocks collapse by aggregating on top of the water surface, instead of dissolving into water subphase. Consequently, the surface area decreases dramatically while surface pressure remain constant, forming the long plateau region.³⁸ At the end of plateau (sub-condensed region), the previous circular domains are pushed close and undergo chaining process, resulting in a short plateau region (Figure 6-3c). Finally, in the condensed region, a novel network structure was observed as result of the domain chaining (Figure 6-3e and Figure 6-6a). The network is found continuous and fully cover the substrate. Close TEM images of the network clearly shows that each units on the chain is no longer the circular and even P3HT amorphous domains. Instead, it assumes a semi-rectangular shape, with a hole surrounded by P3HT fibers forming periphery as observed in the AFM images (Figure 6-5e,f). Those fibers tend to parallel each at the conjunction of neighboring units. The existence of hole can be readily observed through close up TEM image (Figure 6-7a), but also be identified by AFM phase images showing contrast phase differences between central and periphery region (Figure 6-7 b.c). Considering the relative size of PtBA to P3HT phases, the hole region can hardly be attributed to PtBA phase, and should be empty region.

By far, network like morphologies were mainly reported at zero surface pressure from amphiphilic polymers, where dewetting process of polymeric solution on water surface leads to their formation. To best of our knowledge, this is first observation of self-assembly of isotropic circular surface micelle into network structure through lateral compression. Therefore, a new model has been proposed to illustrate this complex self-assembly process, which will be discussed in the later section. Moreover, in contrast with previous conjugated polymer film made by LB techniques other deposition approaches,^{4,45} where strong inter-chain energy transfer within condensed phases severely quench luminescence, the PL emission from network is so strong that single monolayer can be directly observed under conventional optical microscope via the excitation of wide green lamp (Figure 6-6c). Given numerous work on LB work of conjugated polymer, this is first report on directly observation of single conjugated monolayer through optical microscope. The detailed mechanism will be illustrated in next section.

After formation of perfect network, further lateral compression upon monolayer leads to its condensation and finally breaking down (Figure 6-3f), leading to isotropic arrangement of P3HT domains into island like morphology. During this process, the empty space between the networks was gradually filled, therefore a small plateau can be well observed at post condensed region. After condensed compacted, the monolayer is no longer compressible, therefore a dramatic pressure increase is shown at the end of isotherm, followed by sudden pressure drop indicating the collapse of monolayer.

Enhanced photoluminescence emission of MSBC pattern.

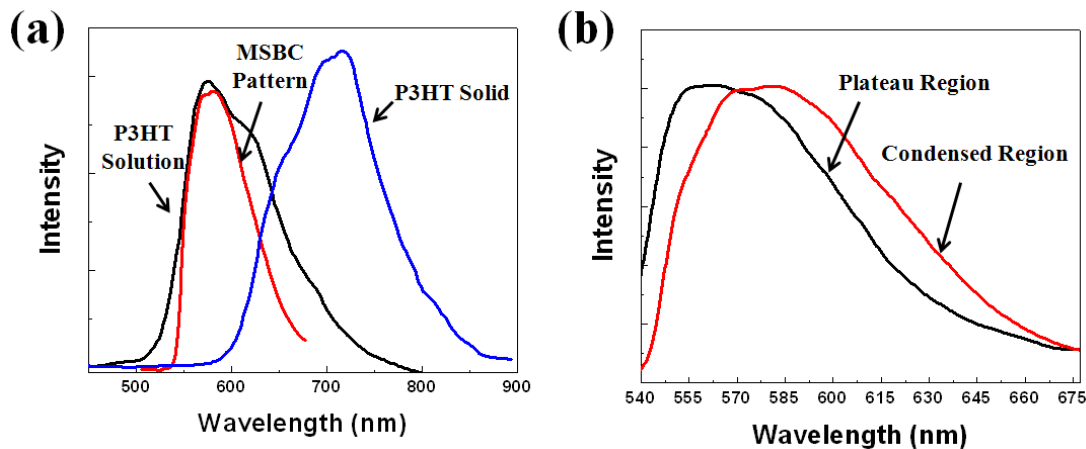


Figure 6-8. Photoluminescence spectra of (a) MSBC patterns, P3HT homopolymer in solution and solid state; (b) MSBC monolayer at the liquid region and condensed region.

The achievement of conjugated polymer film or patterns with high PL efficiency are crucial to fabrication of nano-size electroluminescent devices. In order to reveal the origin of their strong PL emission, the MSBC network was characterized with PL spectra, with P3HT homopolymer (identical to each P3HT blocks) in solution and solid state both measured as reference. The vibronic structures of P3HT are clearly evident (i.e., 0-0 emission peak at 574 nm and 0-1 emission peak at 620 nm for solution state; and 0-0 emission peak at 655 nm and 0-1 emission peak at 715 nm for solid state).⁴⁶ Electronic structure and optical properties of P3HT has been intensely researched in the past decades,^{1,36,47} and two basic types of emission have been identified: intramolecular emission and interchain emission. The 0-0 emission is broadly attributed to the intramolecular exciton, while 0-1 emission is shown strongly related to interchain interaction.^{48,49} In solution state, the conjugated chain is broken into conformational subunits consisting several repeat units long owing to the relatively low energy barrier for

small-angle rotations around bonds along the backbone. Therefore the emission is blue-shifted due to the reduced conjugated length.⁵⁰ After drying out (Figure 6-8), the aggregation of P3HT chain, e.g. crystallization, greatly increase the ordering of polymeric chain and degree of interchain interaction, leading to increased conjugated length (e.g. red-shift) and enhanced 0-1 peak intensity relative to the 0-0 peak, respectively.^{48,49} As reported by Saadeh et.al,⁵¹ the PL efficiency dramatically drops from 30-40% to 1-4% during this process due to increased contribution of non-radiative decay via interchain interactions. In order to preserve high luminescence efficiency observed in solution state, the conjugated polymer are usually incorporated into an inert solid matrix, which often suffers from phase separation or low CP concentration.³⁶

In great contrast to P3HT solid materials, the LB pattern of MSBC shows the identical 0-0 emission position as coiled P3HT chains in solution, clearly indicating the successful transferring of this highly PL efficient disordered state into solids. Moreover, the 0-1 emission (interchain) peak relative to 0-0 emission is also dramatically reduced, even negligible, a clear evidence of prohibited interchain energy transfer in MSBC pattern. Therefore, the PL efficiency of MSBC pattern was great enhanced due to reduced PL quenching traps,³¹ and the high PL emission can be directly observed from OM. To best of our knowledge, this is first work to direct transfer disordered conjugated polymer chain from solution into solid state, a technique paramount important to fabricate high efficient electroluminescent devices. Moreover, it is interesting to notice that the emission position can also be readily modified through surface pressure. As shown in figure 6-8b, the emission is blue shift to the around 550 nm from 585 nm when in the

amorphous state (plateau region). It shows that, in the fiber like state, the P3HT backbone is more rigid, resulting in increased the conjugated length.

Self-assembly Mechanism for MSBC pattern Formation

Obviously, the formation of network is triggered by the detachment of PtBA blocks from water surface, as the chaining process occurs only after the plateau region. As shown in the first section, circular amorphous P3HT domains, assuming a pancake structure with P3HT aggregating on the top of continuous PtBA monolayer, was converted into those composed of fiber-like components. By far, the fiber like morphology in nano-size has seldom been reported in the LB work of conjugated polymer, only wire structure reported after collapse of amphiphilic polythiophenes monolayer.⁵² The fiber like morphology has been broadly observed in the crystallized state of conjugated rod-coil block copolymer, which self-assembled head-to-tail or head-to-head into various structures, like nematic, smectic, hockey pucks, etc.^{53,54} In each case, the width of fiber is no shorter than the chain length of conjugated blocks due to the stacking.⁵⁴ However, the width of fiber in the SBC pattern is estimated around 9 nm from TEM image (Figure 6-7a), much shorter than the chain length of P3HT block (26 nm, calculated from Materials Studio). Considering the prohibited interchain emission observed in the PL spectra, it is safe to draw the conclusion that the fiber is not formed by the crystallization of P3HT blocks as broadly reported previously.^{43,55}

P3HT possesses a molecular architecture similar to amphiphilic graft copolymer, hydrophobic alkyl side chains grafted onto hydrophilic polythiophene backbone. In the organic solvent (chloroform here), selective for side groups chains, the P3HT molecules easily fold back on themselves into helical like conformation with syn configuration of

thiophene units in which all sulfur atoms are directed inside the cavity and hydrocarbon groups are oriented outside the helix.⁵⁶⁻⁵⁸ By the slow drying, some of such helix-like P3HT chain can be preserved into solid state, which appears like rigid rod under TEM images.⁵⁸ After spread on the water surface, the unpleasant interaction between polar water and hydrophobic alkyl side drive the crystallization of P3HT homopolymer to reduce the overall free energy. As the MSBC monolayer, the existence of continuous hydrophobic PtBA layer may effectively block the direct contact between the P3HT phase and water surface, greatly reducing such drive force. Consequently, the disordered helix-like molecular configuration may also be well preserved into MSBC pattern, and alkyl side chain oriented outside the helix effectively block the inter-chain energy transfer between neighboring conjugated backbones. It is consistent with prohibited 0-1 emission in the PL spectra measurement (Figure 6-8).

After the plateau region, the PtBA are no longer able to anchor whole molecules on the water surface due to its detachment, therefore the multi-arm may easily folded into rigid-coil like molecular architecture (Figure 6-2 left-insertion), with P3HT blocks within single molecule forming the rigid part and PtBA blocks the flexible ones (Figure 6-2).⁵⁹ Recently, the self-assembly process has been systematically investigated for rigid-coil comb-like block copolymer which forms the similar elongated surface micelle at the air/water interface. Due to the similar structure of P3HT to amphiphilic graft copolymer, the rigid P3HT blocks may also assemble side by side with adjacent molecules along the axial direction of fiber, with flexible PtBA blocks forming corona to keep neighboring fiber apart (Figure 6-4c). Since each P3HT block chain exists in the helix-like morphology perpendicular to fiber axis (Figure 6-4d), the width of fiber is thus

much shorter than of crystallized state, where the P3HT chain are completely stretch out in a planar achitecture.⁴³ Compared with the disordered amorphous state (e.g. liquid region), the backbone of P3HT in this state is more rigid, resulting in the red shift of PL emission as shown in figure 6-8b.

The anisotropic assembly of individuals with isotropic interaction has been observed frequently in nature, like molecules,^{60,61} surface micelles,⁶² colloidal particles,⁶³ etc. It is generally attributed to the competition between short-range attractive forces and long-range repulsion between them.⁶³ For example, Boerner et.al recently reported the chaining of brush macromolecule with PBA-b-PS grafts on solid substrate. The chaining in the block copolymer brushes was suggested resulting from the attraction of desorbed PS blocks and repulsion between the adsorbed PBA blocks.⁶⁰ However, to our best knowledge, no network like morphology has been reported assembled from isotropic units, so far. To forming the network like morphology, the chaining and branching assembly should occurs spontaneously, with chaining assembly having more probability. Similar to brush macromolecules,⁶³ the chaining of MSBC domain should also originate from the balance between short-range attractive and long-range repulsive forces. Here, the attractive force originates from hydrophobic P3HT fibers when they are pushed close enough. The attractive force can be maximized when P3HT fiber parallel each other in conjunction region (Figure 6-7a). On the other hand, the PtBA layer generates this long range repulsive force resulted from its affinity with water.⁴² However, due to the limited size of PtBA block compared with whole domains, the repulsive force may be not strong enough, resulting in brushing assembly in certain probability. Therefore, a network like morphology can be formed under these tow process. The systematically dynamics

process is explored by Molecular Dynamics simulation, and will be discussed in the later work.

6.4 Conclusions

In summary, we synthesized a novel multi-arm conjugated polymer based block copolymer, multi-arm PtBA-P3HT, and systematically studied the their air/water interfacial behavior. Such polymers can be found readily patterned into network structure with well enhanced photoluminescence efficiency. The branched architecture and existence of amphiphilic PtBA blocks are found effective to preserve highly efficient disordered conjugated polymer chain from solution into solid state. The helix molecular architecture furthermore effectively block the inter-chain energy transfer, contributing to the high efficiency. The influence of surface pressure on assembly behavior of MSBC Langmuir monolayer at the air/water interface was also explored with both AFM and TEM. At low pressure, the molecules forms the surface micelles, assuming a pancake like structure with aggregated P3HT on continuous PtBA monolayer. After the detachment of PtBA block at high pressure, the branched structure can fold into rigid-coil like architecture, resulting in the anisotropic self-assembly process forming the fiber like morphology. The chaining process of domain can be attributed to the balance of attraction of desorbed PS blocks and repulsion between the adsorbed PBA blocks. As such, it not only complements the basic knowledge of self-assembly of conjugated polymer at the air/water interface, but also provides an efficient approach to pattern conjugated polymer and to modify the their photophysical in the solid state.

References:

- (1) Schwartz, B. J. *Annu. Rev. Phys. Chem.* **2003**, *54*, 141.
- (2) He, M.; Zhao, L.; Wang, J.; Han, W.; Yang, Y. L.; Qiu, F.; Lin, Z. Q. *ACS Nano* **2010**, *4*, 3241
- (3) Reitzel, N.; Greve, D. R.; Kjaer, K.; Hows, P. B.; Jayaraman, M.; Savoy, S.; McCullough, R. D.; McDevitt, J. T.; Bjornholm, T. *J. Am. Chem. Soc.* **2000**, *122*, 5788.
- (4) Park, J. Y.; Koenen, N.; Forster, M.; Ponnampati, R.; Scherf, U.; Advincula, R. *Macromolecules* **2008**, *41*, 6169.
- (5) Chen, T. A.; Wu, X. M.; Rieke, R. D. *J. Am. Chem. Soc.* **1995**, *117*, 233.
- (6) Wu, A. P.; Akagi, T.; Jikei, M.; Kakimoto, M.; Imai, Y.; Ukishima, S.; Takahashi, Y. *Thin Solid Films* **1996**, *273*, 214.
- (7) Cimrova, V.; Remmers, M.; Neher, D.; Wegner, G. *Adv. Mater.* **1996**, *8*, 146.
- (8) Pal, A. J.; Ostergard, T.; Paloheimo, J.; Stubb, H. *Appl. Phys. Lett.* **1996**, *69*, 1137.
- (9) Ostergard, T.; Paloheimo, J.; Pal, A. J.; Stubb, H. *Synth. Met.* **1997**, *88*, 171.
- (10) DonatBouillud, A.; Mazerolle, L.; Leclerc, M. *Synth. Met.* **1997**, *84*, 235.
- (11) Ando, M.; Watanabe, Y.; Iyoda, T.; Honda, K.; Shimidzu, T. *Thin Solid Films* **1989**, *179*, 225.

- (12) Rikukawa, M.; Nakagawa, M.; Abe, H.; Ishida, K.; Sanui, K.; Ogata, N. *Thin Solid Films* **1996**, 273, 240.
- (13) Park, Y. H.; Park, S. Y.; Nam, S. W.; Park, C. R.; Kim, Y. J. *J. Appl. Polym. Sci.* **1996**, 60, 865.
- (14) Granholm, P.; Paloheimo, J.; Stubb, H. *Synth. Met.* **1997**, 84, 783.
- (15) Paddeu, S.; Ram, M. K.; Nicolini, C. *J. Phys. Chem. B* **1997**, 101, 4759.
- (16) Takimoto, K.; Kuroda, R.; Shido, S.; Yasuda, S.; Matsuda, H.; Eguchi, K.; Nakagiri, T. *J. Vac. Sci. Technol., A* **1997**, 15, 1429.
- (17) Palto, S.; Blinov, L.; Bune, A.; Dubovik, E.; Fridkin, V.; Petukhova, N.; Verkhovskaya, K.; Yudin, S. *Ferroelectr. Lett.* **1995**, 19, 65.
- (18) Xue, Q. B.; Chen, X.; Yang, K. Z.; Zhang, Q. Z. *J. Macromol. Sci., Rev.* **1995**, 196, 3243.
- (19) Blinov, L. M.; Fridkin, V. M.; Palto, S. P.; Sorokin, A. V.; Yudin, S. G. *Thin Solid Films* **1996**, 285, 474.
- (20) Asadi, K.; De Leeuw, D. M.; De Boer, B.; Blom, P. W. M. *Nat. Mater.* **2008**, 7, 547.
- (21) Wijekoon, W. M. K. P.; Wijaya, S. K.; Bhawalkar, J. D.; Prasad, P. N.; Penner, T. L.; Armstrong, N. J.; Ezenyilimba, M. C.; Williams, D. J. *J. Am. Chem. Soc.* **1996**, 118, 4480.
- (22) Jung, C.; Jikei, M.; Kakimoto, M. *J. Opt. Soc. Am. B: Opt. Phys.* **1998**, 15, 471.
- (23) Schoning, M. J.; Sauke, M.; Steffen, A.; Marso, M.; Kordos, P.; Luth, H.; Kauffmann, F.; Erbach, R.; Hoffmann, B. *Sens. Actuators, B* **1995**, 27, 325.

- (24) Agbor, N. E.; Petty, M. C.; Monkman, A. P. *Sens. Actuators, B* **1995**, 28, 173.
- (25) Milella, E.; Musio, F.; Alba, M. B. *Thin Solid Films* **1996**, 285, 908.
- (26) Lavrik, N. V.; DeRossi, D.; Kazantseva, Z. I.; Nabok, A. V.; Nesterenko, B. A.; Piletsky, S. A.; Kalchenko, V. I.; Shivaniuk, A. N.; Markovskiy, L. N. *Nanotechnology* **1996**, 7, 315.
- (27) Ng, S. C.; Zhou, X. C.; Chen, Z. K.; Miao, P.; Chan, H. S. O.; Li, S. F. Y.; Fu, P. *Langmuir* **1998**, 14, 1748.
- (28) Paloheimo, J.; Kuivalainen, P.; Stubb, H.; Vuorimaa, E.; Ylilahti, P. *Appl. Phys. Lett.* **1990**, 56, 1157.
- (29) Paloheimo, J.; Stubb, H.; Ylilahti, P.; Dyreklev, P.; Inganas, O. *Thin Solid Films* **1992**, 210, 283.
- (30) Xu, G. F.; Bao, Z. A.; Groves, J. T. *Langmuir* **2000**, 16, 1834.
- (31) Spano, F. C. *J. Chem. Phys.* **2005**, 122.
- (32) Kim, J. S.; McHugh, S. K.; Swager, T. M. *Macromolecules* **1999**, 32, 1500.
- (33) Lynd, N. A.; Meuler, A. J.; Hillmyer, M. A. *Prog. Polym. Sci.* **2008**, 33, 875.
- (34) Ruzette, A. V.; Leibler, L. *Nat. Mater.* **2005**, 4, 19.
- (35) Ornatska, M.; Bergman, K. N.; Goodman, M.; Peleshanko, S.; Shevchenko, V. V.; Tsukruk, V. V. *Polymer* **2006**, 47, 8137.
- (36) Perepichka, I. F.; Perepichka, D. F.; Meng, H.; Wudl, F. *Adv. Mater.* **2005**, 17, 2281.

- (37) Choi, I.; Gunawidjaja, R.; Suntivich, R.; Tsitsilianis, C.; Tsukruk, V. V. *Macromolecules* **2010**, *43*, 6818.
- (38) Joncheray, T. J.; Bernard, S. A.; Matmour, R.; Lepoittevin, B.; El-Khoury, R. J.; Taton, D.; Gnanou, Y.; Duran, R. S. *Langmuir* **2007**, *23*, 2531.
- (39) Mengel, C.; Esker, A. R.; Meyer, W. H.; Wegner, G. *Langmuir* **2002**, *18*, 6365.
- (40) Zhao, L.; Byun, M.; Rzayev, J.; Lin, Z. Q. *Macromolecules* **2009**, *42*, 9027.
- (41) Leclere, P.; Hennebicq, E.; Calderone, A.; Brocorens, P.; Grimsdale, A. C.; Mullen, K.; Bredas, J. L.; Lazzaroni, R. *Prog. Polym. Sci.* **2003**, *28*, 55.
- (42) Zhao, L.; Goodman, M. D.; Bowden, N. B.; Lin, Z. Q. *Soft Mater.* **2009**, *5*, 4698.
- (43) Wang, H. B.; You, W.; Jiang, P.; Yu, L. P.; Wang, H. H. *Chem. Eur. J.* **2004**, *10*, 986.
- (44) Taniguchi, T.; Yokoyama, Y.; Miyashita, T. *Macromolecules* **1997**, *30*, 3646.
- (45) Bolognesi, A.; Bajo, G.; Paloheimo, J.; Ostergard, T.; Stubb, H. *Adv. Mater.* **1997**, *9*, 121.
- (46) Xu, J.; Wang, J.; Mitchell, M.; Mukherjee, P.; Jeffries-EL, M.; Petrich, J. W.; Lin, Z. Q. *J. Am. Chem. Soc.* **2007**, *129*, 12828.
- (47) Bredas, J. L.; Cornil, J.; Beljonne, D.; dos Santos, D.; Shuai, Z. G. *Acc. Chem. Res.* **1999**, *32*, 267.

- (48) Ruseckas, A.; Namdas, E. B.; Ganguly, T.; Theander, M.; Svensson, M.; Andersson, M. R.; Inganas, O.; Sundstrom, V. *J. Phys. Chem. B* **2001**, *105*, 7624.
- (49) Nguyen, T. Q.; Doan, V.; Schwartz, B. J. *J. Chem. Phys.* **1999**, *110*, 4068.
- (50) Collini, E.; Scholes, G. D. *Science* **2009**, *323*, 369.
- (51) Saadeh, H.; Goodson, T.; Yu, L. P. *Macromolecules* **1997**, *30*, 4608.
- (52) Bjornholm, T.; Hassenkam, T.; Greve, D. R.; McCullough, R. D.; Jayaraman, M.; Savoy, S. M.; Jones, C. E.; McDevitt, J. T. *Adv. Mater.* **1999**, *11*, 1218.
- (53) de Cuendias, A.; Hiorns, R. C.; Cloutet, E.; Vignau, L.; Cramail, H. *Polym. Int.* **2010**, *59*, 1452.
- (54) Hoeben, F. J. M.; Jonkheijm, P.; Meijer, E. W.; Schenning, A. P. H. J. *Chem. Rev.* **2005**, *105*, 1491.
- (55) Lee, M.; Cho, B. K.; Zin, W. C. *Chem. Rev.* **2001**, *101*, 3869.
- (56) Cui, C. X.; Kertesz, M. *Phys. Rev. B* **1989**, *40*, 9661.
- (57) Williams, D. R. M.; Fredrickson, G. H. *Macromolecules* **1992**, *25*, 3561.
- (58) Kiriya, N.; Jahne, E.; Adler, H. J.; Schneider, M.; Kiriya, A.; Gorodyska, G.; Minko, S.; Jehnichen, D.; Simon, P.; Fokin, A. A.; Stamm, M. *Nano Lett.* **2003**, *3*, 707.
- (59) Genson, K. L.; Hoffman, J.; Teng, J.; Zubarev, E. R.; Vaknin, D.; Tsukruk, V. V. *Langmuir* **2004**, *20*, 9044.
- (60) Borner, H. G.; Beers, K.; Matyjaszewski, K.; Sheiko, S. S.; Moller, M. *Macromolecules* **2001**, *34*, 4375.
- (61) Dobrynin, A. V.; Rubinstein, M. *Macromolecules* **2000**, *33*, 8097.
- (62) Logan, J. L.; Masse, P.; Dorvel, B.; Skolnik, A. M.; Sheiko, S. S.; Francis, R.; Taton, D.; Gnanou, Y.; Duran, R. S. *Langmuir* **2005**, *21*, 3424.

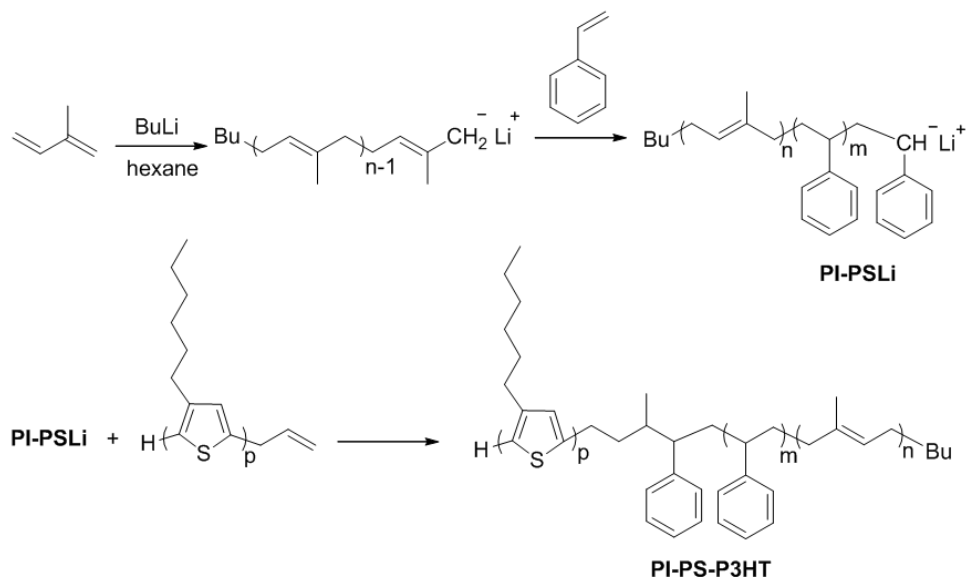
- (63) Malescio, G.; Pellicane, G. *Nat. Mater.* **2003**, 2, 97.

Chapter 7. Patterning of Hydrophobic Conjugated Copolymer with Enhanced photoluminescence via Dewetting at the Air/Water Interface

7.1 Introduction:

In the previous reports on the LB work of conjugated polymers, the existence of hydrophilic components, either like second amphiphilic phase (approach 1) or polar units (approach 2), are believed necessary to stabilize P3AT monolayer, but confining the application of LB techniques only to amphiphilic systems. In this work, we discover, for the first time, the addition of hydrophobic blocks (i.e. PI and PS) to the conjugated polymer P3HT can also stabilize the LB monolayer either, greatly extending the range of LB techniques utilization in P3AT devices. Here, the P3HT was selected because it can easily produce the unique red color that is difficult to achieve with other conjugated polymer.¹ An interesting pattern was observed through dewetting process, and most importantly, the undesirable inter-chain energy transfer can be effectively prohibited due to successful transferring of the high-PL efficient disordered state from solution into solid monolayer, resulting in highly photoluminescent patterns. The self-assembly process of PI-PS-P3HT triblock copolymer at air/water was systematically investigated through AFM and TEM, and the possible model has been proposed to illustrate the patterning mechanism as well as energy transfer process. To best of knowledge, this is the *first report* on the LB work of hydrophobic conjugated polymer, and also the *first work* to obtain conjugated polymer pattern with enhanced photoluminescence through dewetting process. As such, it stands out as a promising technique to fabricate micro optoelectronic devices but also provides a platform to investigate the complex self-assembly process and charge transfer of conjugated polymer system confined in 2 dimensions.

7.2 Experimental Section



Scheme 7-1. Synthesis of polyisoprene-*b*-polystyrene-*b*-poly(3-hexylthiophene) by coupling of living polyisoprene-*b*-polystyryl lithium with allyl-terminated regioregular poly(3-hexylthiophene)

Materials synthesis.

All reactions were conducted under prepurified nitrogen, using oven-dried glassware. Commercial chemicals, purchased from Aldrich Chemical Co., Inc., were used without further purification unless otherwise noted. All solvents were freshly distilled prior to use. Tetrahydrofuran was distilled from sodium benzophenone ketyl. Chloroform was distilled and collected over molecular sieves. Polyisoprene-*b*-polystyrene-*b*-poly(3-hexylthiophene) triblock copolymer was synthesized by addition of living polyisoprene-*b*-polystyryl lithium to the allyl terminated poly(3-hexylthiophene) as shown in Scheme 7-1. A similar procedure was used for the synthesis of polystyrene-*b*-poly(3-hexylthiophene) diblock copolymer.² Addition of allyl magnesium bromide to the

GRIM polymerization generated a polymer with bromine and allyl end-groups. Prior to the anionic coupling reaction the bromine end-group was reduced by magnesium halogen exchange to generate H/allyl polymer. This step was included to avoid a possible side reaction of lithium bromine exchange during the coupling process. Allyl-terminated poly(3-hexylthiophene) was synthesized according to previously published procedure.² The polyisoprene-*b*-polystyrene segment was prepared by *living* anionic polymerization in moisture and oxygen free cyclohexane, according to the previously described method.^{3,4}

Allyl-terminated poly(3-hexylthiophene): ¹H NMR (500 MHz, CDCl₃): δ_H 0.9 (t, 3H), 1.35-1.43 (m, 6H), 1.69 (t, 2H), 2.80 (t, 2H), 3.49 (d, 2H), 5.11 (m, 2H), 5.98 (m, 1H) 6.95 (s, 1H), DP_n=20; SEC: M_n=4500 g/mol; PDI = 1.25.

Polyisoprene-*b*-polystyrene: ¹H NMR (500 MHz, CDCl₃): δ_H 1.4 (bs, *J* = 7 Hz, 3H), 1.53 (s, 3H), 1.61 (s, 3H), 1.67 (s, 3H), 2.0 (m, 2H) 4.7 (m, 1H), 5.1 (m, 1H), 6.5 (m, 2H) 7.1 (m, 3H), SEC: M_n=3700 g/mol; PDI = 1.20.

Coupling of living polystyryl lithium with allyl-terminated P3HT:

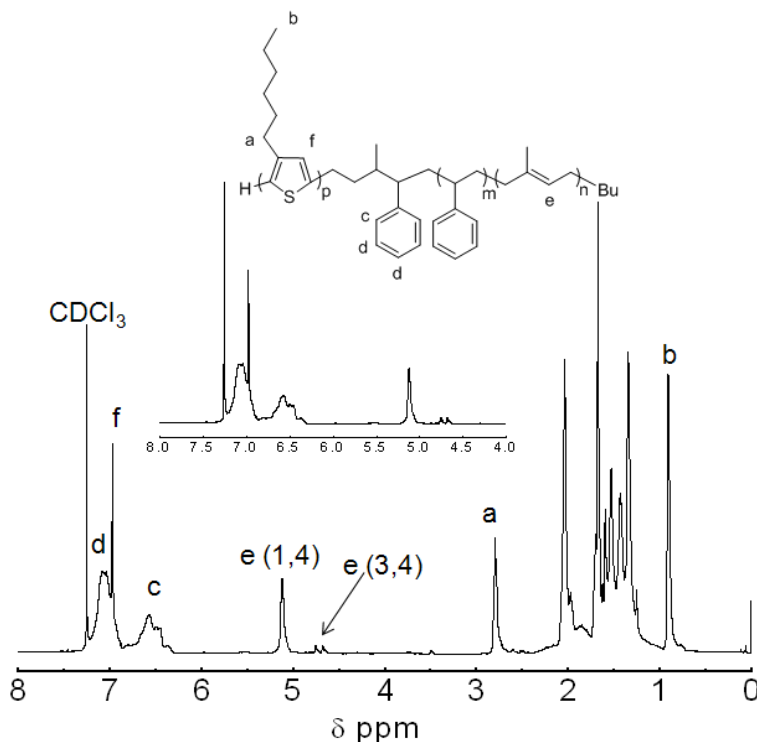


Figure 7-1. ^1H NMR spectrum of polyisoprene-*b*-polystyrene-*b*-poly(3-hexylthiophene) (PI-PS-P3HT)

Polyisoprene-*b*-polystyrene-*b*-poly(3-hexylthiophene) (PI-PS-P3HT) triblock copolymer was synthesized by reacting the allyl-terminated poly(3-hexylthiophene) ($M_n=4500$ g/mol; $DP_n(\text{NMR})=20$) as a solution in dry THF (5 mL) with the *living* polyisoprene-*b*-polystyryl lithium ($M_n(\text{GPC})=3320$ g/mol) in cyclohexane. The coupling reaction was allowed to proceed for 10 min at 40°C . The coupling reaction was performed in a glove box under nitrogen atmosphere. The copolymer was precipitated in methanol and washed with cold cyclohexane to remove the unreacted polyisoprene-*b*-polystyrene diblock copolymer. The composition of the block copolymer was estimated from ^1H NMR spectrum by integrating protons *a* vs protons *c* and *e* (Figure 7-1). The triblock

copolymer contains 28 mol% regioregular poly(3-hexylthiophene), 38.2 mol% polyisoprene, and 33.2 mol% polystyrene. SEC: $M_n=7170$ g/mol; PDI = 1.50.

Monolayer preparation.

The PI-PS-P3HT triblock copolymer chloroform solutions at the concentration, $c = 2$ mg/mL were prepared. Surface pressure - area (π - A) isotherms and polymer monolayers were obtained with R&K Langmuir Blodgett (LB) system (Riegler & Kirstein, GmbH, 160 cm² Teflon trough). The trough was carefully cleaned with 1:1 H₂O₂:NH₃OH solution overnight and subsequently rinsed with DI water (NanoPure, > 18 M Ω cm) for 5 times. A 5 μ L chloroform solution was gently placed on the water surface to ensure initial gas state. After the solvent evaporated for 30 min, the monolayer film was compressed at a rate of 150 μ m/sec. Si substrate used for depositing LB films was cleaned with a mixture of sulfuric acid and Nonchromix, followed by rinsing with DI water and blown dry with N₂. For LB depositions, the Si substrate was withdrawn at a rate of 35 μ m/sec while keeping the pressure constant.

Characterization.

¹H NMR spectra of the polymers were recorded on a VARIAN-INOVA-500 MHz spectrometer at 30 °C. ¹H NMR data are reported in parts per million as chemical shift relative to tetramethylsilane (TMS) as the internal standard. Spectra were recorded in CDCl₃. Morphologies of LB films were examined by Atomic Force Microscopy (AFM; Dimension 3000) in the tapping mode. The scanning rate was 2 Hz. Each sample was imaged at more than 5 locations to ensure the reproducibility of features observed. The fine structure was determined by TEM measurements (JEOL 1200EX scanning/transmission electron microscope (STEM); operated at 80 kV). The emission

spectra of P3HT homopolymer were taken with a Nikon Eclipse TE2000-E microscope coupled with an optical insights hyperspectral unit and a Cascade 512B camera (Roger Scientific). The PL emission of monolayer was measured by using serials of emission filters to measure the emission intensity (the transmission efficiency of these filters is same). The average height, diameter and surface coverage of LB films were obtained by performing the bearing analysis and particle analysis.

7.3 Results and Discussion

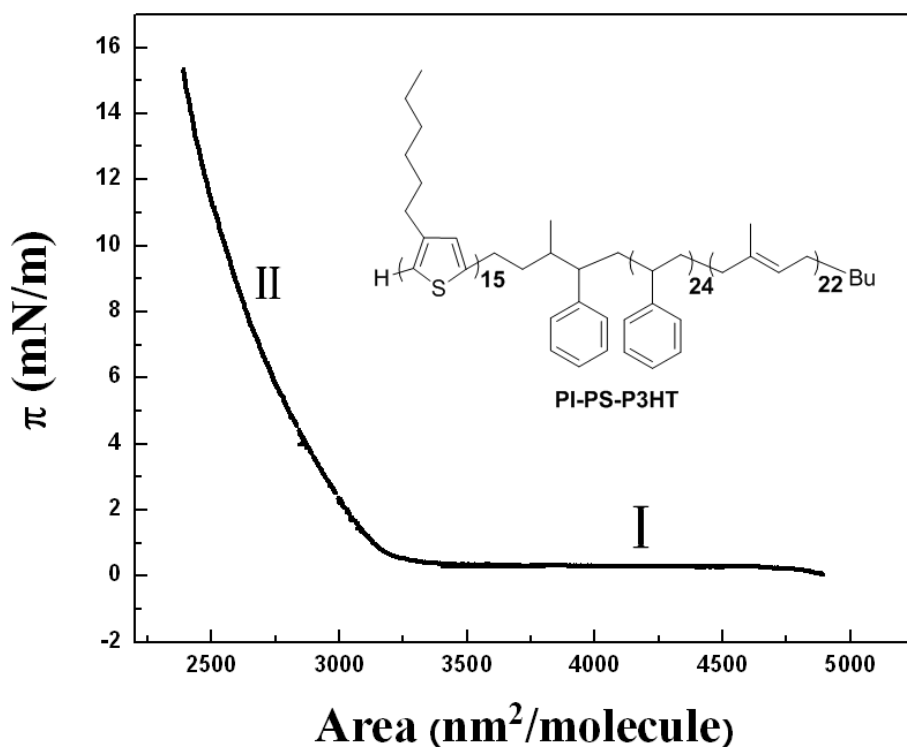


Figure 7-2. Pressure -area isotherms PI-PS-P3HT triblock copolymer : (I) liquid region, (II) condensed region. Insertion shows the chemical structure of PI-PS-P3HT triblock copolymer

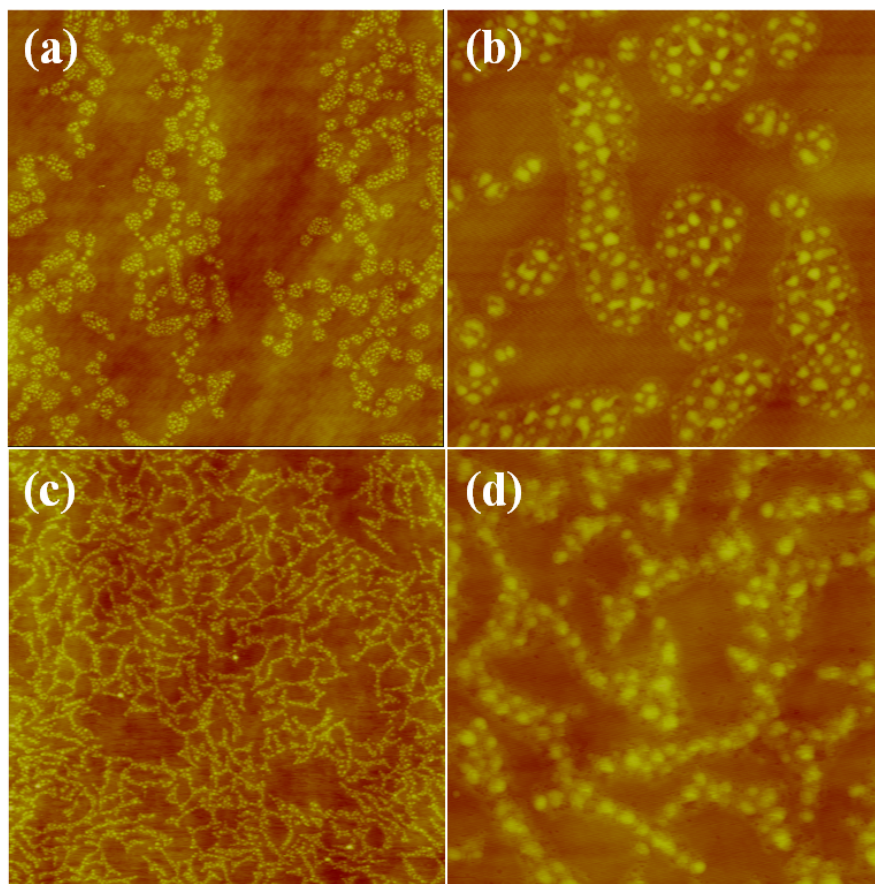


Figure 7-3. AFM height images of the PI-PS-P3HT triblock copolymer LB monolayers obtained from the chloroform solution at (a), (b) gas region; (c),(d) condensed region. Scan size is $20\ \mu\text{m} \times 20\ \mu\text{m}$ for (a) and (c), $5\ \mu\text{m} \times 5\ \mu\text{m}$ for (b) and (d), respectively. The z scale is 50 nm for all images.

The chemical structure of PI-PS-P3HT triblock copolymer is depicted in Figure 7-2. The whole molecule was built and measured by *Materials Studio*, with P3HT block estimated around 6.4 nm, PS block 6.0 nm and the PI block around 9.6 nm in length, respectively.

Langmuir isotherm, i.e., surface pressure- area (π -A) plot, of the PI-PS-P3HT triblock copolymer is shown in Figure 7-2. The continuous pressure rise was indicative of the formation of LB monolayer. Different from the previous hydrophobic block copolymers,⁵ where liquid region are broadly reported, the entire isotherm, is extremely simple, and can be only divided into two typical regions based on the slope of the isotherm (i.e., the pressure increasing rate with the molecular area).^{6,7} They are (i) gas region at $\pi = 0$ mN/m, and (ii) condensed state region at $\pi > 0$ mN/m. The absence of liquid region indicates the monolayer is non-compressible after formation. To best of our knowledge, this is *first* observation of 2 phase isotherm curve in conjugated polymer system. Figure 7-3 shows the representative AFM images of Langmuir monolayers obtained at these two regions, respectively.

The novel worm like domains composed dots structure were observed at the surface pressure $\pi = 0$ mN/m (Figure 7-3a and b). Since the pressure has not yet been applied, the aggregation of polymer was a direct consequence of spontaneous self assembly process. The driving force for the self-assembly was an interplay of the attractive interaction between hydrophilic units and the water phase, and the repulsive interactions between hydrophobic chains and water as chloroform evaporated.^{8,9} Given the hydrophobic nature, the P3HT blocks also have hydrophilic units (i.e. hydrophilic backbone),¹⁰ which have water affinity and enable P3HT fully spread on water surface at lower later pressure. Therefore, the hydrophilic units here originates from P3HT chains, and the hydrophobic chain, without any doubt, can be attributed to the PS and PI blocks since no hydrophilic units exists in those blocks. Close up AFM images shows that the dots is not isolated, but well connected with a spread layer between them (Figure 7-3b).

In order to understand microstructure of the worm like morphology, the monolayer deposited at the gas state was also characterized with TEM.

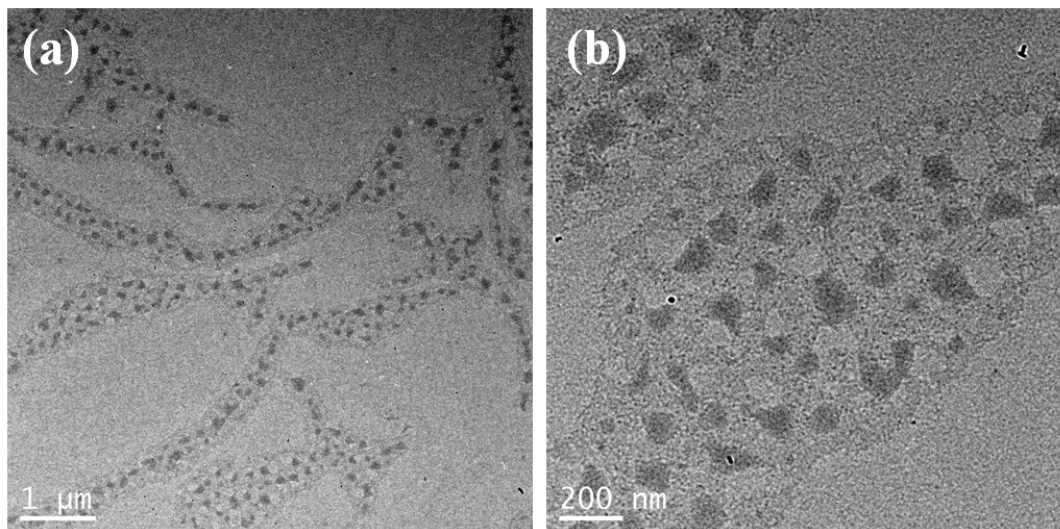


Figure 7-4. TEM images of PI-PS-P3HT triblock copolymer monolayer deposited at gas region at (a) low and (b) high magnification.

Due to its highly localized electron density compared with that of PS and PI blocks,¹¹ P3HT aggregates can be directly observed from TEM without staining, while the PS and PI phase is totally transparent to electron beam generating no contrast in the final images.¹¹ Therefore, the observed morphology from TEM originates from P3HT solely. The TEM images clearly show the existence of P3HT aggregates in dots structure, with size consistent with corresponding AFM images (Figure 7-4a and b). The spread phase between dots structure also shows certain contrast, indicating the existence of P3HT aggregates either (Figure 7-3b). Close up TEM images show that circular domain

is totally amorphous, since no crystallized fiber structure observed as broadly reported.

12,13

	Domain Height (nm)	Domain Diameter (nm)	Surface Coverage (%)
Gas State	4.11	28.87	20.4
Condensed State	5.13	42.34	41.7

Table 7-1. Height, Diameter and surface coverage of PI-PS-P3HT circular domains obtained from AFM images

With the increase of surface pressure from liquid region to condense region, the dots like structure was well preserved, but the size increased from around 28.8 nm to 42.3 nm, and the height also increased from around 4.11 to 5.1nm (Table 7-1). Moreover, the surface coverage of domains dramatically increases from 20.4% to 41.7%, indicating more condensed monolayer at higher surface pressure (Table 1 and Figure 7-3). What is interesting is that these dots no longer form the worm like morphology, but chain into “pearl-necklace” morphology (i.e. isotropic dots domain self-assembly linearly) (Figure 7-3d). The TEM images also shows the condensed the P3HT domains. Such condensed monolayer was also characterized by GISAXS, no diffraction patterns of crystallized P3HT ($0.3\text{-}0.4\text{ \AA}^{-1}$) can be observed,¹⁴ indicating the P3HT exists in the amorphous state, and consistent with TEM result.

Optical property investigation of conjugated pattern

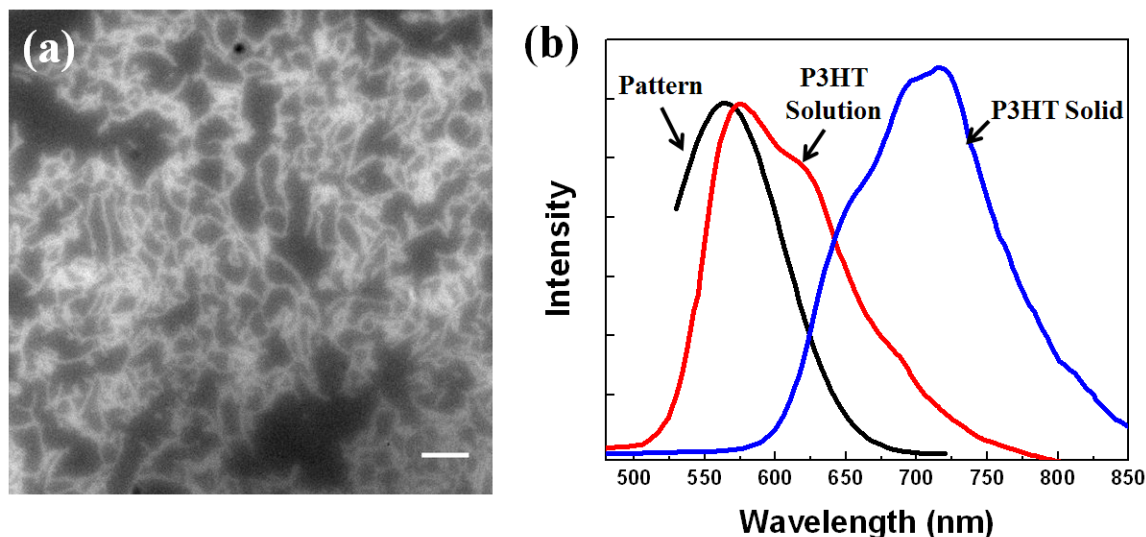


Figure 7-5. (a) fluorescent image of PI-PS-P3HT triblock copolymer monolayer deposited from gas region; (b) Photoluminescence spectra of PI-PS-P3HT patterns, as well as P3HT homopolymer in solution and solid state. The scale bar is 5 μm .

The monolayer deposited at the gas state was also measured with optical microscope coupled with excitation lamp. In stark contrast to previous LB works of CP,^{15,16} where strong inter-chain energy transfer within condensed phases severely quench luminescence, the PL emission from PI-PS-P3HT pattern is so strong that single monolayer can be directly observed under conventional optical microscope via the excitation of wide green lamp (Figure 7-5a). To best of our knowledge, this is *first* report on directly observation of conjugated polymer monolayer through optical microscope.

As discussed previously, the achievement of conjugated polymer film or patterns with high PL efficiency are crucial to fabrication of electroluminescent devices in nano-scale. To reveal the origin of their strong PL emission, the PI-PS-P3HT pattern was

characterized with PL spectra, since optical properties of conjugated polymer are intimately connected to the packing motifs of the molecules as well as its configuration.^{17,18} P3HT homopolymer (both solution and solid state) was also measured as reference. As shown in Figure 7-5b, the vibronic structures of P3HT homopolymer are clearly evident. Electronic structure and optical properties of P3HT has been intensely researched in the past decades.^{1,19,20} In solution state, the conjugated chain is broken into conformational subunits consisting several repeat units long owing to the relatively low energy barrier for small-angle rotations around bonds along the backbone. Therefore the emission is blue-shifted due to the reduced conjugated length.²¹ After drying out (Figure 7-5b), the crystallization of P3HT chain greatly increase the ordering of polymeric chain and degree of interchain interaction, leading to increased conjugated length (i.e. red-shift) and reduced PL efficiency.^{22,23} As reported by Saadeh et.al,²⁴ the PL efficiency dramatically drops from 30-40% to 1-4% during this process due to increased contribution of non-radiative decay via interchain interactions.

In great contrast to crystallized P3HT materials, the monolayer shows the similar emission position as coiled P3HT chains in solution(Figure 7-5b), clearly indicating the successful transferring of this highly PL efficient disordered state into solid film. This result is consistent with result from TEM and GISAXS showing the amorphous state of P3HT chains in LB films. Therefore, the high PL emission can be directly observed from OM. To best of our knowledge, this is first work to direct transfer disordered conjugated polymer chain from solution into solid state, a technique paramount important to fabricate high efficient electroluminescent devices.

Self-assembly process of PI-PS-P3HT triblock copolymer at air/water interface.

As discussed previously, the formation of dots structure is direct consequence of spontaneous self-assembly process, similar to certain amphiphilic polymers.²⁵ The interfacial behavior of amphiphilic copolymer at the air/water interface has been extensively studied since the pioneering work of Eisenberg and Lennox.^{7,24,26,27} To date, the so called “pancake” and “brush” models have been established and proved quite effective in understanding the air/water interfacial behavior of a variety of amphiphilic copolymers, such as linear block copolymers,^{15,28-30} star copolymers,³¹⁻³⁵ comb block copolymers,³⁶ dendritic polymers,^{37,38 39} etc. The “pancake” model refers to the morphology of copolymer LB film formed at low surface pressure. In this model, the hydrophilic blocks spread over the water surface, forming the pancake-like morphology; while the hydrophobic blocks aggregate and sit on the hydrophilic “pancake” to reduce the surface energy. Under the higher compression pressure, the “pancake” is transformed into the “brush”, i.e., the spread hydrophilic blocks are expelled into the water subphase, yielding the brush-like morphology (“brush” model).

Even though the LB techniques is initially designed for amphiphilic molecules, the recent development of this technique, however, has progressively extended its usefulness to different non-amphiphilic system, including the hydrophobic polymer which goes through very complex self-assembly process hardly addressed by the classic theory of Langmuir monolayer for amphiphilic copolymers.⁵ By far, no universal model has been proposed to explain interfacial behavior of hydrophobic copolymer at the air/water interface. However, the presence of hydrophilic components (e.g. hydrophilic units on the hydrophobic polymer) is essential for the formation of Langmuir monolayer because they

facilitate the tethering of whole copolymer chain on the water surface. As for the PI-PS-P3HT monolayer, without any doubt, such hydrophilic component originates from P3HT solely, since both PS and PI are pure hydrophobic materials. In order to form the stable LB monolayer, the P3HT block must spread on the water surface, tethering the whole molecule on the water surface (Figure 7-5a in red). On the hand, the PS and PI from the aggregation to reduce the overall free energy due to unfavorable interaction between them and water (Figure 7-5b, in black).⁴⁰ According to this model, the P3HT block can still forms a continuous layer, generating the contrast in the TEM images. Due to aggregation of highly hydrophobic PS and PI chains, the P3HT, although hydrophobic, was forced to spread on the water surface in order to stabilize the monolayer. Under this scenario, the P3HT block was prohibited from stacking to form crystallized state, in stark contrast to previous work where P3HT chain crystallized in LB film and hydrophilic component (e.g. hydrophilic side chains) were strongly demanded to stabilize the monolayer.⁴¹ Therefore, the adding of hydrophobic blocks was proven to be an effective and robust method to fabricate stable P3HT monolayer in amorphous state.

The worm like pattern formed at zero surface pressure (Figure 7-3a and b, Figure 7-4) resembled those formed by the dewetting process, which has been broadly observed in the LB fabrication.⁴² When the PI-PS-P3HT triblock copolymer solution was placed on the water surface, it formed a thin continuous liquid film (300 nm thick, which was calculated by dividing the solution volume (5 μ L) by the surface area of LB trough (160 cm^2)), stabilized by the positive spreading coefficient of chloroform on the water.⁴² As the solvent evaporated, the liquid film became thinner (< 100 nm), and the increased contribution from the unfavorable interfacial interactions between PS, or PI chains and

water eventually resulted in the dewetting of thin film. The dewetting of thin film can be proceeded via three stages.⁴³ First, the film ruptures, thereby generating randomly distributed holes. Second, the holes then grow and the rims ahead of the holes eventually merge to form a cellular structure. Third, the resulting ribbons in the cellular pattern are unstable and decay into droplets. It is clear that the observed ribbon pattern resembled the morphology formed in the third stage of dewetting process.⁴² As the holes grew during the solvent evaporation, the concentration of PI-PS-P3HT triblock was greatly increased, leading to the aggregation of polymers and thus the formation of dots like structure. Moreover, certain amount of polymer was still left non-aggregated due to the fast dewetting process,²⁵ forming the “spreading phase” between the dots like domain.

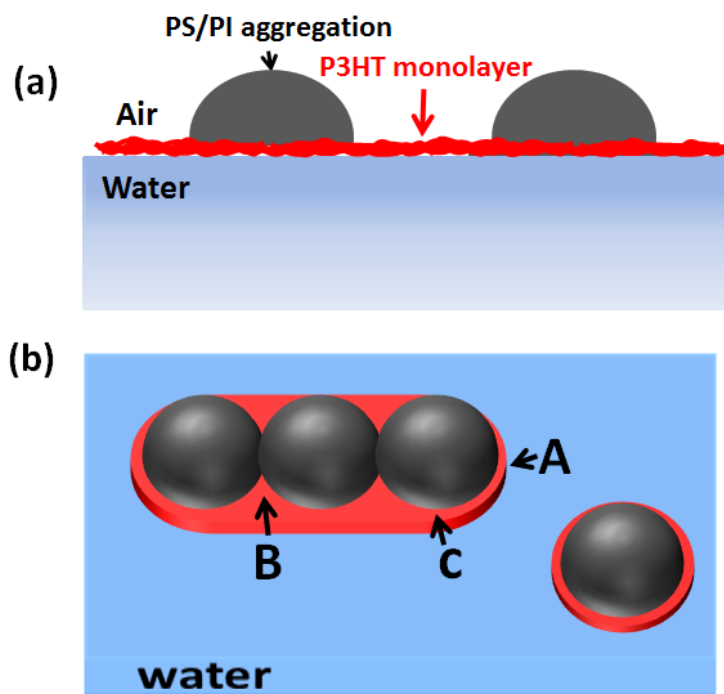


Figure 7-6. Schematic illustration of (a) microstructures of PI-PS-P3HT monolayer. The P3HT phase is shown in red, and PI/PS aggregation in black; and (b) chaining process of dot domain into “pearl-necklace” morphology.

With the increase in surface pressure from liquid region to condense region, the spread polymer was pushed to join the existing dots aggregation under the lateral compression. Therefore, the size of the dots structure increase, and monolayer are more condensed (Figure 7-3 and Table 7-1). In addition, the dots domain becomes more compressed under this lateral force, resulting in little increase of domain height (Table 7-1). Since the polymer already exist in highly aggregated state after dewetting process, the monolayer is less compressible, resulting in the absence of liquid region in the isotherm (Figure 7-2). Most interestingly, due to gradual amalgamation of “spreading phase” with dots domain under surface pressure, the dots domain become connected with each other, chaining into “pearl-necklace” morphology. The anisotropic assembly of individuals with isotropic interaction (chaining process) has been observed frequently in nature, like molecules,^{44,45} surface micelles,⁹ colloidal particles,⁴⁶ etc. It is generally attributed to the competition between short-range attractive forces and long-range repulsion between them.⁴⁶ For example, Duran et.al recently reported the chaining of Polystyrene-block-Poly(ethylene oxide) Stars at the Air/Water Interface. The chaining in the block copolymer brushes was suggested resulting from the attraction of PS aggregation and repulsion between the spread PEO blocks.⁴⁴ Similarly, the chaining of PS-PI-P3HT domain should also originate from the balance between short-range attractive and long-range repulsive forces. Here, the attractive force originates from hydrophobic PI and PS aggregates when they are pushed close enough (Figure 7-6 in black). On the other hand, the spread P3HT chains generates this long range repulsive force due to its affinity with water.⁴⁰ In detail, upon compression, the cores (PS-PI aggregation) were brought closer together and the P3HT on the periphery of PS-PI cores were thus forced to shift to the

side, forming a higher local density (position B or C, Figure 7-6b). Eventually, the PS-PI cores moved closely enough to chain with one another, and the P3HT chains were pushed to either side of elongated PS-PI aggregation.⁹ Thus further chaining was more likely to occur in the area of low PEO density, and the most probable location for additional aggregation was the position A as illustrated in Figure 7-6b.⁹

7.4 Conclusions

In summary, we synthesized a novel PI-PS-P3HT triblock copolymer, and systematically studied its air/water interfacial behavior. Such polymers are found readily patterned due to dewetting process. The adding of hydrophobic blocks, instead of hydrophilic components as exclusively utilized before, can be an effective and robust method to fabricate stable P3HT monolayer in amorphous state, preserving the high PL efficiency as in disordered solution state. The influence of surface pressure on assembly behavior of triblock copolymer at the air/water interface was also explored with both AFM and TEM. It is found that the P3HT block forms a continuous monolayer on the water surface, with PI and PS blocks forming aggregates atop it. The lateral surface pressure results in the chaining process of the aggregates, which originates from the balance between short-range attractive (PS/PI aggregates) and long-range repulsive forces (P3HT monolayer). As such, it stands out as a promising technique to fabricate micro optoelectronic devices but also provides a platform to investigate the complex self-assembly process and charge transfer of conjugated polymer system confined in 2 dimensions.

References:

- (1) Perepichka, I. F.; Perepichka, D. F.; Meng, H.; Wudl, F. *Adv. Mater.* **2005**, *17*, 2281.
- (2) Iovu, M. C.; Jeffries-El, M.; Zhang, R.; Kowalewski, T.; Mccullough, R. *D. J. Macromol. Sci. Part A Pure Appl. Chem.* **2006**, *43*, 1991.
- (3) Iovu, M. C.; Buzdugan, E.; Teodorescu, M.; Britchi, A. G.; Hubca, G.; Iovu, H. *Angew. Makromol. Chem.* **1999**, *271*, 18.
- (4) Schue, F.; Worsfold, D. J.; Bywater, S. *Macromolecules* **1970**, *3*, 509.
- (5) Zhao, L.; Byun, M.; Rzaev, J.; Lin, Z. Q. *Macromolecules* **2009**, *42*, 9027.
- (6) Petty, M. C. *Cambridge ; New York : Cambridge University Press* **1996**.
- (7) Zhu, J.; Eisenberg, A.; Lennox, R. B. *Macromolecules* **1992**, *25*, 6547.
- (8) Cox, J. K.; Yu, K.; Constantine, B.; Eisenberg, A.; Lennox, R. B. *Langmuir* **1999**, *15*, 7714.
- (9) Logan, J. L.; Masse, P.; Dorvel, B.; Skolnik, A. M.; Sheiko, S. S.; Francis, R.; Taton, D.; Gnanou, Y.; Duran, R. S. *Langmuir* **2005**, *21*, 3424.
- (10) Kiriya, N.; Jahne, E.; Adler, H. J.; Schneider, M.; Kiriya, A.; Gorodyska, G.; Minko, S.; Jehnichen, D.; Simon, P.; Fokin, A. A.; Stamm, M. *Nano Lett.* **2003**, *3*, 707.
- (11) Wang, H. B.; You, W.; Jiang, P.; Yu, L. P.; Wang, H. H. *Chem. Eur. J.* **2004**, *10*, 986.
- (12) de Cuendias, A.; Hiorns, R. C.; Cloutet, E.; Vignau, L.; Cramail, H. *Polym. Int.* **2010**, *59*, 1452.

- (13) Hoeben, F. J. M.; Jonkheijm, P.; Meijer, E. W.; Schenning, A. P. H. J. *Chem. Rev.* **2005**, *105*, 1491.
- (14) Zhang, R.; Li, B.; Iovu, M. C.; Jeffries-EL, M.; Sauve, G.; Cooper, J.; Jia, S. J.; Tristram-Nagle, S.; Smilgies, D. M.; Lambeth, D. N.; McCullough, R. D.; Kowalewski, T. *J. Am. Chem. Soc.* **2006**, *128*, 3480.
- (15) Park, J. Y.; Koenen, N.; Forster, M.; Ponnampati, R.; Scherf, U.; Advincula, R. *Macromolecules* **2008**, *41*, 6169.
- (16) Bolognesi, A.; Bajo, G.; Paloheimo, J.; Ostergard, T.; Stubb, H. *Adv. Mater.* **1997**, *9*, 121.
- (17) Zhao, L.; Pang, X. C.; Adhikary, R.; Petrich, J. W.; Lin, Z. Q. *Angew. Chem. Int. Ed.* **2011**, *50*, 3958.
- (18) Zhao, L.; Pang, X. C.; Adhikary, R.; Petrich, J. W.; Jeffries-El, M.; Lin, Z. Q. *Adv. Mater.* **2011**, *23*, 2844.
- (19) Schwartz, B. J. *Annu. Rev. Phys. Chem.* **2003**, *54*, 141.
- (20) Bredas, J. L.; Cornil, J.; Beljonne, D.; dos Santos, D.; Shuai, Z. G. *Acc. Chem. Res.* **1999**, *32*, 267.
- (21) Collini, E.; Scholes, G. D. *Science* **2009**, *323*, 369.
- (22) Ruseckas, A.; Namdas, E. B.; Ganguly, T.; Theander, M.; Svensson, M.; Andersson, M. R.; Inganas, O.; Sundstrom, V. *J. Phys. Chem. B* **2001**, *105*, 7624.
- (23) Nguyen, T. Q.; Doan, V.; Schwartz, B. J. *J. Chem. Phys.* **1999**, *110*, 4068.
- (24) Saadeh, H.; Goodson, T.; Yu, L. P. *Macromolecules* **1997**, *30*, 4608.
- (25) Zhao, L.; Goodman, M. D.; Bowden, N. B.; Lin, Z. Q. *Soft Matter* **2009**, *5*, 4698.

- (26) Zhu, J.; Lennox, R. B.; Eisenberg, A. *Langmuir* **1991**, 7, 1579.
- (27) Zhu, J. Y.; Eisenberg, A.; Lennox, R. B. *J. Am. Chem. Soc.* **1991**, 113, 5583.
- (28) daSilva, A. M. G.; Filipe, E. J. M.; dOliveira, J. M. R.; Martinho, J. M. G. *Langmuir* **1996**, 12, 6547.
- (29) Cheyne, R. B.; Moffitt, M. G. *Langmuir* **2006**, 22, 8387.
- (30) Cox, J. K.; Yu, K.; Eisenberg, A.; Lennox, R. B. *Phys. Chem. Chem. Phys.* **1999**, 1, 4417.
- (31) Francis, R.; Skolnik, A. M.; Carino, S. R.; Logan, J. L.; Underhill, R. S.; Angot, S.; Taton, D.; Gnanou, Y.; Duran, R. S. *Macromolecules* **2002**, 35, 6483.
- (32) Peleshanko, S.; Gunawidjaja, R.; Jeong, J.; Shevehenko, V. V.; Tsukruk, V. V. *Langmuir* **2004**, 20, 9423.
- (33) Peleshanko, S.; Jeong, J.; Gunawidjaja, R.; Tsukruk, V. V. *Macromolecules* **2004**, 37, 6511.
- (34) Genson, K. L.; Hoffman, J.; Teng, J.; Zubarev, E. R.; Vaknin, D.; Tsukruk, V. V. *Langmuir* **2004**, 20, 9044.
- (35) Gunawidjaja, R.; Peleshanko, S.; Tsukruk, V. V. *Macromolecules* **2005**, 38, 8765.
- (36) Zhao, L.; Goodman, M. D.; Bowden, N. B.; Lin, Z. Q. *Soft Matter* **2009**, 5, in press.
- (37) Peleshanko, S.; Sidorenko, A.; Larson, K.; Villavicencio, O.; Ornatska, M.; McGrath, D. V.; Tsukruk, V. V. *Thin Solid Films* **2002**, 406, 233.
- (38) Njikang, G. N.; Cao, L.; Gauthier, M. *Langmuir* **2008**, 24, 12919.

- (39) Njikang, G. N.; Cao, L.; Gauthier, M. *Macromol. Chem. Phys.* **2008**, *209*, 907.
- (40) Zhao, L.; Goodman, M. D.; Bowden, N. B.; Lin, Z. Q. *Soft Mater.* **2009**, *5*, 4698.
- (41) Reitzel, N.; Greve, D. R.; Kjaer, K.; Hows, P. B.; Jayaraman, M.; Savoy, S.; McCullough, R. D.; McDevitt, J. T.; Bjornholm, T. *J. Am. Chem. Soc.* **2000**, *122*, 5788.
- (42) Muller-Buschbaum, P. *J. Phys. Condens. Matter* **2003**, *15*, R1549.
- (43) Reiter, G. *Physical Review Letters* **1992**, *68*, 75.
- (44) Borner, H. G.; Beers, K.; Matyjaszewski, K.; Sheiko, S. S.; Moller, M. *Macromolecules* **2001**, *34*, 4375.
- (45) Dobrynin, A. V.; Rubinstein, M. *Macromolecules* **2000**, *33*, 8097.
- (46) Malescio, G.; Pellicane, G. *Nat. Mater.* **2003**, *2*, 97.

Chapter 8. Self-Assembly of P3HT-PDMAEMA Responsive Block Copolymer at Air/Water Interface

8.1 Introduction:

The response of polyelectrolyte (PEL) to changes in pH or ionic strength is well known.¹⁻⁹ PH responsive polymers contain ionizable pendant groups that can accept or donate protons in response to an environmental change in pH.¹⁰⁻¹² A rapid change in the net charge of pendant groups lead to a dramatic change of the hydrodynamic volume of the polymer chains which ensues from changes in the osmotic pressure exerted by mobile counter ions neutralizing the polymer charges. When integrated PH sensitive polymer in the block copolymer, the amphiphilic balance can be readily adjusted by controlling environment. In the work, the PDMAEMA(poly(dimethylaminoethyl methacrylate))¹³⁻¹⁶ was block with the P3HT, since it is shift and can be used in the bio-field. to forms the diblock polymer, so the self-assembly process, determined by the amphiphic balance of the two blocks, was modified by the environment.

8.2 Experiment Section:

2.2 Monolayer preparation.

The P3HT-PDMAEMA chloroform solutions at the concentration, $c = 12 \text{ mg/mL}$ were prepared. Surface pressure - area ($\pi - A$) isotherms and polymer monolayers were obtained with R&K Langmuir Blodgett (LB) system (Riegler & Kirstein, GmbH, 160 cm² Teflon trough). The trough was carefully cleaned with 1:1 H₂O₂:NH₃OH solution overnight and subsequently rinsed with DI water (NanoPure, > 18 M Ω cm) for 5 times. A 40 μL chlorform solution was gently placed on the water surface to ensure initial gas state.

After the solvent evaporated for 30 min, the monolayer film was compressed at a rate of 150 $\mu\text{m}/\text{sec}$. Si substrate used for depositing LB films was cleaned with a mixture of sulfuric acid and Nonchromix, followed by rinsing with DI water and blown dry with N_2 . For LB depositions, the Si substrate was withdrawn at a rate of 35 $\mu\text{m}/\text{sec}$ while keeping the pressure constant.

2.3 Characterization

Morphologies of LB films were examined by Atomic Force Microscopy (AFM; Dimension 3000) in the tapping mode. The scanning rate was 2 Hz. Each sample was imaged at more than 5 locations to ensure the reproducibility of features observed. The fine structure was determined by TEM measurements (JEOL 1200EX scanning/transmission electron microscope (STEM); operated at 80 kV).

8.3 Result and discussion:

The chemical structure of P3HT-PDMAEMA diblock copolymer is depicted in Figure 8-1. The whole molecule was built and measured by *Materials Studio*, with P3HT block estimated around 11 nm and the PDMAEMA block around 30 nm in length, respectively. The hydrophilic PDMAEMA block is a weak polyelectrolyte brush, whose degree of ionization (d.i.) can be switched at around physiological conditions, therefore more promising materials than conventional strong polyelectrolytes in the bio application.

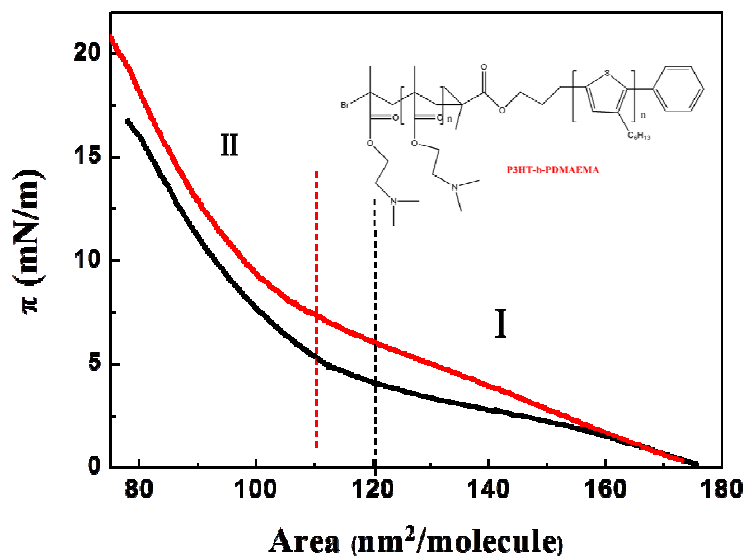


Figure 8-1. Pressure -area isotherms P3HT-PDMAEMA diblock copolymer obtained from DI water (red) and NaOH solution (black): (I) liquid region, (II) condensed region.

Langmuir isotherm, i.e., surface pressure- area (π -A) plot, of the P3HT-PDMAEMA diblock polymer is shown in Figure 8-1. The continuous pressure rise was indicative of the formation of LB monolayer. Similar to the previous hydrophobic diblock copolymers,¹⁷ the entire isotherm, besides the gas region, can be divided into two typical regions based on the slope of the isotherm (i.e., the pressure increasing rate with the molecular area).^{18,19} They are (i) liquid state region at $\pi = 0\sim 8$ mN/m, and (ii) condensed state region at $\pi > 8$ mN/m. Figure 8-2 shows the representative AFM images of Langmuir monolayers obtained at these two regions, respectively; dot-like domains with certain size distribution were observed. Table 1 summarizes the domain height, size, and their surface coverage. With the increase in surface pressure from liquid region to condense region, the domain shape did not show obvious change, however the surface coverage of domains dramatically decrease from 31.5 % at liquid region to 13.8%,

completely different from previous diblock polymer where high surface pressure condense the monolayer leading to increased density of surface micelles. Moreover, the size of the domain also decrease from around 40.7 nm to 28.7 nm, and height decrease from 4.1 nm to -1.4 nm. To best of our knowledge, this is the first report of negative domain height of surface micelle work. The concave structure can be readily observed from the cross-section view of close up images. Besides, the monolayer deposited at the transition region at $\pi = 8$ mN/m was also characterized with AFM images, the coexistence of both two phases can be clearly observed, indicating the phase transition process.

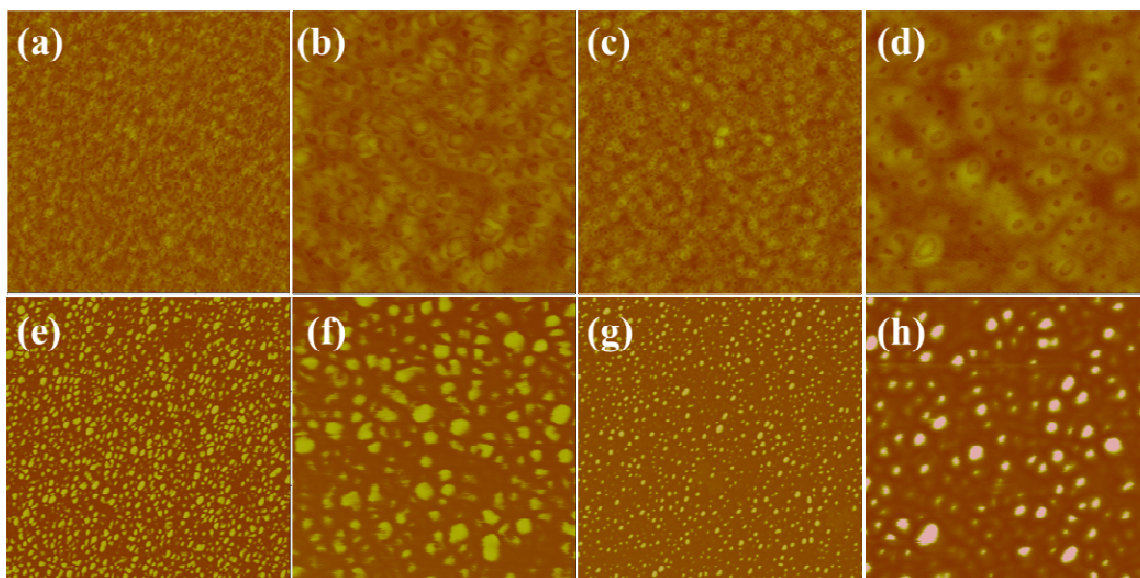


Figure 8-2. AFM height images of the P3HT-PDMAEMA diblock copolymer LB monolayers obtained from the chloroform solution at gas region(a,b height image, and e,f. corresponding phase images); condensed region (c,d height image, and g,h. corresponding phase images). Scan size is $3 \mu\text{m} \times 3 \mu\text{m}$ for a,c,e,g, and, $1 \mu\text{m} \times 1 \mu\text{m}$ for b,d,f,h, respectively. The z scale is 50 nm for all images

Since both PDMAEMA and P3HT are amphiphilic polymers at this condition, in order to indentify the two phase in the AFM images, the monlayer deposited at the liquid

region was characterized with TEM (Figure 8-3). Due to its highly localized electron density compared with that of PDMAEMA,²⁰ P3HT aggregates can be directly observed from TEM without staining, while the PDMAEMA phase is totally transparent to electron beam giving no contrast in the final images. Therefore, all the morphology from TEM originates from P3HT only. The TEM images clearly show the circular domain is composed of P3HT blocks, with size consistent with corresponding AFM images. Close up TEM images show that circular domain is totally amorphous, since no crystallized fiber structure observed as broadly reported. The monolayer deposited at condensed region was also characterized with TEM, and no clear difference can be observed from that in liquid region. It indicates that, along with surface pressure increase, P3HT surface aggregation keeps the same and morphology evolution observed from AFM originates from PDMAEMA blocks.

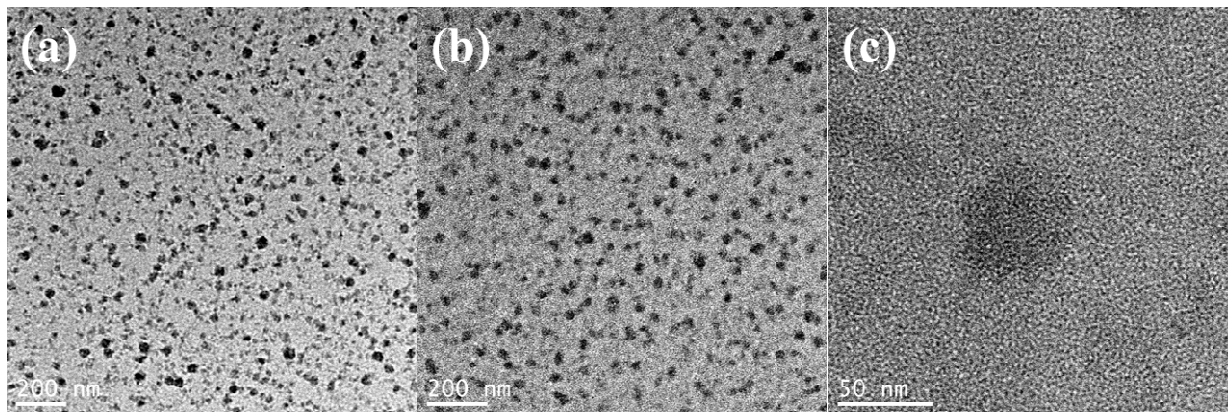


Figure 8-3. TEM image of P3HT-PDMAEMA diblock copolymer monolayer deposited at gas state (a) and condensed state (b), as well as HTEM image of individual domain.

As it is well known that PDMAEMA is a pH responsive polymer. The change in the net charge of its tertiary amine pendant groups lead to a dramatic change of the hydrodynamic volume of the polymer chains which ensues from changes in the osmotic

pressure exerted by mobile counter ions neutralizing the polymer charges.²¹ Therefore, The conformational change of the PDMAEMA block is dominated by the charging (protonation) and decharging (deprotonation) of its tertiary amine side groups. Spread on the water surface, the uncharged PDMAEMA block adsorbs to the air/water interface and becomes intermixed with the PS block. The charged PDMAEMA block, on the contrary, tends to desorb from the air/water interface, triggering the phase transition process.²² The expected degrees of ionization (d.i.) for PDMAEMA at the surface for pH=5.5 (D.I. water) conditions are reported to be 0.85,²³ indicating 85% of the block are charged. Therefore, the PDMAEMA blocks tends to absorbed on the water surface, or partially dissolved in the water subphase (Figuree 4a). The yellow chain indicates those charged, and backs ones for those uncharged. On the other hand, the unfavorable interfacial interaction between the hydrophobic P3HT block and water leads to the aggregation of P3HT, forming circular domain to reduce the overall free energy of the system (Figure 8-4a).

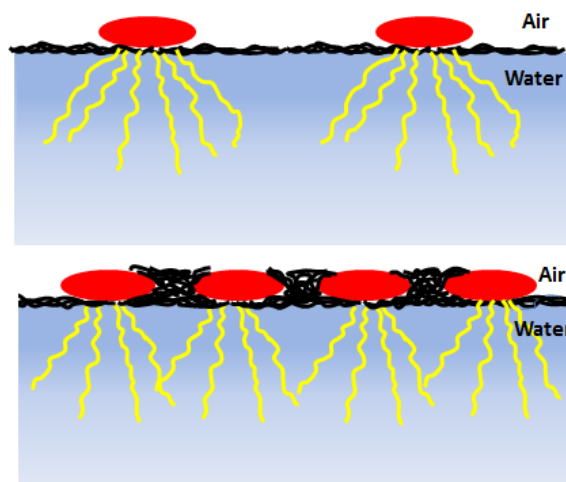


Figure 8-4. Schematic illustration of self-assembly process, P3HT aggregation is shown in red, hydrophilic PDMAEMA is shown in yellow, and hydrophobic PDMAEMA is shown in black

Due to hydrophobic nature of uncharged PDMAEMA chain spreading on water surface, the surface pressure lead to the collapse of this layer by folding and aggregating it on top of the water surface,²⁴ instead of dissolving into water subphase as conventional hydrophilic blocks, e.g. PEO, PAA or charged PDMAEMA. The decrease of circular height can be attributed to this process. As shown in Figure 8-3b, due to the folding of uncharged PDMAEMA chains (black) as a result of applied compressive surface pressure, the surface stress was released and the space between P3HT domains was filled with uncharged PDMAEMA chains, thereby leading to the reduction in the height difference between the PS domain and the spreading PLA phase. A concave P3HT domain was finally formed at extremely high pressure when the folded PDMAEMA chains layer is thicker than the P3HT domains (Figure 8-5). Since the PDMAEMA chain has no contrast in the TEM images, there is seldom any change observed.

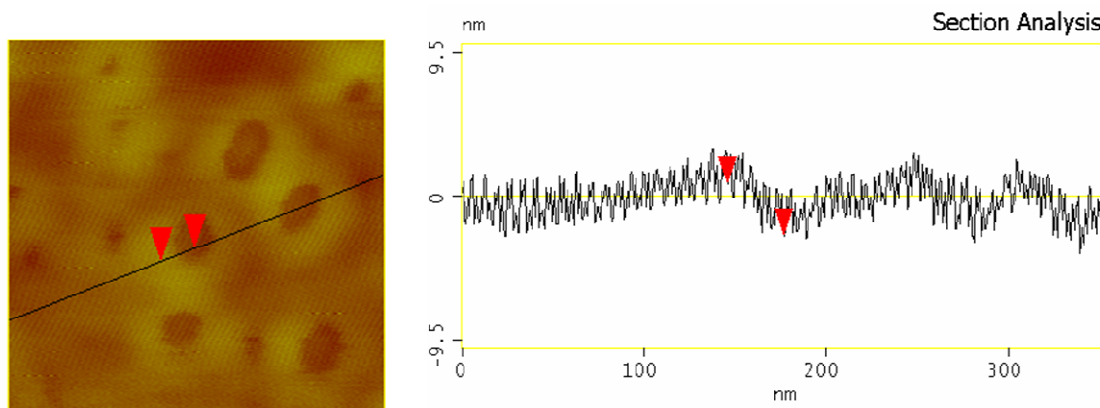


Figure 8-5. Cross-section analysis of LB film at high pressure.

Optical properties

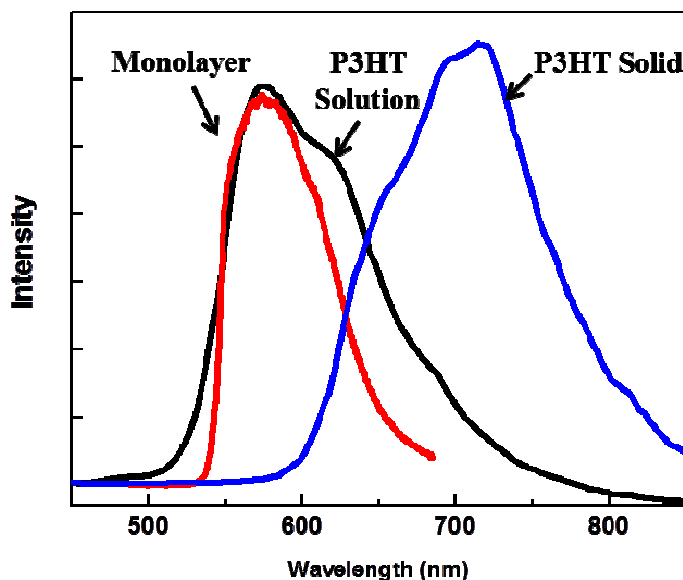


Figure 8-6. Photoluminescence spectra of P3HT-PDMAEMA patterns, as well as P3HT homopolymer in solution and solid state.

The achievement of high PL efficiency conjugated polymer film is crucial to fabrication of nano-size electroluminescent devices. The spectra was measure on LB monolayer, with P3HT homopolymer (same to each P3HT blocks) in both solution and solid state as reference. The vibronic structures of homopolymer P3HT are clearly evident (i.e., 0-0 emission peak at 574 nm and 0-1 emission peak at 620 nm for solution state; and 0-0 emission peak at 655 nm and 0-1 emission peak at 715 nm for solid state). Electronic structure and optical properties of P3HT has been intensely researched in the past decades,²⁵⁻²⁷ and two basic types of emission have been identified: intramolecular emission and interchain emission. The 0-0 emission is broadly attributed to the intramolecular exciton, and 0-1 emission is strongly related to interchain interaction.^{28,29}

In solution state, the conjugated chain is broken into conformational subunits consisting several repeat units long owing to the relatively low energy barrier for small-angle rotations around bonds along the backbone. Therefore the emission is blue-shift due to the reduced conjugated length.³⁰ After drying out (Figure 8-6), the aggregation of P3HT chain, e.g. crystallization, greatly increase the ordering of polymeric chain and degree of interchain interaction, leading to increased conjugated length (e.g. red-shift) and enhanced 0-1 peak intensity relative to the 0-0 peak, respectively. As reported by Saadeh et.al,³¹ the PL efficiency dramatically drops from 30-40% to 1-4% during this process due to increased contribution of non-radiative decay via interchain interactions. In order to preserve high luminescence efficiency observed in solution state, the conjugated polymer are usually incorporated into an inert solid matrix, which often suffers from phase separation or low CP concentration.²⁶

In contrast to P3HT solid materials, the LB monolayer of P3HT-PDMAEMA shows the similar 0-0 emission position as coiled P3HT chains in solution, clearly indicating the successful transferring of this highly efficient disordered state into solids. This is consistent with the TEM images where amorphous P3HT domain is observed. Moreover, the 0-1 emission (interchain) peak relative to 0-0 emission is also dramatically reduced, even negligible, a clear evidence of prohibited interchain energy transfer in P3HT domain. Therefore, the PL efficiency was further enhanced. To best of knowledge, this is the first work to directly transfer disordered conjugated diblock polymer chain from solution into solid state, a technique paramount important to fabricate high efficient electroluminescent devices.

Clearly, this phenomenon can be attributed to the existence of PDMAEMA blocks since

P3HT monolayer exist in the form of crystallized state. In the organic solvent, good for side groups and poor for backbones, the P3HT molecules fold back on themselves into helical like conformation with syn configuration of thiophene units in which all sulfur atoms are directed inside the cavity and hydrocarbon groups are oriented outside the helix.³²⁻³⁴ By the slow draying, such helix-like e simple P3HT can even be presrved into solid state.³⁴ After spread on the water surface, the unpleasuent interaction between water and hydrophobic alkyl side drive the crystallization of RR-P3HT to reduce the overall free energy. For the P3HT-PDMAEMA monolayer, the existance of continous hydrophic PDMAEMA layer effectively blocks the direct contact between the P3HT phase siting on tis top and water surface, reducing the drive force for P3HT to crystallize. Therefore, the disordered helix-like molecular configuration may well preserved into the solid state, and alkey side chain oriented outside the helix effectively block the inter chain energy transfer between neighboring conjugated backbones, which is consistent with the PL result.

Influence of PH stimuli

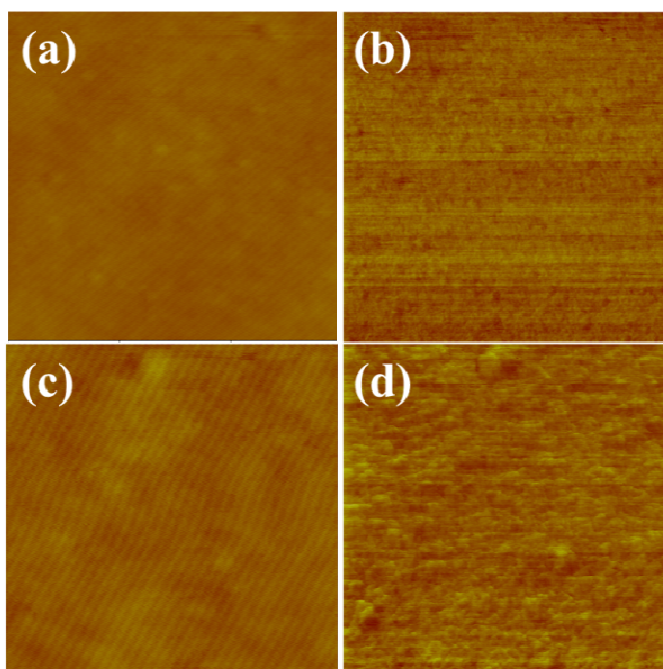


Figure 8-7. AFM height images of the P3HT-PDMAEMA diblock copolymer LB monolayers obtained under basic water subphase (a,c height image, and b,d. corresponding phase images); Scan size is $3\ \mu\text{m} \times 3\ \mu\text{m}$ for a,b, and $1\ \mu\text{m} \times 1\ \mu\text{m}$ for c,d, respectively. The z scale is 50 nm for all images

As discussed in the first section, PDMAEMA is a Ph responsive polymer with degrees of ionization (d.i.) can be readily modified by the PH value of water subphase. The diblock copolymer was spreaded on the basic water subphase (PH=10), under which the ODMAEMA is almost completely uncharged. Figure 8-1 indicates Langmuir isotherms recorded at different pH subphase conditions at 20 °C. As shown in the figure, the overall shapes of the two curves at pH 10 (blue line) and pH 5.5 (red line) are similar. The monolayer deposited under these condition shows featureless morphology in the AFM images (Figure 8-8), indicating no phase segregation process occurs to form the surface micelle. Besides, the TEM images also shows the absence of any P3HT aggregation,

indicating the P3HT chain should be higher isolated. These results clearly shows that uncharged PDMAEMA block should also adsorbs to the air/water interface and becomes intermixed with the P3HT chains. Due to existence of hydrophilic units on both two block, they can both attach to water surface, resulting in monolayer.

8.4 Conclusion

In summary, we synthesized a novel PI-PDMAEMA diblock copolymer, and systematically studied its air/water interfacial behavior. The morphology evolution under environment was systematically investigated, which shows sensitive PH response. The adding of responsive blocks was also proven to be an effective and robust method to fabricate stable P3HT monolayer in amorphous state, preserving the high PL efficiency as in disordered solution state. The influence of surface pressure on assembly behavior of triblock copolymer at the air/water interface was also explored with both AFM and TEM. The surface micelle was found to show novel self-assembly process under surface pressure, assuming the concave structure. The self-assembly process was systematically examined, and a model was proposed to explain the complex dynamics process.

References:

- (1) Mora-Huertas, C. E.; Fessi, H.; Elaissari, A. *International Journal of Pharmaceutics*, **385**, 113.
- (2) Chen, T.; Ferris, R.; Zhang, J. M.; Ducker, R.; Zauscher, S. *Progress in Polymer Science*, **35**, 94.
- (3) Bunsow, J.; Kelby, T. S.; Huck, W. T. S. *Accounts of Chemical Research*, **43**, 466.
- (4) Shakya, A. K.; Sami, H.; Srivastava, A.; Kumar, A. *Progress in Polymer Science*, **35**, 459.
- (5) Tan, B. H.; Tam, K. C. *Advances in Colloid and Interface Science* 2008, **136**, 25.
- (6) Ballauff, M.; Lu, Y. *Polymer* 2007, **48**, 1815.
- (7) Hartig, S. M.; Greene, R. R.; Dikov, M. M.; Prokop, A.; Davidson, J. M. *Pharmaceutical Research* 2007, **24**, 2353.
- (8) Nylander, T.; Samoshina, Y.; Lindman, B. *Advances in Colloid and Interface Science* 2006, **123**, 105.
- (9) Forster, S.; Abetz, V.; Muller, A. H. E. *Polyelectrolytes with Defined Molecular Architecture Ii* 2004, **166**, 173.
- (10) Tong, W. J.; Gao, C. Y. *Chemical Journal of Chinese Universities-Chinese* 2008, **29**, 1285.
- (11) Thomas, D. B.; Vasilieva, Y. A.; Armentrout, R. S.; McCormick, C. L. *Macromolecules* 2003, **36**, 9710.
- (12) Qiu, Y.; Park, K. *Advanced Drug Delivery Reviews* 2001, **53**, 321.

- (13) Zhang, W. L.; He, J. L.; Liu, Z.; Ni, P. H.; Zhu, X. L. *Journal of Polymer Science Part a-Polymer Chemistry*, **48**, 1079.
- (14) Tang, X. D.; Liang, X. C.; Gao, L. C.; Fan, X. H.; Zhou, Q. F. *Journal of Polymer Science Part a-Polymer Chemistry*, **48**, 2564.
- (15) Schacher, F.; Rudolph, T.; Wieberger, F.; Ulbricht, M.; Muller, A. H. E. *Acs Applied Materials & Interfaces* 2009, **1**, 1492.
- (16) Zhang, Z. B.; Zhu, X. L.; Xu, F. J.; Neoh, K. G.; Kang, E. T. *Journal of Membrane Science* 2009, **342**, 300.
- (17) Zhao, L.; Byun, M.; Rzayev, J.; Lin, Z. Q. *Macromolecules* 2009, **42**, 9027.
- (18) Petty, M. C. *Cambridge ; New York : Cambridge University Press* 1996.
- (19) Zhu, J.; Eisenberg, A.; Lennox, R. B. *Macromolecules* 1992, **25**, 6547.
- (20) Wang, H. B.; You, W.; Jiang, P.; Yu, L. P.; Wang, H. H. *Chem-Eur J* 2004, **10**, 986.
- (21) Chen, T.; Ferris, R.; Zhang, J. M.; Ducker, R.; Zauscher, S. *Prog Polym Sci* 2010, **35**, 94.
- (22) Plamper, F. A.; Schmalz, A.; Ballauff, M.; Muller, A. H. E. *J Am Chem Soc* 2007, **129**, 14538.
- (23) Rehfeldt, F.; Steitz, R.; Armes, S. P.; Von Klitzing, R.; Gast, A. P.; Tanaka, M. *J Phys Chem B* 2006, **110**, 9171.
- (24) Kubies, D.; Machova, L.; Brynda, E.; Lukas, J.; Rypacek, F. *J Mater Sci-Mater M* 2003, **14**, 143.
- (25) Schwartz, B. J. *Annu Rev Phys Chem* 2003, **54**, 141.

- (26) Perepichka, I. F.; Perepichka, D. F.; Meng, H.; Wudl, F. *Adv Mater* 2005, **17**, 2281.
- (27) Bredas, J. L.; Cornil, J.; Beljonne, D.; dos Santos, D.; Shuai, Z. G. *Accounts Chem Res* 1999, **32**, 267.
- (28) Ruseckas, A.; Namdas, E. B.; Ganguly, T.; Theander, M.; Svensson, M.; Andersson, M. R.; Inganas, O.; Sundstrom, V. *J Phys Chem B* 2001, **105**, 7624.
- (29) Nguyen, T. Q.; Doan, V.; Schwartz, B. J. *J Chem Phys* 1999, **110**, 4068.
- (30) Collini, E.; Scholes, G. D. *Science* 2009, **323**, 369.
- (31) Saadeh, H.; Goodson, T.; Yu, L. P. *Macromolecules* 1997, **30**, 4608.
- (32) Cui, C. X.; Kertesz, M. *Phys Rev B* 1989, **40**, 9661.
- (33) Williams, D. R. M.; Fredrickson, G. H. *Macromolecules* 1992, **25**, 3561.
- (34) Kiriya, N.; Jahne, E.; Adler, H. J.; Schneider, M.; Kiriya, A.; Gorodyska, G.; Minko, S.; Jehnichen, D.; Simon, P.; Fokin, A. A.; Stamm, M. *Nano Lett* 2003, **3**, 707.

Acknowledgements

I sincerely appreciate my major advisor Prof. Zhiqun Lin for his support, instructions and patience; his has been a great mentor to me.

I would like to thank all the committee members, Prof. Kaitlin Bratile, Prof. Surya K. Mallapragada, Prof. Fang Ning, and Prof. Malika Jeffries-EL for committing their time and effort into my work.

I also would like to thank all my group members, Dr. Xinchang Pang, Dr. Myunghwan Byun, Dr. Jun Wang, Matthew Goodman, Wei Han, Xukai Xin, Chaowei Feng, Jaehan Jung, Bo Li, Weijie Yu, and Hsiang-Yu Liu. I feel quite fortunate to work with these smart guys.

Finally, I would like to thank all our collaborators and those who have provided technical support to my work, including Prof. Fang Ning, Prof. Harry T. Horner and Tracy Pepper.

Publications

1. **L. Zhao**, Z. Lin*, "Self-assembly non-linear block copolymer at air/water interface", *Soft Mater*, DOI: 10.1039/C1SM05745F (Featured on **Cover**).
2. **L. Zhao**, X. Pang, R. Adhikary, J. Petrich, and Z. Lin*, "Organic-Inorganic Nanocomposites by Placing Conjugated Polymers in Intimate Contact with Quantum Rods", *Adv. Mater.*, 23, 2844 (2011) (Featured on **Frontispiece**)
3. **L. Zhao**, X. Pang, R. Adhikary, J. Petrich, and Z. Lin*, "Semiconductor anisotropic nanocomposites via directly coupling conjugated polymers with quantum rods", *Angew. Chem. Int. Ed.*, 50, 3958 (2011), (Featured in Inside **Front Cover**, Featured on **Nanowerk** and **MRS bulletin**)
4. **L. Zhao**, J. Wang and Z. Lin*, "Semiconducting nanocrystals, conjugated Polymers, and conjugated polymer/nanocrystal nanohybrids and their use in solar cells", *Front. Chem. Chin.* 5, 33 (2010)
5. **L. Zhao**, M. Byun, J. Rzaev, and Z. Lin*, "Polystyrene–polylactide bottlebrush block copolymer at the air/water interface", *Macromolecules* 42, 9027 (2009)
6. **L. Zhao**, M. Goodman, N. B. Bowden, and **Z. Lin***, "Self-assembly of ultrahigh molecular weight comb block copolymer at the air/water interface", *Soft Matter* 5, 4698 (2009)
7. X. Pang, **L. Zhao**, C. Feng, and Z. Lin*, "Novel Amphiphilic Multi-Arm, Star-Like Coil-Rod Diblock Copolymers via a Combination", *Macromolecules*, accepted (2011)
8. X. Pang, **L. Zhao**, M. Akinc, J. K. Kim, and Z. Lin*, "Novel amphiphilic multi-arm, star-like block copolymers as unimolecular micelles", *Macromolecules* 44, 3746 (2011)
9. M. He, **L. Zhao**, J. Wang, W. Han, Y. L. Yang, F. Qiu, and Z. Lin*, "Self-assembly of all-conjugated poly(3-alkylthiophene) diblock copolymer nanostructures from mixed selective solvents", *ACS Nano* 4, 3241, (2010)
10. M. Goodman, **L. Zhao**, and Z. Lin*, "Self-assembly of CdTe tetrapods into network monolayers at air/water interface", *ACS Nano*, 4, 2043 (2010)
11. J. Wang, **L. Zhao**, V. S.Y. Lin and **Z. Lin***, "Formation of various TiO₂ nanostructures from electrochemically anodized titanium", *J. Mater. Chem.* 19, 3682 (2009)

12. W. Han, M. Byun, **L. Zhao**, J. Rzyev, and Z. Lin*, "Controlled Evaporative Self-Assembly of Hierarchically Structured Bottlebrush Block Copolymer with Nanochannels", *J. Mater. Chem.* DOI: 10.1039/c1jm10978b
13. J. Wang, **L. Zhao**, and M. Goodman, and **Z. Lin***, "Semiconducting nanostructures for new energy generating and novel bio-detecting" in the book entitled, "Encyclopedia of semiconductor nanotechnology", **American Scientific Publishers** (2010)